Improving Strength and Stability in Continuum Robots

A Dissertation Presented for the

Doctor of Philosophy

Degree

The University of Tennessee, Knoxville

Jake A. Childs

December 2022

© by Jake A. Childs, 2022
All Rights Reserved.

To my family and friends.

Acknowledgments

I would like to take the opportunity to acknowledge the people in my life that have helped me in my personal, professional, and academic journeys. Their support and inspiration has contributed to the success of this work.

I would like to begin by expressing my gratitude to my advisor Dr. Caleb Rucker. I've learned so much from him through my time in the REACH Lab, where I've learned to be become a better researcher, educator, and engineer. I'm grateful for the academic freedom and mentorship he provided me throughout my time in graduate school, as it's helped me write a dissertation I'm proud of. I would like to thank my committee members, Dr. Jindong Tan, Dr. Jessica Burgner-Kahrs, and Dr. Brett Compton, whose feedback have enhanced this work. Many anonymous reviewers have also provided valuable feedback for the work presented in this dissertation.

I would like to thank the instructors from Roane State who helped me in my early academic trajectory. Dr. Larry Bouldin, Jill Denton, and Eric Bouldin gave me the first tools in my mathematics toolbox and they sparked a joy of education, mentorship, and mathematics that continues to this day. Mike Hill taught me how to take pride in my writing and gave me the courage to become a writing tutor.

I'm grateful for my labmates and friends in the REACH Lab that truly made my time in graduate school, both in and out of the lab, unforgettable. Kaitlin Oliver-Butler was the first person I collaborated with when I started in the REACH Lab, providing technical (and moral) support in planning research and prototyping. In addition, Kaitlin also ensured the smooth transfer of leadership within the Graduate

Association of MABE Engineers (GAME) and its STEM outreach efforts, allowing the club to successfully continue on after defending her dissertation. Vince Aloi was my personal sounding board on programming and mechanics problems, as well as helping coordinate STEM outreach events for GAME. Michael Buckley ran so many FEA simulations on bellows and slotted-tube designs and built more bellows prototypes than I could count. Khoa Dang was always there to help out building the next robot or experimental setup for everyone in the lab. Riley Tavasolli also ran many FEA simulations on slotted-tube designs and assisted in prototyping.

Outside the REACH Lab, there are a number of people that I would like to thank and acknowledge. I would like to thank Dr. Doug Aaron, who was always on-hand to help me as a lab manager and I've learned many lessons from him on being an effective communicator and leader. Dr. Jeffrey Reinbolt provided invaluable advice in preparing for graduate school and imparted valuable wisdom on work-life balance, research, and education. Kaustubh Mungale helped me with grading while I adapted an in-person lab course to a fully virtual course during a global pandemic. I'd like to thank Brett Brownlee and Zacharia Nelson, who helped break up the days with banter on VR, hoola-hoops, machine learning, and the challenges of getting autonomous vehicles to stop at intersections. In the MABE business office, I would like to thank Tammy Johnson, Janet Carnes, Rhnea Reagon, and Ruthann Moyers. They always had the answers to our finances, from assisting with conference arrangements, to helping get our pizza order reimbursements for GAME and outreach meetings.

In the last year of writing this dissertation, I had the opportunity to move to Nashville, where I've had some incredible experiences and have made some great friends along the way. I'd like to thank the team at Endotheia, Joshua Gafford, Scott Webster, Patrick Anderson, Laura Davis, Tyler Efird, and Chris Schlichter for being such an awesome team to work with and providing feedback on the defense presentation. I'd like to thank Katerina Freeman for her patience and support, especially during the later stages of dissertation experiments and writing. Lastly, I would like to thank my mom, Vickie Hensley, who has provided unconditional love

and support throughout my life and instilled in me the importance of education and lifelong learning. She has always been there when I needed her most and I'm forever grateful for her.

Parts of this work are based upon work supported by the National Science Foundation under IIS-1652588, an NSF CAREER Award. Any opinion, findings, and conclusions or recommendations expressed herein are those of the author and do not necessarily reflect the views of the National Science Foundation.

Abstract

Continuum robots, which are bio-inspired 'trunk-like' robots, are characterized for their inherent compliance and range of motion. One of the key challenges in continuum robotics research is developing robots with sufficient strength and stability without adding additional weight or complexity to the design. The research conducted in this dissertation encompasses design and modeling strategies that address these challenges in strength and stability. This work improves three continuum robot actuation paradigms: (1) tendon-driven continuum robots (TDCR), (2) concentric tube robots (CTR), and (3) concentric push-pull robots (CPPR). The first chapter of contribution covers strategies for improving strength in TDCRs. The payload capacity and torsional stiffness of the robot can be improved by leveraging the geometry of the backbone design and tendon routing, with design choices experimentally validated on a robot prototype. The second chapter covers a new bending actuator, concentric precurved bellows (CPB), that are based upon CTR actuation. The high torsional stiffness of bellows geometry virtually eliminates the torsional compliance instability found in CTRs. Two bellows designs are developed for 3D printing and the mechanical properties of these designs are characterized through experiments on prototypes and in static finite element analysis. A torsionally rigid kinematic model is derived and validated on 3D printed prototypes. The third chapter of contribution covers the development and validation of a mechanics-based CPPR kinematics model. CPPRs are constructed from concentrically nested, asymmetrically patterned tubes that are fixed together at their distal tips. Relative translations

between the tubes induces bending shapes from the robot. The model expands the possible design space of CPPRs by enabling the modeling of external loads, non-planar bending shapes, and CPPRs with more than two tubes. The model is validated on prototypes in loaded and unloaded experiments.

Table of Contents

1 Introduction **1**

1.1 Background and Motivation 1

1.2 Tendon-Driven Continuum Robots 2

1.3 Concentric Tube Robots 5

1.4 Concentric Push Pull Robots 8

1.5 Outline and Contributions 11

2 Improving Strength in Tendon-Driven Continuum Robots **13**

2.1 Disclosure of Previously Published Material 13

2.2 Overview 13

2.2.1 Novel Backbone Design with High Torsional and Shear Stiffness 14

2.3 Tendon Routing for Tip Load Resistance 22

2.4 Robot Embodiment 25

2.4.1 Tendon Pathway Guides 25

2.4.2 Anti-Buckling Tendon Mechanism 27

2.5 Robot Compliance and Payload Capacity 32

3 Concentric Precurved Bellows: Improving Stability in Concentric Tube Robots **35**

3.1 Disclosure of Previously Published Material 35

3.2 Overview 35

3.3 Bellows Design and Fabrication 38

3.3.1 Revolute Bellows Design . . . 41
3.3.2 Helical Bellows Design . . . 41
3.3.3 Pre-curving bellows via Heat Treatment . . . 41
3.3.4 Example Bellows Specifications and Fabrication . . . 42
3.4 Bellows Modeling . . . 42
3.4.1 Bellows Parameter Characterization . . . 42
3.4.2 Kinematic Modeling . . . 48
3.5 Validation Experiments . . . 51
3.5.1 Validation of Torsional Rigidity Assumption . . . 51
3.5.2 Validation of Kinematic Model . . . 52
3.5.3 Payload Demonstration . . . 53

4 Model-Based Design of Concentric Push-Pull Robots for High Strength 60

4.1 Disclosure of Published Material . . . 60
4.2 Overview . . . 60
4.3 Modeling . . . 61
4.3.1 Conventions and Modeling Assumptions . . . 62
4.3.2 Kinematics of Tubes with Offset Stiffness Centers . . . 62
4.3.3 Model Structure Overview . . . 66
4.3.4 Embedding the Constraints of Concentricity . . . 66
4.3.5 Parameterization of Free Variables . . . 71
4.3.6 Principal of Minimal Potential Energy . . . 71
4.3.7 Model Boundary Conditions . . . 73
4.3.8 Summary of Solution Procedure . . . 76
4.4 Tube Pattern Design and Parameter Characterization . . . 80
4.4.1 Tube Pattern Designs . . . 80
4.4.2 Young's modulus calibration . . . 83
4.4.3 Parameter Characterization . . . 86

4.5 Experimental Validation 88
4.5.1 Experimental Setups 91
4.5.2 Case 1: Two-Tube, Constant Stiffness Center Location 91
4.5.3 Case 2: Two Tube, Varying Stiffness Center Location 93
4.5.4 Case 3: Three Tube, Constant Stiffness Center Location . . . 97
4.5.5 Error Sources 97
4.6 Conclusion 105

5 Conclusions **107**
5.1 Tendon-Driven Continuum Robots 107
5.2 Concentric Tube Robots 108
5.3 Concentric Push-Pull Robots 109

Bibliography **111**

Appendix **129**

Vita **129**

List of Tables

2.1 Dimensions of unit cell design used in experiments 16
2.2 Mechanical properties of unit cell from FEA and experimental setups. 18

3.1 Flexural to Torsional Rigidity Ratios 37
3.2 Bellows dimensions of 3D printed prototype used in kinematic and bending experiments 43
3.3 FEA and experimental characterization of revolute and helical bellows prototypes. 47
3.4 Kinematic modeling error of concentric precurved bellows prototype . 54

4.1 Kinematic Nomenclature 63
4.2 Nitinol Tube Dimensions and Calibrated Mechanical Properties . . . 84
4.3 Slot parameters used for Case 1 CPPR 94
4.4 Mechanical Properties of Case 1 Sheaths 94
4.5 Tip Position Error Statistics of Case 1 94
4.6 Constant slot parameters used for Case 2 CPPR 98
4.7 Tip Position Error Statistics of Case 2 102
4.8 Slot parameters used for Case 3 CPPR 102
4.9 Tube Parameters of Case 3 Sheaths 102
4.10 Tip Position Error Statistics of Case 3 104

List of Figures

1.1 General design of a tendon-driven continuum robot (TDCR) consisting of a flexible backbone, tendons, and spacer disks that guide the tendons. 4

1.2 Backbone designs used in TDCRs to improve strength and range of motion, which include origami-inspired designs as shown in [1](a), [2](b), and [3](c), stacked vertebrae backbones [4](d), and active stiffening designs using combinations of pneumatic-tendon actuation [5] (e), and SMA-based heating [6](f). 4

1.3 Concentric Tube Robot (CTR) consisting of two precurved tubes. . . 6

1.4 Examples of tube patterning used to reduce the flexural to torsional rigidity of the tube, using repeated slotted patterns in [7](a) and [8] (b), cellular patterns based on topology optimization results in [9](c), and asymmetric patterning in [10](d). Auxetic patterns also enable control over flexural and torsional rigidity values of the tube [11](e). 6

1.5 Concentric Push-Pull Robot (CPPR) consisting of two asymetrically patterned tubes. 9

1.6 CPPRs can be fabricated at needle-sized scales (left). Ch. 4 details the derivation and validation of the first kinematics model for CPPRs in the literature, which can account for external loads (middle) and robots using more than two tubes. This model will be useful in the design and analysis of CPPRs for MIS applications (image from [12]) (right). 9

2.1 Strength-improved TDCR using a torsionally strong backbone and converging tendon routing (a), capable of lifting significant payloads relative to the weight of the robot (b). The design can be easily fabricated through 3D printing and accurately fabricate at small-scales (c). 16
2.2 Backbone design with repeated rhombus sections (a), a unit cell rhombus which is dictated by its width w, height h, wall thickness t and extruded depth a, (b) and a single plate model from the unit cell (c). 18
2.3 Finite element analysis of a unit cell rhombus with loading cases needed to calculate the axial rigidity (a), torsional rigidity (b), flexural rigidity about x (c), flexural rigidity about y (d), shear rigidity in x (e), and shear rigidity in y (f). 19
2.4 Experimental setups used to determine the effective axial rigidity (a), torsional rigidity (b), flexural rigidity about x (c), flexural rigidity about y (d), shear rigidity in x (e), and shear rigidity in y (f) of the unit cell. 20
2.5 Prototype robot actuation pathway (a), which utilizes (b) converging actuation rod routing, which enables strength against tip forces end-effector and (c) traditional parallel actuation rod routing that enables strength against tip moments. 23
2.6 Converging actuation rods enable translation of the tip (a) and parallel actuation routing enable bending at the tip (b). The dashed lines represent the actuation rods, with the green rods representing the parallel routing rods (3 and 5), the blue representing the converging routing rods (2 and 4) and the black dashed line is rod 1, which acts in both parallel and converging routing. 24
2.7 Actuation platform used for experiments with each component labeled. 26

2.8 Cannula guides designed using cubic Bézier curves (a) that are generated from specifying entry and distal conditions (b). Cannula guides are printed individually and attached to the actuation and backbone base plates (c). 28
2.9 Actuation mechanism used to enable compressive actuation rod loads and prevent buckling. 29
2.10 Experimental setup for calculating the compliance matrix for each pose. The 'Translation in Y' pose is shown with a 200 g pre-load attached to the end-effector that is applied in the negative y direction in O_R. 30
2.11 Candidate robot poses used in compliance analysis. The actuation rod length configurations necessary to achieve the pose and resultant compliance matrix for that pose are shown. 31
2.12 Payload carrying task with time-stamped steps. 34

3.1 Improved strength and stability of concentric tube robots using bellows.The concentric bellows pair is actuated by axially rotating the base of each individual bellows. Rotating equal amounts in opposite directions changes the bending angle in a single plane, while rotating equal amounts in the same direction changes the plane of bending. Torsional rigidity is high relative to flexural rigidity due to the bellows geometry, such that a torsionally rigid modeling assumption is accurate. 37
3.2 Possible convolution geometries using circular (a), flat (b) or v-shaped convolutions (c). Bellows can be designed to have elements from all three variations. Our 3D printed prototypes use flat outer convolutions and v-shaped inner convolutions to improve printing feasibility. 39

3.3 Convolution geometry schematic and design parameters (a) used for revolute (b) and helical bellows (c). 3D printing layer orientation along with side references used in parameter estimation and kinematic experiments are shown for both bellows. A revolute bellows pair cannot be disassembled and must be printed and precurved in the assembled state. Helical bellows can be printed and precurved separately and subsequently assembled 40
3.4 Components used to fabricate a pair of helical bellows (a). The curvature jig is inserted through the inner lumen of the bellows and enforces the new shape onto the bellows in the precurving process (b). Once precurved, inner and outer bellows attachments can be used to mount bellows onto actuation systems (c). 43
3.5 Flexural and torsional rigidity calibration of helical and revolute bellows designs. The experimental and FEA setups are shown in (a) with the flexural and torsional calibration results for the inner and outer bellows for the revolute (b) and helical (c) designs. 45
3.6 The plot shows the angle between the inner and outer bellows at the tip over a range of relative base actuation angles. The experimental setup is shown in on the left. Torsional rigidity would imply the base and tip angles to be equal (dashed line). Thus the data (right) confirms the torsionally rigid assumption of our model. 54
3.7 Manual actuation setup used in model validation experiments. The system provides rotation for both the inner and outer bellows and allows translation of inner bellows. 55
3.8 Experimental setup for measuring points along the curvature of thebellows pair (left). The outer curvature of the bellows pair were measured infive configurations in which the angles of the inner and outer bellows wereequal in magnitude but opposite in direction (right). 56

3.9 Experimental validation of torsionally-rigid kinematic model. The manual actuation setup is shown in (a) and the actuated configurations that are compared with the model are shown in (b). Experimental measurements of helical bellows at the actuated configurations are compared with the kinematic model using (i) FEA determined mechanical properties and (ii) experimentally determined mechanical properties. . 57
3.10 Payload capacity of prototype helical bellows pair with and without 100 g tip load (left) and a soft gripper demonstration (right). 59
3.11 Bellows can fabricated at scale suitable for minimally-invasive surgical applications (left) and retain large bending angles at this scale (right). 59

4.1 Illustration of a single tube with offset stiffness center with pertinent kinematic parameters labeled. 64
4.2 Examples of constant and varying stiffness center locations in relation to the tube profile. 68
4.3 Actuation and arc length variables for a two tube CPPR. The base of the slotted section of Tube 1, the outermost tube, is considered $s_1 = 0$. The distal arc length $s_1 = L$ is set to where the slotted section of Tube 1 terminates. 75
4.4 High-level flowchart the overall kinematics solutions. The dimensions, slot pattern, and material of the tubes are inputs to the FEA-based Parameter Characterization from Section 4.4 which outputs the bulk parameters of the slotted pattern. The tube parameters are used in the kineto-static model derived in Section 4.3. Actuation and external loads are inputs into the kineto-static model and the resultant shape and pose of the CPPR are the model outputs. 77

4.5 Slotted-tube pattern used to generate tube with offset stiffness centers. Slot parameters for a unit cell are shown in (a) with the 'unfolded' pattern design that is wrapped onto a nitinol tube (b). The resultant patterned tube is show from top (i), side (ii), and bottom (iii) views (c). 81
4.6 Converging tube design used for the Case 2 CPPR in which the backbone angle ϕ_i of each tube linearly tapers down the length of each tube as a function of s_i. 82
4.7 Slotted-tube pattern used for three-tube CPPR experiments. Slot parameters for a unit cell are shown in (a) with the 'unfolded' pattern design that is wrapped onto a nitinol tube (b). The patterned tube is shown from a top (i), side (ii), and bottom (ii) views in (c). Note that the additional overlaps from γ_i create additional slots on the side of the tube, thus enabling improved design of both flexural rigidity values of the tube. 84
4.8 Three point flexural test setup used to calibarate the Young's modulus E of each nitinol tube. The moduli values are then used in our FEA simulations to determine the flexural and torsional properties of our patterned tubes. 85
4.9 FEA Setups for calculating the flexural rigidity about x $(EI)_{x,i}$ (a), flexural rigidity about y $(EI)_{y,i}$ (b), and torsional rigidity $(GJ)_i$) (c). 87
4.10 Tube alignments for the two-tube CPPRs (top) and three tube CPPRs (bottom). The principal axes at the center for both alignments indicate the origin of the centerline in relation to the stiffness center locations of each tube. 89
4.11 Actuation setups for 2-tube CPPRs (top) and 3-tube CPPRs (bottom). 90
4.12 Case 1 CPPR (constant $\mathbf{r}_i$) workspace while unloaded while actuated to $\pm 3mm$ (left). Tip position of the CPPR are recorded at each pose and compared with model predictions (right). 92

4.13 Case 1 CPPR with 50 gram load applied in the plane of bending while the inner tube is actuated at 1.25mm (top). Actuated configurations from -1.25mm to 1.25mm in 0.25mm increments (bottom). 95
4.14 Case 1 CPPR with 50 gram load applied out of the plane of bending while the inner tube is actuated at 1.00mm (left). Actuated configurations are from -1mm to 1mm in 0.25mm increments (right). 98
4.15 Parameter sweep of flexural, rigidity, torsional rigidity, and stiffness center location of tubes 1 and 2 for Case 2 CPPR. 99
4.16 Case 2 CPPR prototype actuated to ±1.25mm (top) and the resultant workspace of the experimental prototype and comparison with our model predictions (bottom). 100
4.17 Case 2 CPPR prototype shown with 50g tip laod (top) and the resultant workspace with the tip load applied (bottom). 101
4.18 Three tube robot actuation poses showing displacements of just tube 2 (left), just tube 3 (middle) and both tubes in equal direction and displacement (right). 103
4.19 Workspace of three tube CPPR showing model predictions compared with experimental results. 104

Chapter 1

Introduction

1.1 Background and Motivation

Inspired by natural entities like octupus tentacles, snakes, and elephant trunks, continuum robots can achieve continuous curved shapes and can traverse complex trajectories. Their slender and compliant architecture enables them to work inside constrained and compact workspaces. These characteristics of continuum robots have shown great promise for a range of applications, which include minimally invasive surgery (MIS)[13, 14, 15, 16, 17, 18], search-and-rescue operations [19, 20], in-situ aerospace inspection [21, 22, 23, 24, 25], underwater manipulation [26, 27], and delicate material handling [28, 29, 30].

As reviewed in [13], the primary motivation in continuum robotics research medical applications. Advancements in robot design [4, 31], kinematic and statics modeling [32, 33, 34], force sensing [35, 36, 37], and control [38, 39, 40] have been investigated for a range of different actuation designs, which include tendon-driven [41], fluid-based (i.e. pnuematics and hydraulics) [42, 43, 44, 45], concentric tube robots [46], eccentric tube robots [47, 48]. Across all the actuation paradigms of continuum robots, one of the key challenges in continuum robot implementation is creating robots with sufficient strength and payload capacity. This can be a difficult problem to solve

without compromising the desired aspects of continuum robots such as compactness, weight, and range of motion. In addition, strategies for improving the strength and stability can be dependent on continuum robots with specific actuation architectures. The research in this dissertation investigates modeling and design strategies that can improve the strength and stability of continuum robots.

This introduction provides an overview on the three continuum robot actuation methods that are investigated: tendon-driven continuum robots (TDCRs), concentric tube robots (CTRs), and concentric push-pull robots (CPPRs). The working principles behind each actuation method and a brief state-of-the-art in improving the strength and stability of these robots are described for each actuation design.

1.2 Tendon-Driven Continuum Robots

TDCRs, in their simplest form, consist of a flexible backbone structure with tendons routed along the backbone as shown in Figure 1.1. When a tendon is pulled or actuated, it induces bending in the robot. The geometry of the backbone and tendon routing dictate the kinematics of the robot. TDCRs are one of the most widely used continuum robot designs [41] in the literature, as the actuation principle is highly scalable. The robots are capable of being fabricated from millimeter scales to the size of elephant trunks [32].

Developing TDCR manipulators capable of achieving wide ranges of motion while also having sufficient strength to perform load-bearing operations is challenging. There is a general trade-off in design choices; aspects that improve the overall range of motion oftentimes can limit the strength and stiffness of the robot (and vice versa). The range of motion is largely dictated by the slenderness and compliance of the TDCR backbone structure. Using materials with high elastic strain limits, such as hyperelastic nitinol and elastomers, and using long, slender backbones improve the range of motion but mitigate strength. Kinematically, continuum robots possess infinite degrees of freedom but only a few are controlled and actuated. The remaining

degrees of freedom in the system are thus dictated by actuation and external loading. There are two passive modes of deformation that limit the strength of slender TDCRs when external loading is applied:

1. In *curved* poses, out-of-plane transverse loads cause significant deflection due to the torsional deformation at the base and along the length (in addition to bending deflection).

2. In *straight*, cantilevered poses, the robot typically deflects in an s-shape deformation mode when a transverse load is applied [49]

These passive modes of deformation typically occur from a combination of the under-constrained actuation of TDCRs as well as a lack of torsional strength from the overall robot structure. Research has primarily focused on developing novel TDCR backbone designs (as shown in Figure 1.2) and manufacturing methods to improve payload capacity and strength. Utilizing endo- and exo-skeleton designs has been shown to prevent buckling and improve overall strength [50]. Backbones using rigid interlocking vertebrae were investigated by Castledine *et al.* to assess design choices and resultant range of motion and payload capacity [4]. Bellows, which have high torsional rigidity in comparison with its flexural rigidity, have also been used in pneumatic [51, 52, 53] and concentric-tube robots [54] which can drastically improve the torsional strength of the overall robot.

A number of groups have investigated origami structures, which can be tuned from geometric parameters and can be made on a wide range of scales [55, 56, 57, 58, 59, 60]. Active stiffening elements that enable control of the overall stiffness such as granular jamming [61, 62], can be housed inside manipulator structures. Shape memory alloys (SMA), which provide local stiffness control when heated, have also been integrated into backbones [6, 63]. Additionally, using combinations of actuation designs, like combining tendon and pneumatic actuation in [5], also enables local stiffness control. While many of these design strategies can improve TDCR strength, they can also introduce adverse effects which can include increasing the overall weight of the robot

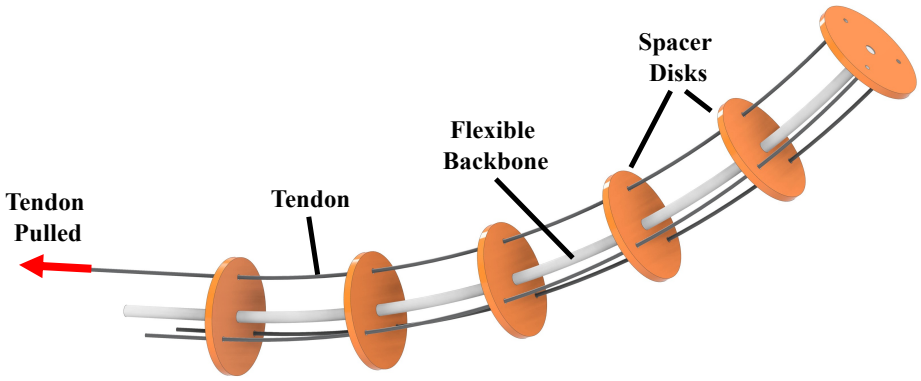


Figure 1.1: General design of a tendon-driven continuum robot (TDCR) consisting of a flexible backbone, tendons, and spacer disks that guide the tendons.

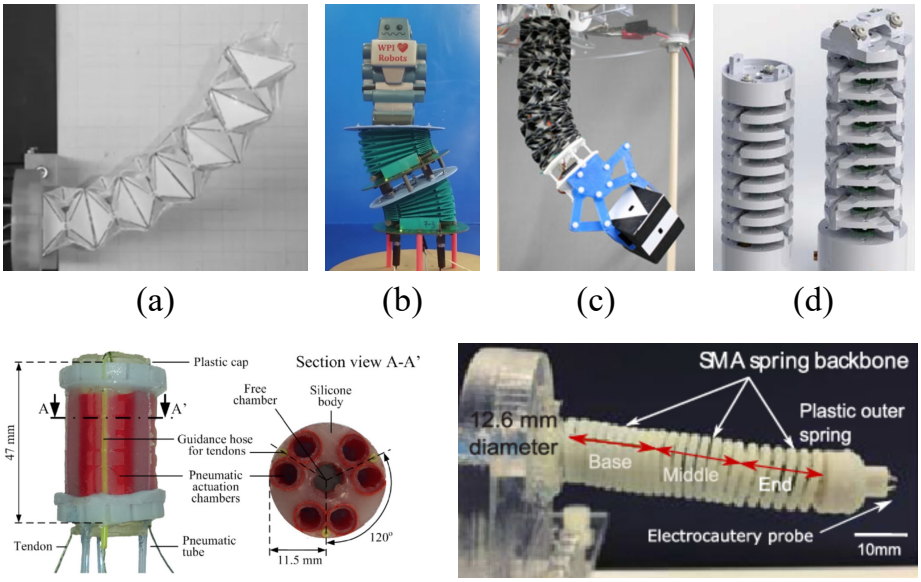


Figure 1.2: Backbone designs used in TDCRs to improve strength and range of motion, which include origami-inspired designs as shown in [1](a), [2](b), and [3](c), stacked vertebrae backbones [4](d), and active stiffening designs using combinations of pneumatic-tendon actuation [5] (e), and SMA-based heating [6](f).

and difficulty in fabrication and assembly; some designs may be limited in scale as well.

Another method for improving TDCR strength is leveraging the actuation path routing [64, 65, 66] which has recieved less attention than the design of the backbone. Case et. al. [64] used coupled cable configurations that reduce the actuator count and reduced the actuator effort. Utilizing helical tendon routing alongside straight tendon routing can greatly increase the achievable workspace as demonstrated in [65]. The majority of tendon- and rod-driven continuum robots utilize parallel actuation path routing, where the tendons or rods are parallel to the centerline of the backbone. Oliver-Butler *et al.* investigated the effects of using converging tendon routing in TDCRs, in which the tendon routing begins as an offset from the backbone and terminates at the distal end closer to the center of the backbone [67]. The converging tendon routing design can significantly reduce translational compliance at the end-effector of the robot, as well as altering the kinematics.

1.3 Concentric Tube Robots

Concentric tube robots (CTR) consist of precurved, concentrically nested tubes. Relative rotations of the concentric tubes enable new bending shapes. For a pair of concentric precurved tubes, as shown in Figure 1.3, a range of bending angles in a single plane can be achieved by rotating the two tube bases in opposite directions, if the tubes have equal flexural rigidities. The plane of bending can be changed by rotating the tube bases equal amounts in the same direction. Because CTRs can be constructed with thin-walled medical tubing such as hyperelastic nitinol, which allows for an inner lumen to pass tools through, the primary motivation of CTR research is their implementation in minimally invasive surgery (MIS) applications. Over the past fifteen years, a wide range of research has been investigated on these robots. The initial concept and kinematic models were first introduced by Webster *et al.* [68] and Sears *et al.* [69] in 2006. CTR kinematics and statics models expanded into

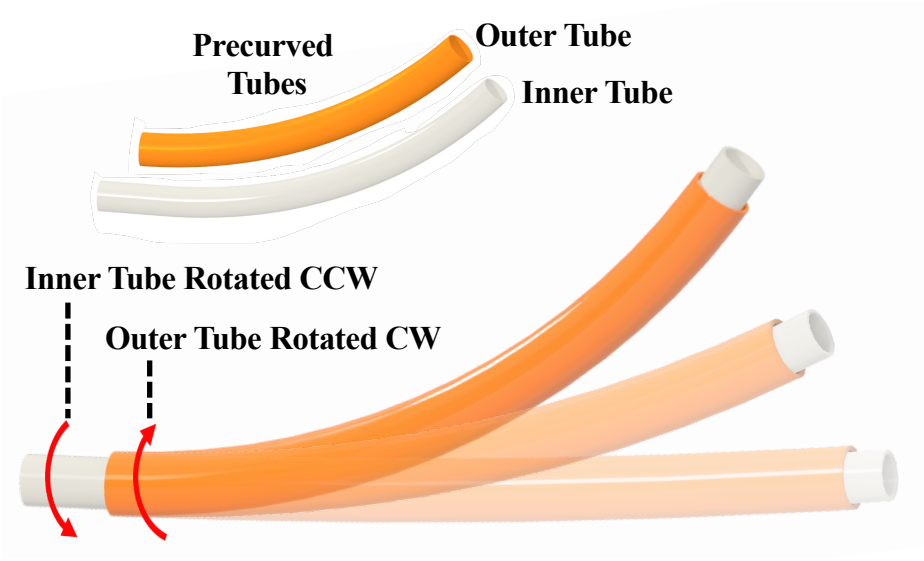


Figure 1.3: Concentric Tube Robot (CTR) consisting of two precurved tubes.

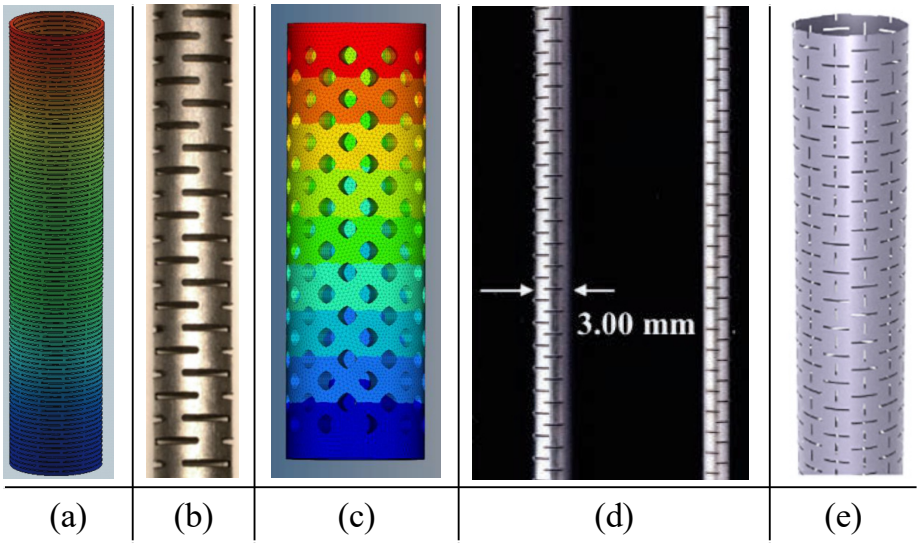


Figure 1.4: Examples of tube patterning used to reduce the flexural to torsional rigidity of the tube, using repeated slotted patterns in [7](a) and [8] (b), cellular patterns based on topology optimization results in [9](c), and asymmetric patterning in [10](d). Auxetic patterns also enable control over flexural and torsional rigidity values of the tube [11](e).

more general models that account for multiple tubes, external loading, and friction [70, 71, 72, 73], control methods [74], actuation design [75, 76, 77, 78], path-planning strategies [79, 80, 81, 82], patient-specific optimized designs [83, 84, 81], and shape estimation [85, 86, 87].

However, one of the fundamental challenges of this robot is the problem of 'snapping' - an instability that arises due to the torsional compliance of the tubes. When a CTR is actuated to a 'snapping' configuration, the CTR will 'snap' to a more stable energy state. Webster *et al* in [88] developed a model to study the energy landscape, demonstrating the need for including torsion in kinematic models. Elastic stability tests for CTRs in free space [89] and while loaded [90] have been developed, as well as dynamic models [91, 92]. In addition to the snapping problem, torsional compliance also allows static friction to affect the robot configuration in a hysteretic way, which further complicates the kinematics. For a thin-walled tube, the torsional rigidity GJ is much smaller than its flexural rigidity EI, solely by the geometry of the tube (where E represents the Young's modulus of the tube material, I is the second moment of area of the tube, G is the shear modulus of the tube, and J is the polar moment of area). [89, 93, 90]; there is even one paper that has leveraged this instability for high-force application [94].

To mitigate the problem of snapping, research into control strategies and novel tube designs (with examples shown in Figure 1.4) have been investigated. Path planning algorithms have been developed to achieve stability while traversing an intended goal or trajectory. Bergeles *et al*. utilized a rapidly exploring random trees algorithm for planning a desired clinical trajectory (minimimilly invasive cauterization of hydrocephalus in the brain using a patient CT-scan) while maintaining local stability during path traversal [79]. Hendrick *et al*. used bifrucation theory to design precurvatures of CTRs consisting of arbitrary number of tubes, that are globally stable [95]. Fellmann *et al*. evaluated synchronous and asynchronous actuation velocities for path-planning to design collision free trajectories [96]. Leibrandt *et al*. used a multi-processor approach to design stable CTRs in collision free trajectories [82, 97].

In terms of tube design strategies, the goal of tube patterning to reduce the flexural rigidity EI, relative to the tube's torsional rigidity GJ. The ratio EI/GJ has been widely used as a common reference metric in the literature. Azimian *et al.* initially hypothesized the use of leveraging the mechanical design of the tube, proposing the use of multi-layered helical tubing and laser-machining auxetic and cellular patterns onto tubes to achieve a lower EI/GJ ratio [7]. Kim *et al.* in [98] investigated the role of using anisotropic patterning, using a series of overlapping slot patterns down the length of the tube, to alter the EI/GJ [98] and Lee *et al* developed analytical models that predicted the resultant EI and GJ of their anisotropic patterning [8]. Xin Jue Luo *et al.* investigated the use of topology optimization that minimized EI/GJ, using the ratio of torsional compliance to flexural compliance as the objective function [9]. Finally, Rucker *et al.* explored the design of tranverse anistropic patterning (i.e. direction-dependent flexural rigidities) in which stability can be achieved while retaining more tube stiffness. However, even though patterned tube design approach can mitigate the effects of 'snapping,' the tube patterns can still suffer from torsional lag and kinematic inaccuracies due to frictional hysteresis. Furthermore, even with patterning, tubes can still poses unstable configurations at sufficiently large precurvatures.

1.4 Concentric Push Pull Robots

Concentric push-pull robots (CPPR) are continuum manipulators that consist of concentrically nested, asymmetrically patterned tubes that are fixed together at their distal ends as shown in Figure 1.5. Relative translations of the tubes generate bending in the overall CPPR structure. Such asymmetrically patterned tubes can be fabricated using a number of different methods, including laser machining [99, 100, 10, 8, 7], conventional milling [101, 102, 103], and 3D printing [104],[99]. Like pre-curved concentric tube robots (known as CTRs), CPPRs can be fabricated at millimeter scales and are capable of traversing complex and tortuous pathways,

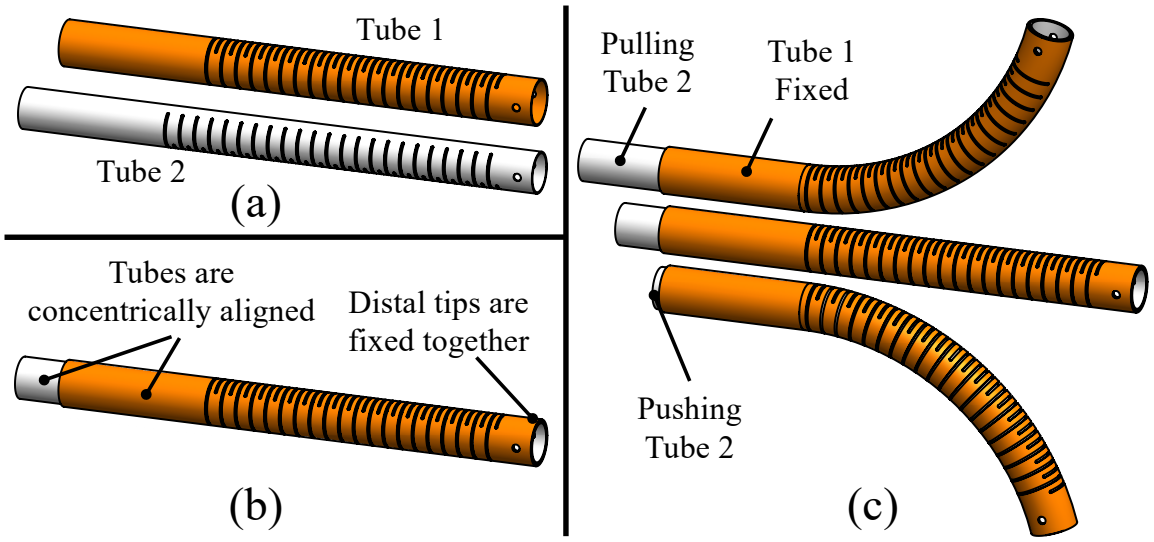


Figure 1.5: Concentric Push-Pull Robot (CPPR) consisting of two asymetrically patterned tubes.

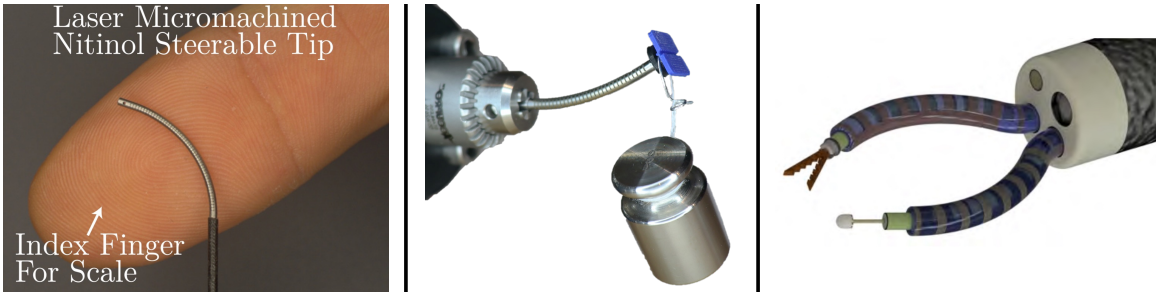


Figure 1.6: CPPRs can be fabricated at needle-sized scales (left). Ch. 4 details the derivation and validation of the first kinematics model for CPPRs in the literature, which can account for external loads (middle) and robots using more than two tubes. This model will be useful in the design and analysis of CPPRs for MIS applications (image from [12]) (right).

making them suitable manipulators for minimally invasive surgery (MIS) applications [13]. However, unlike CTRs, CPPRs are able to achieve a wide bending range of motion without the elastic instabilities found in CTRs [89],[105].

For CPPRs, the additional tube is capable of withstanding tension and extension, enabling bending in both directions through relative translations (i.e. pushing and pulling) of the tubes. Using thin-walled tubes enables a large inner lumen space for passing through surgical tools such as grippers, cameras, and illumination. The additional tube in CPPRs increases the overall stiffness of the manipulator, enhancing its strength and capabilities for load-bearing surgical applications such as tissue traction. In previous CPPR research, Euler-Bernoulli beam theory was used to model the bending of small 'notched' sections of the tube to create a forward kinematics model for CPPRs. The parameters of the design, which includes the spacing and size of the rectangular notches, dictate the overall bending shape of the CPPR when actuated [99]. However, this existing work is limited to large rectangular notches, planar shapes, and CPPRs consisting of pairs of distally attached tubes (not more than two attached together). CPPRs with large rectangular notches can interlock between the inner and outer tube when actuated, can cause Brazier buckling (an unmodeled deformation effect) at large bend angles, and create a source of pinching when interacting the environment, a potential safety hazard for MIS applications. In addition, the influence of external loading and the overall stiffness of the device has yet to be modeled. CPPRs have successfully demonstrated tumor resection in a ex vivo models [12]. The ability for the model to account for external loading is key in designing these robots for load-bearing applications. Novel design opportunities in CPPRs, such as using more than two tubes, have yet to be investigated and modeled. In addition, more advanced slot patterns with improved mechanical properties could greatly improve the overall performance of CPPRs [11, 106] but these patterns cannot be modeled with previous kinematic models. Having a model that includes these additions are important for analyzing more general designs, expanding the possible design optimization of CPPRs and developing the technology further for

MIS applications. Mechanics models such as Kirchhoff rod and Cosserat rod models have been used to model a range of continuum robot designs, including tendon-driven continuum robots [107, 34, 108, 33], CTRs [109, 110, 71, 74, 70], parallel continuum robots [111, 112], fluid-actuated continuum robots [113],[114] and new eccentric tube robots [47, 48]. These models are useful in that the kinematics can be efficiently computed [112] and can capture external loading and arbitrary numbers of additional tubes and rods. However, the CPPR actuation paradigm presents a number of unique challenge not present in other continuum robots. The stiffness centers of the tubes used in CPPRs are not coincident with the centerline, which is the case for CTRs, and the stiffness centers can vary along the length of the tubes. The modeling derivation in Ch. 4 shows how the concentricity constraint for tubes with offset and varying stiffness centers introduces additional modeling complexity. Casting the kinematics as an energy minimization problem has also been used on tendon-driven [107], concentric tube [88], and parallel continuum robots [115], where the shape and pose of the continuum robots are parameterized. The energy minimization method also enables the inclusion of conservative external loading into the system.

1.5 Outline and Contributions

This dissertation covers modeling and design advancements to improve the strength and stability of the previously discussed continuum robot actuation paradigms. Chapter 2 investigates the implementation of a novel backbone design and tendon routing that can improve the strength and stability of TDCRs. A novel backbone design is investigated and an FEA-based model is used to analyze the axial, torsional, flexural, and shear rigidities of the backbone. A robotic platform is created to validate the proposed strength-improving strategies by experimentally characterizing the compliance of the robot at pertinent poses. The strength-improving concepts used in the backbone design and the tendon routing are then successfully demonstrated experimentally by having the robot perform a pick-and-place task, with minimal

oscillatory vibrations while the robot was performing the task, carrying a payload that is over 5 times the weight of the backbone.

Chapter 3 covers the development of a new bending continuum robot, concentric precurved bellows, that are based on the concentric tube robot actuation paradigm. The work in this chapter greatly mitigates the torsional compliance in CTRs, a key instability for this actuation paradigm. This instability from torsional compliance allows a dangerous phenomena called 'snapping' to occur when sufficient elastic energy is stored and released. The use of bellows tubing enables high torsional stiffness while enabling low flexural stiffness which virtually eliminates instability. Two novel bellows designs are developed and analyzed. Parameter characterization of bellows prototypes are conducted through static FEA simulations and on 3D printed prototypes. A torsionally rigid kinematic that accounts asymmetric flexural rigidity is derived and validated on experimental prototypes. Fabrication techniques are explored that enable fabrication at large- and small-scales of these robots are also explored and a soft robotic gripper is constructed using concentric precurved bellows to demonstrate its effectiveness in payload tasks.

Chapter 4 covers modeling advancements of CPPRs and validation experiments therein. While previous kinematic models have been accurate for CPPRs under limited assumptions, this modeling will expand the analysis of the load bearing capacities of these robots as well enable modeling of more complex CPPRs that are capable of non-planar bending, large deflections, and constructed from more than two tubes. The model will be used to analyze how varying tube properties can affect the CPPRs resistance to tip forces.

Chapter 2

Improving Strength in Tendon-Driven Continuum Robots

2.1 Disclosure of Previously Published Material

The work presented in this chapter has been published in Frontiers of Robotics and AI [116]. The dissertation author served as first author on this publication and D. C. Rucker, the chair of this dissertation's committee, was second author and provided guidance and support throughout the paper writing process.

2.2 Overview

The research in this chapter addresses the problems of the under-constrained nature of tendon-driven continuum robot (TDCR) actuation and insufficient torsional stiffness by investigating (1) a novel flexible backbone design and (2) novel actuation routing paths. The specific geometry of both these design choices helps to increase the load bearing capacity at the end effector without sacrificing actuatable range of motion. The backbone is designed using an extruded thin-plate rhombus pattern for the backbone that is lightweight, torsionally stiff, and simple to manufacture.

Additionally, actuation rods are routed through the backbone in both parallel and converging paths to eliminate the main underactuated bending modes. This creates a 5-DOF robot, as shown in Figure 2.1(a) and (b), capable of both bending and translation motions with high output stiffness throughout its workspace. This robot concept can be fabricated at both large scales with conventional fused filament fabrication and at small scales with stereolithography as shown in Figure 2.1(c).

2.2.1 Novel Backbone Design with High Torsional and Shear Stiffness

The backbone structures of continuum robots are a fundamental component in the bulk mechanical properties and performance of the robot. The novel backbone design is shown in Figure 2.2 (a). The backbone consists of a repeated rhombus unit cell which has a height h, width w, wall thickness t, and extruded depth a as shown in Figure 2.2 (b). The modes of deformation that occur within this unit cell arise due to bending and warping from the individual plates that connect the structure into a rhombus. Investigating the deformation in a single plate of the unit cell as shown in Figure 2.2 (c), one can intuitively understand the performance using conventional stiffness characterizations from mechanics of materials. If a single thin-walled plate is considered as a beam, the flexural rigidity about x_2 is far greater than the flexural rigidity about x_1 if the extruded depth a is far greater than the thickness t. In addition, if the plate has small thickness relative to its width, it is relatively compliant when a torque is applied about the x_3 axis. With these beam deformations in mind, we can intuitively see that the unit cell should be able to easily bend about the x and y axes, but it will resist torsional deformation about z with high rigidity (because this would require the individual plates to bend about the x_2 axis in Figure 2.2(c)).

To verify that this intuitive design achieves our purpose, experiments were conducted on 3D printed unit cells and in simulation using the FEA package Nastran In-CAD, a Nastran plug-in for Autodesk Inventor, to determine the mechanical

properties of the unit cell. The dimensions of the unit cell that was analyzed are tabulated in Table 2.1.

Six loading cases were conducted to determine the effective flexural rigidities EI, the axial rigidity AE, torsional rigidity GJ and shear rigidities GA of the unit cell. The FEA and experimental setups are shown in Figure 2.3 along with the model equations used to estimate the effective rigidity values of the unit cell. For the axial and flexural tests, the distal vertex of the unit cell is free to rotate and translate. For the torsional test, the distal vertex is constrained from translating in the z-direction. For the shear tests, the distal vertex is constrained to only translate in the direction the tip load is applied in; this vertex is also constrained from rotations about the x- ,y-, and z-axes. For the effective AE, $(GA)_x$, and $(GA)_y$ rigidity values, a linear force F_i is applied to the distal end of the unit cell and the resultant displacements δ_i are recorded. For the effective GJ, $(EI)_x$, $(EI)_y$ rigidity values, a moment M_i is applied and the resultant rotations θ_i are recorded. Forces at 0.1N and moments of 0.005 Nm were applied in the simulation to ensure the small deformation assumption and stay within the linear elastic region. The FEA model in Nastran uses shell elements of parabolic order and the element size was selected to be 1mm. Both FEA and experimental setups assume linear elastic material behavior and small deformation. For a backbone that utilizes multiple unit cells, while the overall structure is capable of large bending angles and translations, the individual unit cells remain in the small deformation regime. Due the anisotropic nature of 3D printing [117], the FEA simulations used a calibrated Young's modulus E of PETG, the print material used in the physical prototypes. The Young's modulus was calibrated using a three-point flexural test on a sample printed PETG beam:

$$E = \frac{L^3 m}{4bd^3} \tag{2.1}$$

where L is the supported length of the beam, m is the slope of the load-deflection curve, b is the width of the beam, and d is the depth of the beam. The PETG sample

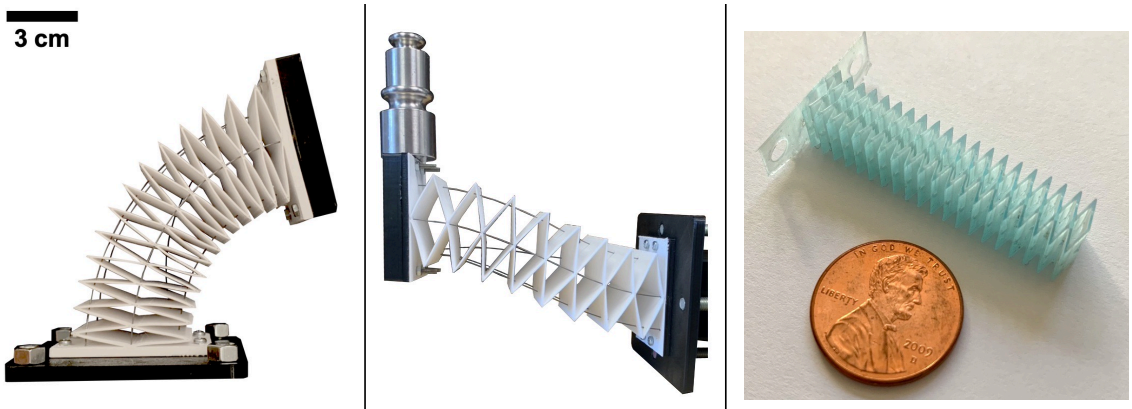


Figure 2.1: Strength-improved TDCR using a torsionally strong backbone and converging tendon routing (a), capable of lifting significant payloads relative to the weight of the robot (b). The design can be easily fabricated through 3D printing and accurately fabricate at small-scales (c).

Table 2.1: Dimensions of unit cell design used in experiments

Parameter	**Value**
Unit cell width, w	50 mm
Unit cell height, h	12 mm
Extruded depth, a	50 mm
Wall thickness, t	0.8 mm

beam used in the three-point flexural test had a length of 40 mm, a depth/thickness of 0.8 mm and a width of 15 mm. To find the slope of the load-deflection curve, we apply a range of small deflections to the midpoint of the beam using a manual linear rail with an attached digital displacement scale and record the corresponding force readings using a force gauge (Beslands HF-50). The Young's modulus E was calculated to be 1.22GPa, similar to other reported 3D Printed PETG [117].

For the experiments with unit cell prototypes, the design was 3D printed specified in Table 2.1 using MatterHackers PETG on a MakeIt Pro-M 3D printer. The unit cells were fabricated using a nozzle temperature of 245^{o}C and a bed temperature of 60^{o}C. Ultimaker Cura was used to slice the part and allowed control over the number of wall layers in the part. Because the nozzle diameter of the printer was 0.4mm, two wall layers were used to achieve our 0.8mm wall thickness.

A manual force stand, displacement scale and force gauge used in each of the experiments are labeled in the experimental setup for determining the effective axial rigidity of Figure 2.4 (a). This is the same equipment used in the three-point flexural test to calibrate the Young's modulus of the PETG that was used. For each mechanical property case, the load-displacement relationship is generated by applying a range of deformations to the unit cell and measuring the resultant reaction force using a force gauge (Beslands HF-50). A linear fit is performed for each set of load-displacement data using the method of least squares. The slopes of the linear fit lines correspond to the F_i/δ_i and M_i/θ_i (where $i = x, y, z$) in the equations in Figure 2.3. The experimental mechanical properties are then found by multiplying these slopes by the height h of the unit cell. To constrain the unit cell to only rotate about its z-axis, a bearing mount is attached to the unit cell's distal plate. For the torsional and flexural rigidity experiments, an 8020 aluminum extrusion frame is attached to the tip and used as a moment arm for the force gauge. A rectangular cap that is attached to the 8020 frame is used as a contact point for the force gauge tip and is positioned to set the moment arm distance from the center of the unit cell, which are denoted as r_{GJ} and r_{EI} in Figure 2.4 (b)-(d). The moment arm in the torsional experiment r_{GJ}

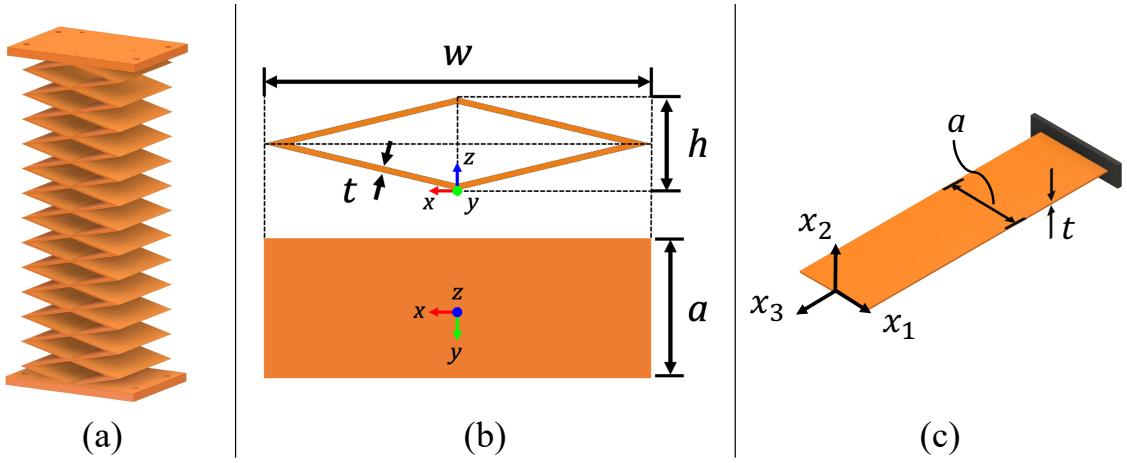


Figure 2.2: Backbone design with repeated rhombus sections (a), a unit cell rhombus which is dictated by its width w, height h, wall thickness t and extruded depth a, (b) and a single plate model from the unit cell (c).

Table 2.2: Mechanical properties of unit cell from FEA and experimental setups.

Unit Cell Mechanical Property	**FEA Value**	**Experimental Value**
Axial Rigidity, AE	77 N	77 N
Torsional Rigidity, GJ	4.68 Nm^2	1.79 Nm^2
Flexural Rigidity about x, $(EI)_x$	0.029 Nm^2	0.024 Nm^2
Flexural Rigidity about y, $(EI)_y$	0.016 Nm^2	0.015 Nm^2
Shear Rigidity in x, $(GA)_x$	178 N	195 N
Shear Rigidity in y, $(GA)_y$	7,600 N	589 N

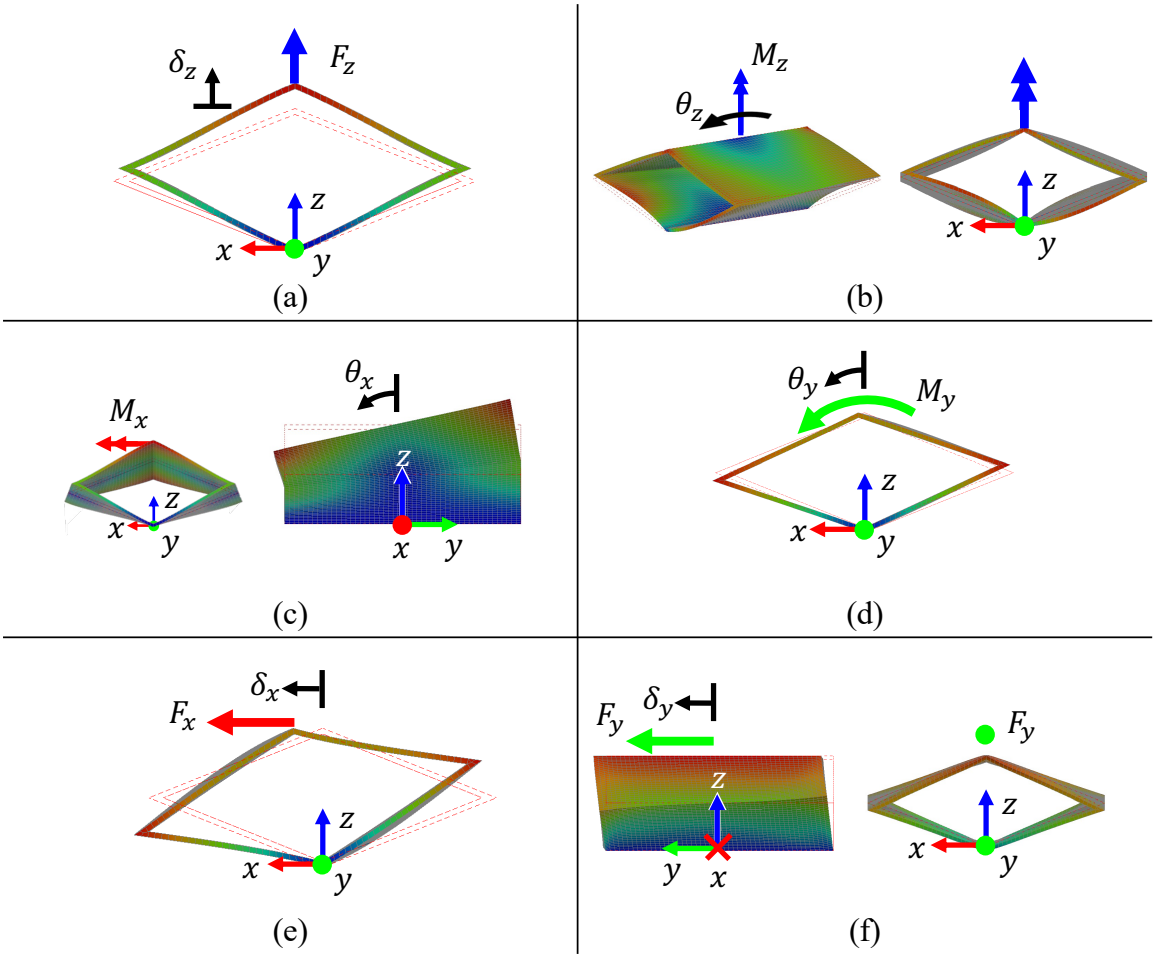


Figure 2.3: Finite element analysis of a unit cell rhombus with loading cases needed to calculate the axial rigidity (a), torsional rigidity (b), flexural rigidity about x (c), flexural rigidity about y (d), shear rigidity in x (e), and shear rigidity in y (f).

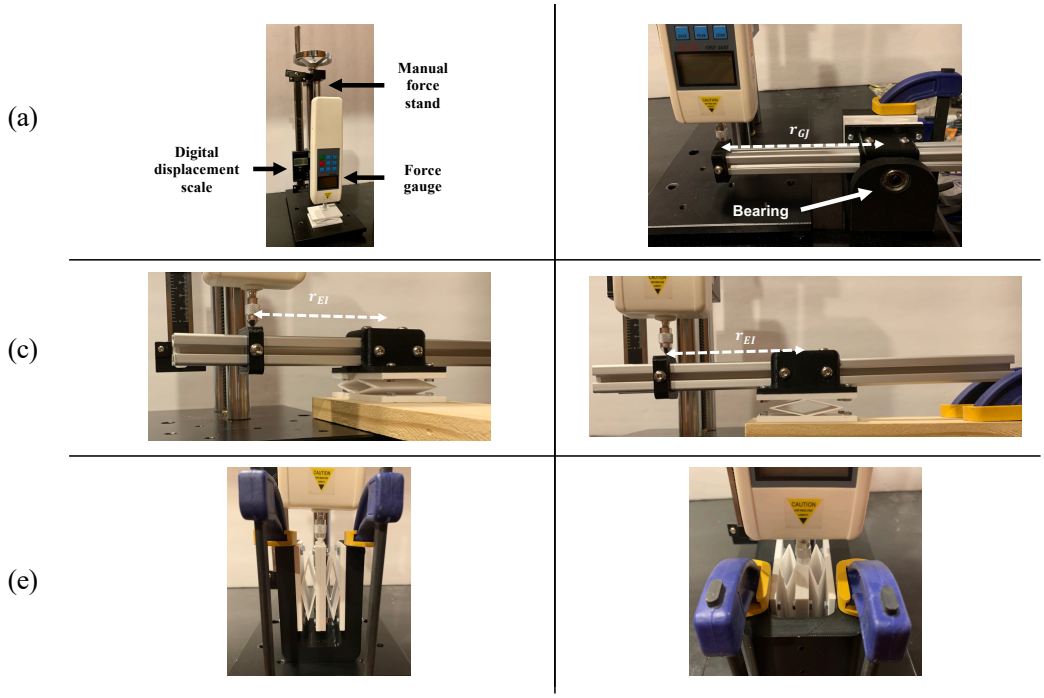


Figure 2.4: Experimental setups used to determine the effective axial rigidity (a), torsional rigidity (b), flexural rigidity about x (c), flexural rigidity about y (d), shear rigidity in x (e), and shear rigidity in y (f) of the unit cell.

has a length of 150mm and the moment arm in both flexural experiments r_{GJ} have a length of 100mm. The applied moments for the torsional and flexural are computed as $M_z = r_{GJ}F_m$ and $M_x = M_y = r_{EI}F_m$ where F_m is the measured force applied by the force gauge. Using a small angle assumption, these moment arm lengths are also used to calculate the angular deflections θ_i exhibited by the torsional and flexural cases which is simply $\theta_i = r_i\delta_m$ where δ_m is the displacement applied to the 8020 frame at the moment arm distance location.

For the physical shear rigidity experiments, two unit cells are attached together at their end plates. The base plate of the two unit cells are fixed within in a U-shaped jig as shown in Figure 2.4 (e) and (f). Applying a force at the midpoint between the attached two unit cells plates enforces translation in the direction of force without additional rotation or translation deflections. It should be noted that because two unit cells are connected in parallel for the shearing experiments, the resulting load-deflection data would correspond to the shear rigidity of two unit cells. The effective shear rigidity values $(GA)_x$ and $(GA)_y$ for a single unit cell are simply half the shear rigidity values of the two combined unit cells.

The mechanical properties predicted by FEA were in close agreement with experimental results, as tabulated in Table 2.2. While the FEA simulation predicted that the torsional rigidity GJ and shear rigidity $(GA)_y$ to be much greater than what was experimentally determined, the discrepancy is likely due to small deflections in the support fixtures for these experiments. Furthermore, both FEA and experiments confirm that the stiffness of these modes is very high, so that continuum robot deformations will be primarily caused from bending and axial deformation, which was the design goal of this research. The experimental torsional rigidity is greater than the flexural rigidities $(EI)_x$ and $(EI)_y$ by factors of approximately 75 and 119 respectively. Additionally, we can see that the experimental shear rigidities $(GA)_x$ and $(GA)_y$ are approximately 2.53 and 7.65 times greater than the axial rigidity AE. For comparison, a rod with a simple circular cross section has torsional rigidity of just $1/(1+\nu)$ times its flexural rigidity, and a shear rigidity of $1/[2(1+\nu)]$ times its axial

rigidity, where ν is Poisson's ratio of the example backbone. If this rod was made of steel (ν=0.3), the torsional rigidity would only be 0.77 times its flexural rigidity and the shear rigidity would only be 0.38 times its axial rigidity. These experiments confirm the assumptions that the rhombus unit cell design enables a backbone high torsional rigidity relative to its flexural rigidity. In addition, when using calibrated material properties, FEA can be used as design tool to achieve a rhombus backbone design with desired mechanical properties.

2.3 Tendon Routing for Tip Load Resistance

While having a backbone with high torsional rigidity can greatly improve its payload capacity, the design of the actuator routing paths can also be used to increase output stiffness. As shown in Figure 2.5 (a), continuum robots with parallel actuator routing exhibit an s-shaped deformation mode when a transverse tip force is applied to the end-effector. However, the parallel actuator routing resists moment loads with high stiffness. Conversely, as shown in Figure 2.5 (b), robots with converging routing paths exhibit deformation when tip moments are applied, but resist direct tip force loading with high stiffness because the non-parallel actuation forces (tension or compression) are capable of producing a resultant in the opposite direction of the tip load. Thus, using both converging and parallel actuation routing simultaneously provides high stiffness with respect to both forces and moments at the tip.

If the backbone has a high torsional rigidity that is much greater than its flexural rigidities, this also means that the angular twist degree of freedom about the robot's z-axis (direction of backbone length) will be constrained. Therefore, only five actuation rods are necessary to control the remaining five degrees of freedom - translations in x, y, and z angles about the x- and y-axes. The converging actuation rods enable three translation motions of the tip while the parallel actuation rods enable two bending motions at the tip as shown in Figure 2.6.

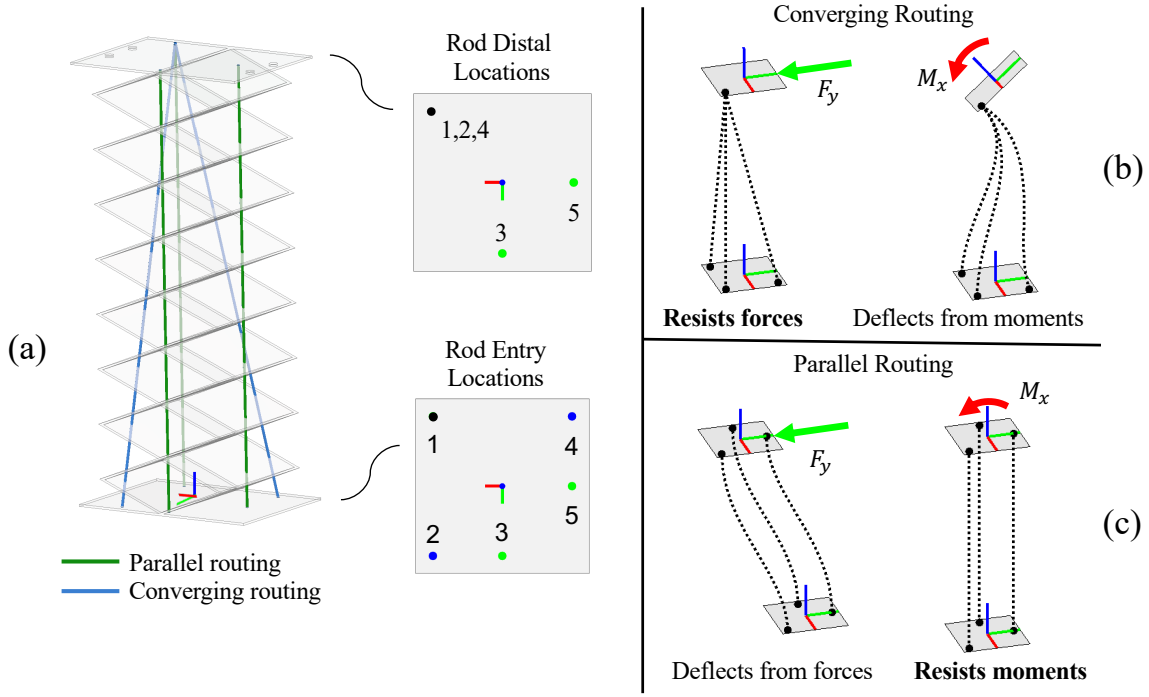


Figure 2.5: Prototype robot actuation pathway (a), which utilizes (b) converging actuation rod routing, which enables strength against tip forces end-effector and (c) traditional parallel actuation rod routing that enables strength against tip moments.

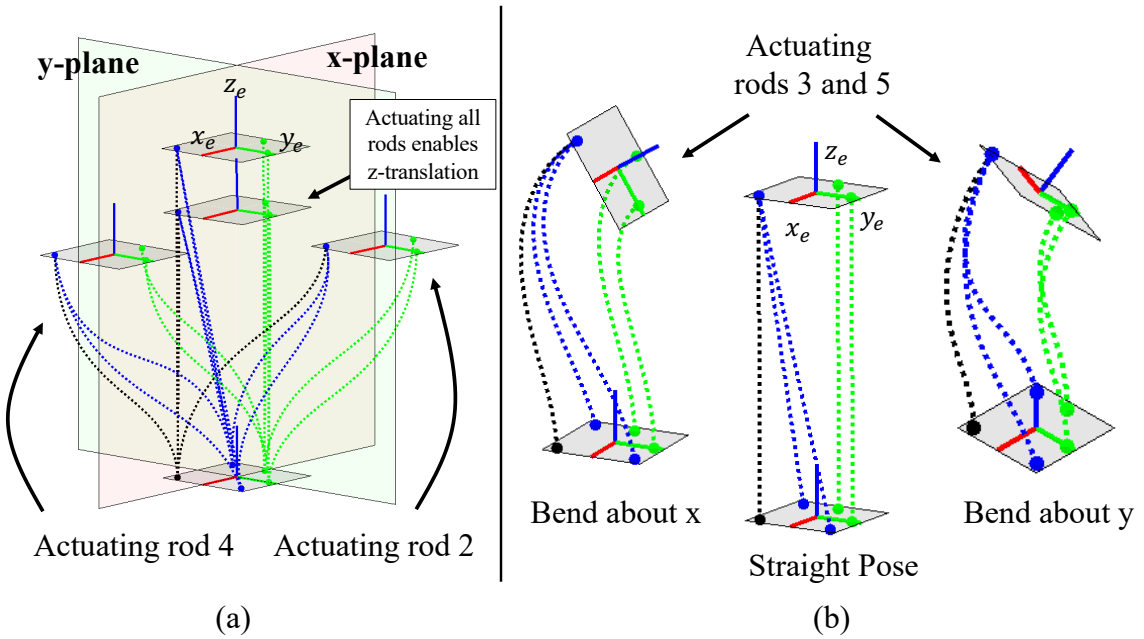


Figure 2.6: Converging actuation rods enable translation of the tip (a) and parallel actuation routing enable bending at the tip (b). The dashed lines represent the actuation rods, with the green rods representing the parallel routing rods (3 and 5), the blue representing the converging routing rods (2 and 4) and the black dashed line is rod 1, which acts in both parallel and converging routing.

If the actuation rods are able to withstand both compression and tension, then the robot can achieve symmetric motions within its workspace. Furthermore, the actuation routing is designed such that none of the actuation rods pass through the centerline of the backbone. This allows inner channels to be created within the backbone which would allow devices at the end-effector such as grippers, sensors or cameras to have their cables pass through the backbone.

2.4 Robot Embodiment

An actuation setup was designed and fabricated to experimentally test the proposed design paradigm for leveraging backbone and actuation routing geometry. There are four sections of the robot: (1) the rhombus backbone, (2) the cannula guides, (3) the anti-buckling structures, and (4) the actuation pack assembly. The complete actuation setup and details of its sections are shown in Figure 2.7. NEMA 17 non-captive linear stepper actuators translate the spring-steel actuation rods. Relative to the mechanical properties of the backbone, the actuation rods contribute an insignificant amount of bending stiffness to the structure. For the backbone, we used 13 repeated unit cells of equal dimension were used, resulting in a backbone bounded by a 50x50x165mm rectangular prism. The repeated unit cell dimensions are tabulated in Table 2.1. Using an Ohaus CS 5000 weight scale, the mass of the backbone was measured to be 73 grams (without actuation rods inserted).

2.4.1 Tendon Pathway Guides

To achieve the parallel and convergent actuation routing paths that run in straight lines from the base of the backbone to the tip, a set of curved rigid cannula guides were designed that allow the actuation rods pass through on their way from the pack of linear actuators to the backbone. These rigid cannula guides solve three challenges: (1) they allow converging actuation rods 2 and 4 to enter into the backbone at their

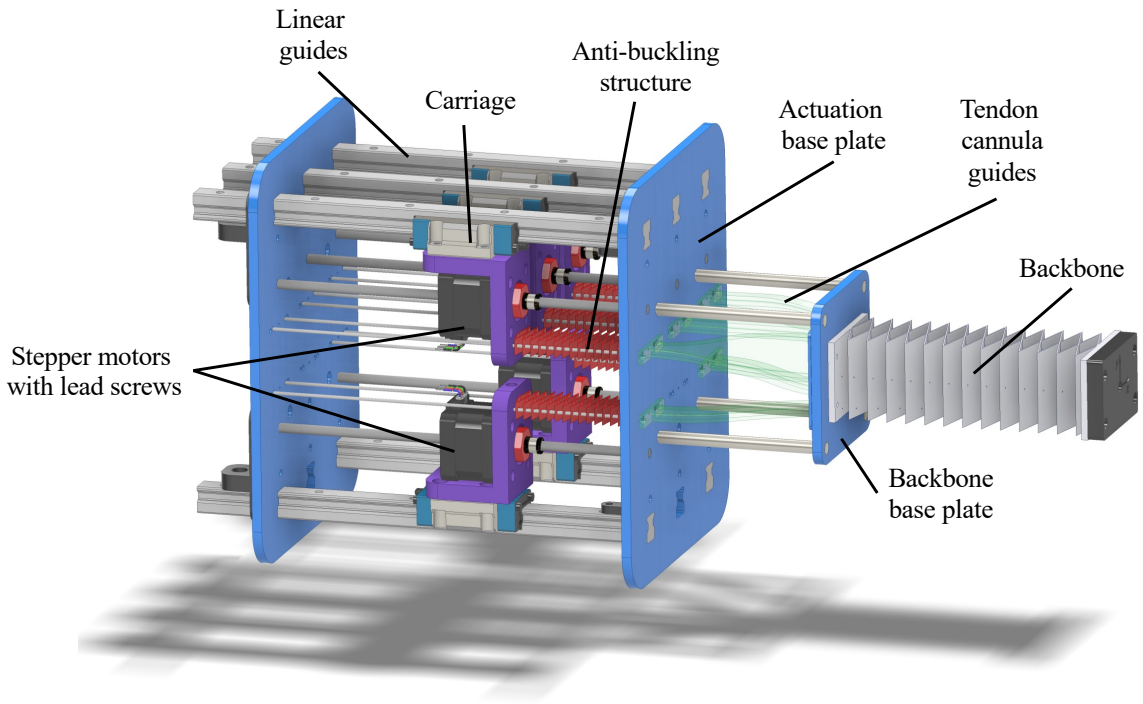


Figure 2.7: Actuation platform used for experiments with each component labeled.

prescribed angles, (2) they prevent rod buckling between the actuation base plate and the backbone base plate, and (3) they allow the linear actuators to be spaced without interference. Cubic Bézier curves were used to design the guides to satisfy the point-slope entry and distal conditions. Figure 2.8 shows the Bézier curves that route each actuation rod through the actuation base plate and into the backbone base plate where the tendons are then inserted through the backbone. Each curve was designed by specifying the entry and distal point and slope conditions for each rod as shown in Figure 2.8. The entry conditions for a single actuation rod consist of the entry location on the actuation base plate p_a in the O_a reference frame and the entry slope p'_a. For each rod, the entry slope condition is always straight i.e. $p'_a = [0, 0, 0]^\top$. The distal condition p_b specifies the rod entry locations into the backbone base plate (in the O_a frame) and p'_b specifies the slope of the rod as it enters the backbone base plate.

2.4.2 Anti-Buckling Tendon Mechanism

To allow for push-pull actuation, there is a free length of the actuation rods between the stepper motor carriage and the actuation base plate. To prevent the rods from buckling in this region before entering the cannula guides, a smaller version of the rhombic backbone structure was used to create an anti-buckling mechanism between the actuators and the robot backbone. The schematic of this diagram is found in Figure 2.9. The mechanism consists of a small-scale version of the rhombus backbone that allows the actuating rod to pass through the center of the structure. Two steel rods are routed through the miniature backbone structure to increase its resistance to buckling when in compression. These support rods are fixed between the plates attached to the backbone structure and the actuator base plate.

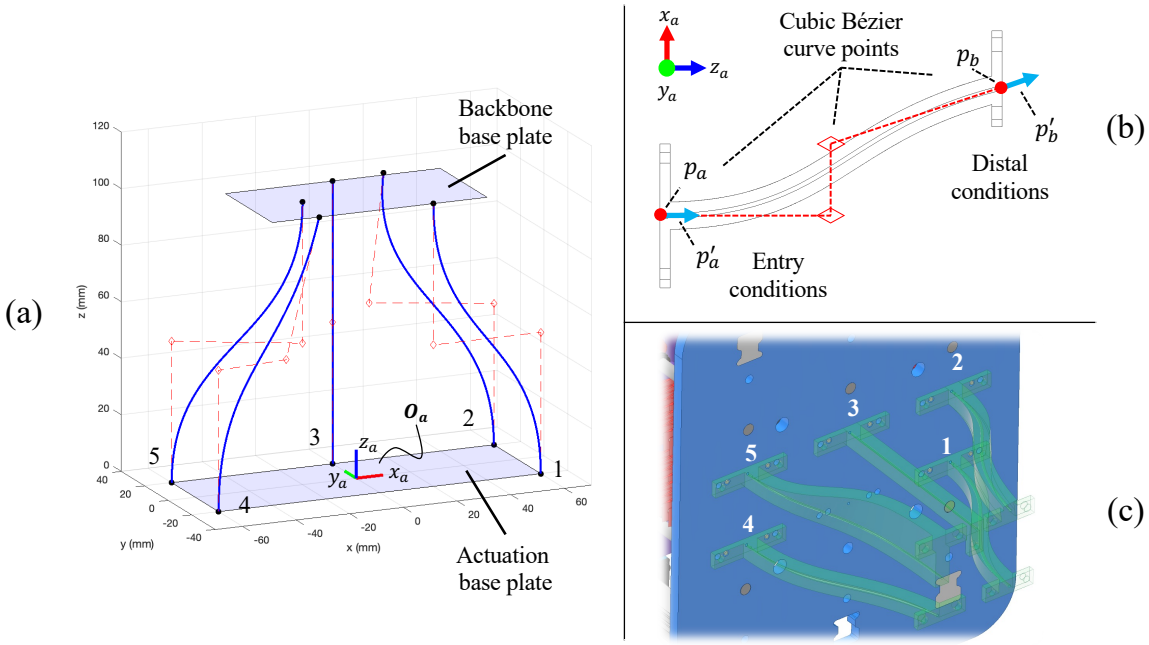


Figure 2.8: Cannula guides designed using cubic Bézier curves (a) that are generated from specifying entry and distal conditions (b). Cannula guides are printed individually and attached to the actuation and backbone base plates (c).

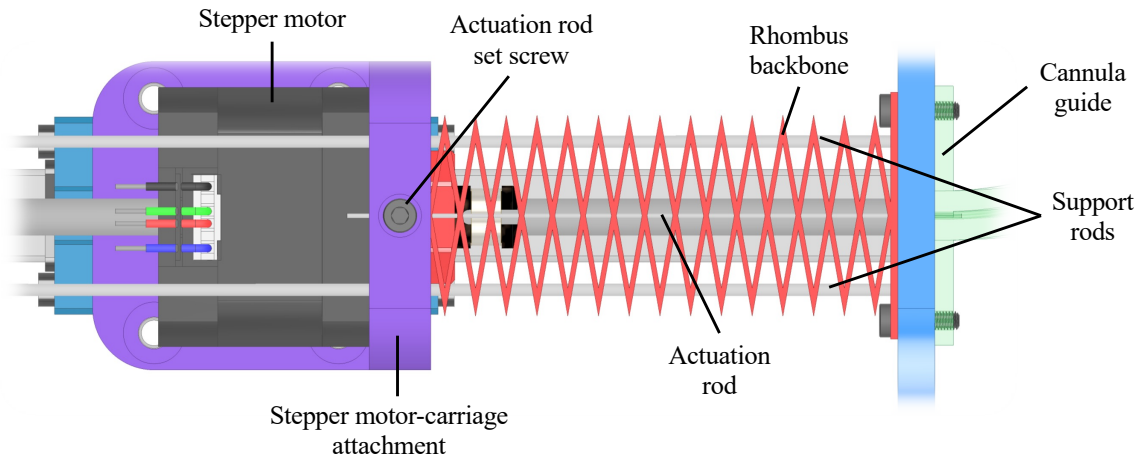


Figure 2.9: Actuation mechanism used to enable compressive actuation rod loads and prevent buckling.

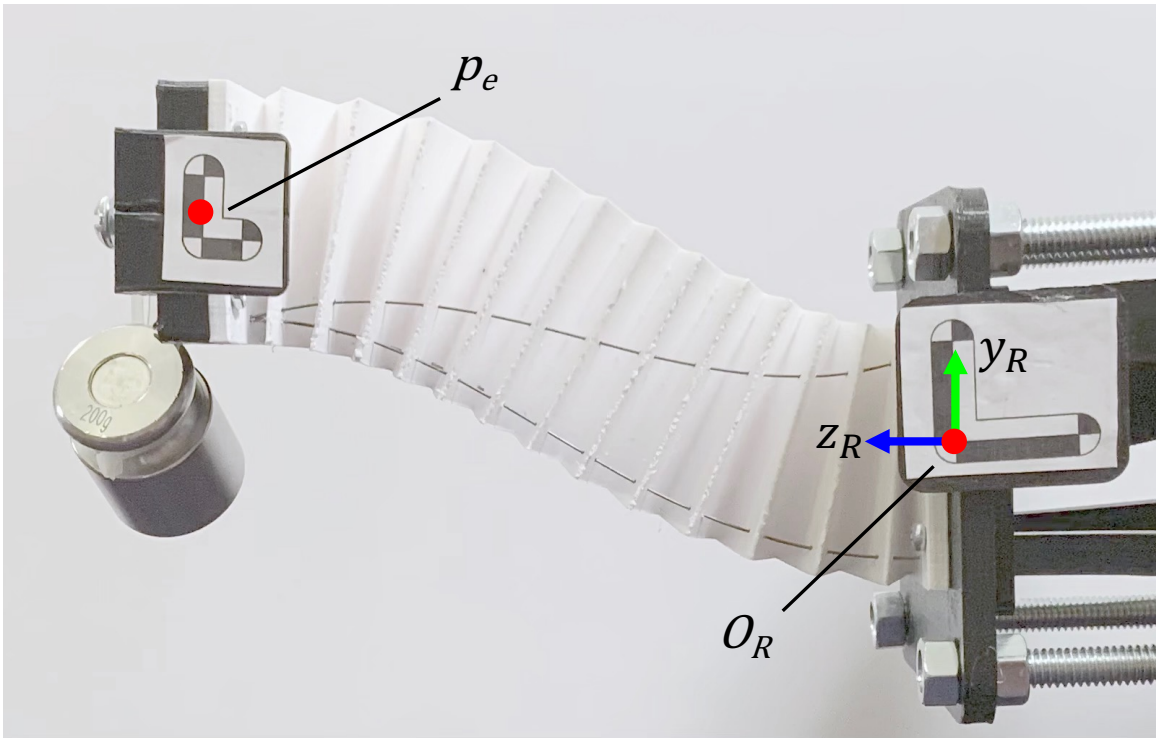


Figure 2.10: Experimental setup for calculating the compliance matrix for each pose. The 'Translation in Y' pose is shown with a 200 g pre-load attached to the end-effector that is applied in the negative y direction in O_R.

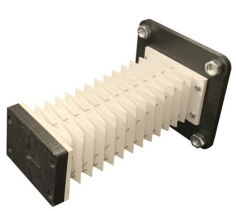
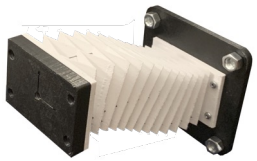
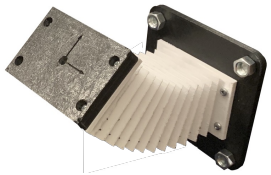
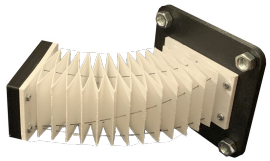
	Straight Pose	Translation in X	Translation in Y	Bending About X	Bending About Y
Actuated Pose					
Rod Lengths (mm)	[160 165 160 165 160]	[160 165 160 185 160]	[160 145 160 165 160]	[160 140 120 165 140]	[160 165 135 140 110]
Compliance Matrices (mm/N)	$\begin{bmatrix} 1.13 & -0.41 & -0.04 \\ -0.47 & 1.08 & 0.07 \\ -0.34 & 0.09 & 0.29 \end{bmatrix}$	$\begin{bmatrix} 0.36 & -0.37 & -0.05 \\ -0.34 & 1.09 & 0.03 \\ -0.31 & 0.30 & 0.28 \end{bmatrix}$	$\begin{bmatrix} 1.87 & -0.44 & 0.08 \\ -0.41 & 0.67 & -0.06 \\ -0.27 & -0.04 & 0.24 \end{bmatrix}$	$\begin{bmatrix} 1.43 & -0.48 & 0.11 \\ -0.50 & 1.05 & -0.10 \\ -0.42 & -0.38 & 0.08 \end{bmatrix}$	$\begin{bmatrix} 0.51 & -0.22 & -0.06 \\ -0.34 & 0.62 & 0.02 \\ -0.02 & -0.10 & 0.06 \end{bmatrix}$

Figure 2.11: Candidate robot poses used in compliance analysis. The actuation rod length configurations necessary to achieve the pose and resultant compliance matrix for that pose are shown.

2.5 Robot Compliance and Payload Capacity

The strength performance of the robotic prototype was assessed using end-effector compliance matrices that were experimentally calculated while the robot was actuated in straight, tip-translated, and bending poses. The compliance matrix relates the applied force at the end-effector $\mathbf{F}$ and its resultant displacement Δ $\mathbf{p}$ in the global reference as follows:

$$\begin{gathered} \mathbf{\Delta p} = C\mathbf{F} \\ \begin{bmatrix} \Delta p_x \\ \Delta p_y \\ \Delta p_z \end{bmatrix} = \begin{bmatrix} C_{11} & C_{12} & C_{13} \\ C_{21} & C_{22} & C_{23} \\ C_{31} & C_{32} & C_{33} \end{bmatrix} \begin{bmatrix} F_x \\ F_y \\ F_z \end{bmatrix} \end{gathered} \tag{2.2}$$

To calculate the compliance matrix for each pose, end-effector tip loads are applied in the x, y, and z directions relative to the base frame of the robot O_R as shown in Figure 2.10 and measure the change in tip position using a stereoscopic camera. Markers are attached to the distal end and base of the robot to measure the deflections at the end-effector (in the base frame of the robot O_R). For each loading case, a pre-load of 200g is applied to mitigate the backlash that can occur in the actuation setup and then marker positions and orientations are recorded after loading. An additional 200g is applied at the tip (total of 400g tip load) and the resultant marker positions are recorded after this loading. The displacements from when the robot is loaded with 200g to when it's loaded with 400g are used for Δp_x, Δp_y and Δp_z. This process is performed for the five pose cases as shown in Figure 2.11, containing the results of the experimentally determined compliance matrices for each of the poses. The robot exhibits low compliance at the tip for all configurations. From both inspection of the robot loading scenario and the compliance matrix results, the traditional s-shape mode of deformation found in near-straight poses is virtually eliminated; significant torsional deformation in the bending cases with out-of-plane loads has also been mitigated.

Inspired by the results of the compliance experiments, the robot's load capacity was demonstrated by pouring a glass of water into another cup. Figure 2.12 shows the timestamps of the carrying task. In this demonstration, the robot is loaded at its end-effector with the payload. The cup assembly without any water added is 160g. 8oz of water is added (227g) to the cup assembly for a combined 387g tip load (stage 1). Then, the robot lifts the payload in the positive y-direction (stage 2) and then translates in the negative x-direction (stage 3). Finally, the end-effector smoothly rotates to pour the water into the coffee mug on the (stage 4). This task was accomplished by actuating a single motor at a time within 15 seconds. No oscillations were observed, and none of the water spilled from the cup assembly while in transit.

The results of the compliance characterization and carrying demonstrations show how a strong continuum robot can be developed out of common materials by leveraging the geometric design improvements for the backbone and actuation rod routing without introducing additional stiffening components or weight into the robot design.

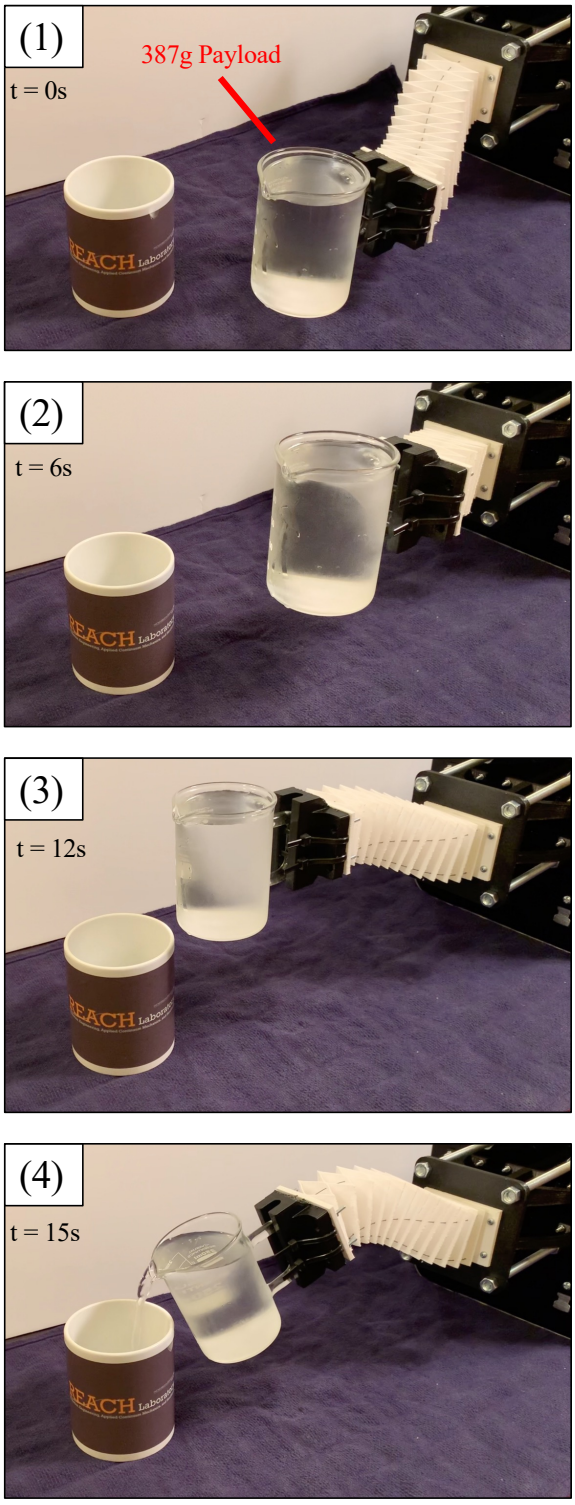


Figure 2.12: Payload carrying task with time-stamped steps.

Chapter 3

Concentric Precurved Bellows: Improving Stability in Concentric Tube Robots

3.1 Disclosure of Previously Published Material

The work presented in this chapter has been published in IEEE Robotics and Automation Letters [54]. The dissertation author served as first author on this publication and D. C. Rucker, the chair of this dissertation's committee, was second author and provided guidance and support throughout the paper writing process.

3.2 Overview

Torsional flexibility and frictional hysteresis continue to be difficult aspects of concentric-tube actuation regardless of robot size. Torsional flexibility can introduce undesired complexities into the behavior of these robots, including non-constant curvature shapes and "snapping" behavior in which the robot can rapidly release stored elastic energy and transition to a different configuration [88, 74]. A

fundamental parameter that affects the stability of concentric precurved tubes is the ratio of effective flexural rigidity, EI, to effective torsional rigidity, GJ which will be referred to as the ratio EI/GJ throughout this chapter (where E is Young's modulus, I is the cross sectional second moment of area, G is the shear modulus, and J is the polar moment of area). Lowering this ratio can mitigate or eliminate undesired torsional effects.

Cutting a pattern of notches into the tubes (i.e. "patterning") can reduce the effective EI/GJ ratio, and a variety of notch patterns have been investigated [98, 7, 8, 9]. As shown in Table 3.1, while solid tubes have a ratio of around 1.3 (assuming Poisson's ratio $\nu = 0.3$), the various notch patterning strategies in the works cited in the table created tubes with EI/GJ ratios ranging from 0.344 to 0.95.

This chapter addresses two existing limitations of the concentric tube robots: (1) torsional compliance limitations, and (2) small diameter limitations by investigating a new concept for bending actuators for soft and continuum robots based on precurved concentric bellows. While bellows structures are often used as flexible pressure vessels for fluidic actuation strategies [52], the bellows are used as the tubes for CTRs. A range of bending angles in a single plane can be achieved by rotating the two bellows bases by the same angle in opposite directions, if the bellows have equal flexural rigidities. The plane of bending can be changed by rotating the bellows bases equal amounts in the same direction as shown in Figure 3.1. The geometry of typical convolution bellows designs exhibits high torsional rigidity relative to flexural rigidity which virtually eliminates the negative effects associated with torsion. As recorded in Tables 3.1 and 3.3, 3D printed prototype bellows tubes exhibited experimental EI/GJ values between 0.016 and 0.078, which is (1) an order of magnitude lower than typical EI/GJ values achieved so far through laser machined cutout patterns, and (2) low enough to effectively eliminate any torsional lag during actuation, such that torsionally rigid kinematic models become accurate. In addition, the bellows concept exhibits a large bending range of motion within reasonable material strain limits. This enables the fabrication of large diameter robots and allows for large precurvatures

Table 3.1: Flexural to Torsional Rigidity Ratios

Reference	**Design**	EI/GJ
–	Solid Tube	1.3 (if $\nu = 0.3$)
[98]	Horizontal Notches (120°)	0.4
[7]	Horizontal Notches	0.48
[8]	Horizontal Notches (120°)	0.344 to 0.587
[9]	Cellular Hole Pattern	0.94
This work	Bellows Tube	0.016 to 0.078

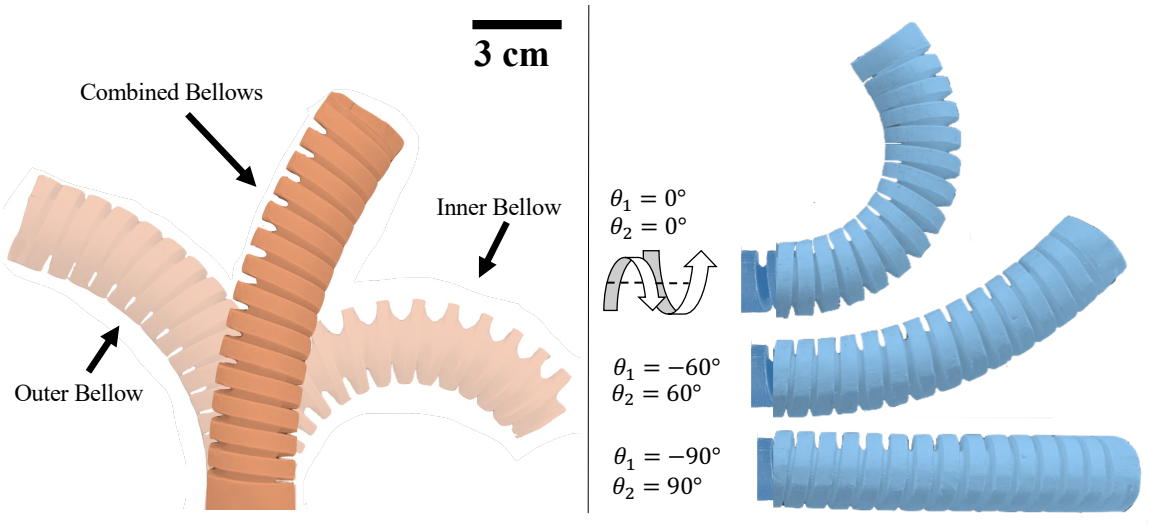


Figure 3.1: Improved strength and stability of concentric tube robots using bellows.The concentric bellows pair is actuated by axially rotating the base of each individual bellows. Rotating equal amounts in opposite directions changes the bending angle in a single plane, while rotating equal amounts in the same direction changes the plane of bending. Torsional rigidity is high relative to flexural rigidity due to the bellows geometry, such that a torsionally rigid modeling assumption is accurate.

relative to the bellows diameter. One identified trade-off is that bellows geometry is not as compact as thin-walled tubes since the bellows convolutions alternate between two different inner and outer diameters which can be challenging to scale to extremely small diameters. However, using bellows enables a new actuation method for large-scale soft robots that can serve as an alternative to tendon-driven or fluidic actuation.

This chapter covers the design and fabrication of 3D printed pairs of CTR bellows. Parameter identification is performed through FEA simulation and experimental tests on prototypes. The torsionally rigid concentric-tube kinematic model originally developed in [88] is expanded to handle the possibility of direction-dependent flexural rigidities. Finally, the torsionally rigid behavior during concentric-tube actuation is experimentally validated as well as the model shape accuracy for bending angles up to 120°.

3.3 Bellows Design and Fabrication

Low-cost methods for additive manufacturing of concentric bellows pairs through 3D printing (fused-deposition modeling) were developed for this work. These methods are suitable for research and the rapid iterative development of soft robot actuators. Typical bellows design consists of a convolution geometry, with examples shown in Figure 3.2, that is revolved around a central axis to form a "revolute bellows." In order to minimize overhangs and provide a stable interface with the print bed, a v-shaped inner geometry and a flat outer geometry, as shown in Figure 3.3, were used. The plate width (the difference between a bellows inner and outer radii) and the wall thickness are the dominant factors in influencing the flexural rigidity, while the overall diameter is relatively less significant (in contrast to solid tubes). This enables an inner/outer balanced stiffness pair of bellows [74] to be designed. In the example design as shown in Figure 3.3, the inner bellows is just slightly stiffer than the outer because it has a smaller plate width and the same wall thickness.

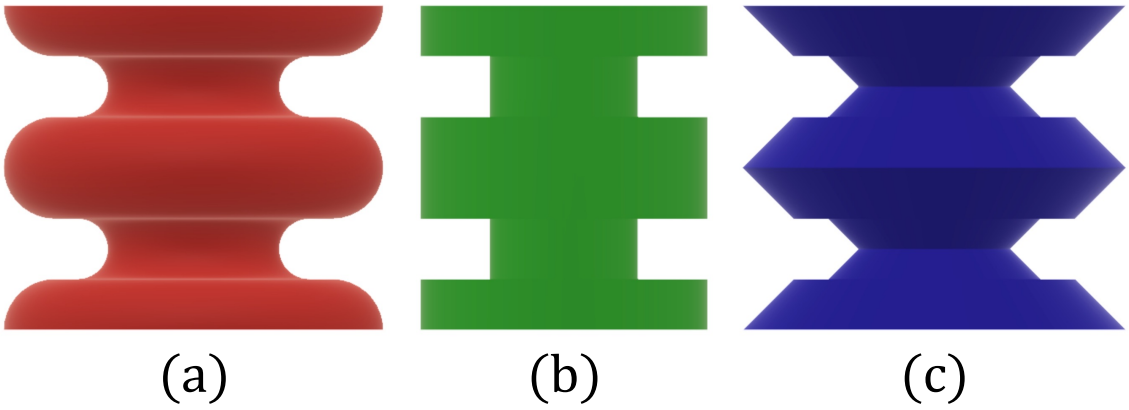


Figure 3.2: Possible convolution geometries using circular (a), flat (b) or v-shaped convolutions (c). Bellows can be designed to have elements from all three variations. Our 3D printed prototypes use flat outer convolutions and v-shaped inner convolutions to improve printing feasibility.

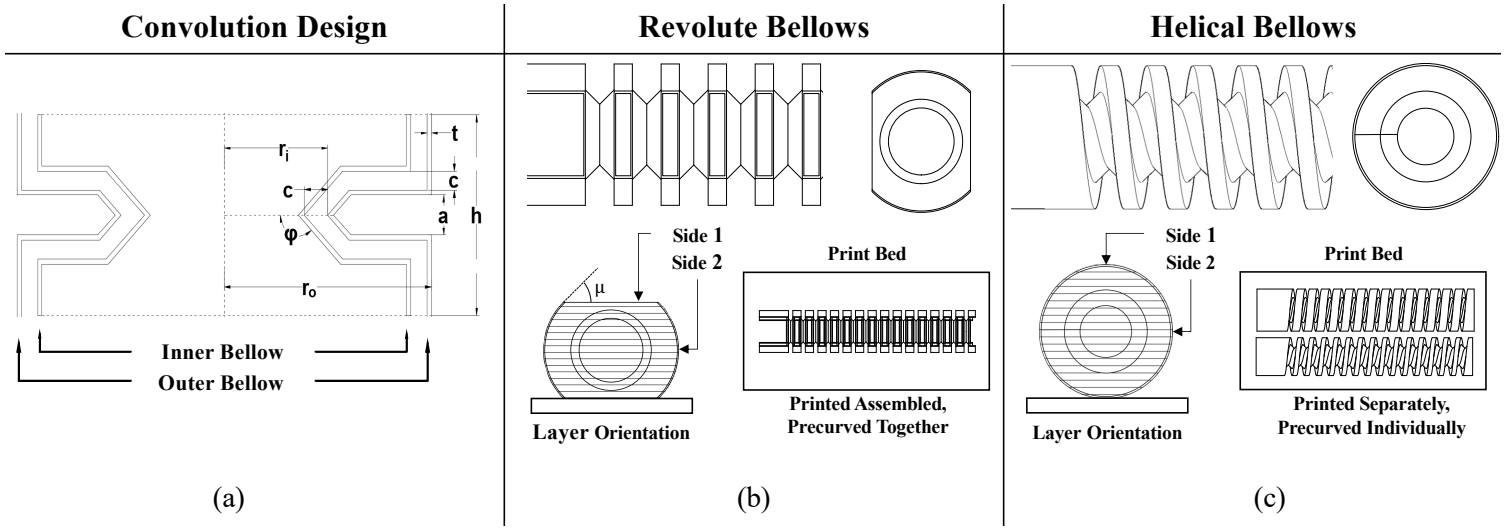


Figure 3.3: Convolution geometry schematic and design parameters (a) used for revolute (b) and helical bellows (c). 3D printing layer orientation along with side references used in parameter estimation and kinematic experiments are shown for both bellows. A revolute bellows pair cannot be disassembled and must be printed and precurved in the assembled state. Helical bellows can be printed and precurved separately and subsequently assembled

3.3.1 Revolute Bellows Design

Revolving an inner and outer convolution geometry about a central axis results in a concentric pair of revolute bellows that cannot be assembled or disassembled because they are interlocked. One way to construct such an assembly is to additively manufacture the two bellows tubes simultaneously in the assembled (interlocked) state, as shown in Figure 3.3 (b). While dissolvable support material can be used to support and separate the two bellows surfaces during printing, it is very challenging to subsequently dissolve the support material due to the winding convolution geometry and small clearance between the parts. To avoid this difficulty, an extruded cut, which makes an angle μ from the outer tangent, can be applied to either side of the assembled bellows CAD model as shown in Figure 3.3 (b). The geometry of each individual bellows can then be independently anchored to the build plate, and the pair can be printed in the assembled state without support material.

3.3.2 Helical Bellows Design

It is also possible to create a bellows tube geometry by specifying a helical extrusion of the convolution geometry (with pitch h) instead of a revolved extrusion. This allows easy assembly and disassembly of a bellows tube pair by simply threading them into or out of each other. Thus, individual helical bellows can be printed and precurved separately and subsequently assembled. Actuation of a helical bellows pair is then achieved by combined translation and rotation of each base with pitch h.

3.3.3 Pre-curving bellows via Heat Treatment

After either a revolute bellows pair or an individual helical bellows is printed, the bellows can be pre-curved by constraining it to a desired shape via a jig and heating it to the glass transition temperature of the material. After glass transition, the part is allowed to cool in its fixtured precurved state and is subsequently removed. It should be noted that it is also possible to eliminate the heat treatment step by simply

printing the concentric bellows pair in the pre-curved state, but this requires much more effort and complexity in the CAD modeling of the design, whereas an uncurved bellows design is very straightforward to generate.

3.3.4 Example Bellows Specifications and Fabrication

The dimensions of the bellows prototypes for both revolute and helical designs used in experiments are tabulated in Table 3.2. These dimensions were selected iteratively such that bellows could smoothly rotate within one another and feasibly be fabricated. Prototypes were 3D printed out of PLA on a Makerbot Replicator 2 at 230°C and a layer height of 0.15 mm. Single wall (shell) print settings with no infill and a floor/ceiling height of 0.4 mm were used to achieve a finished part with roughly uniform wall thickness. A curvature jig was inserted through the bellows inner lumen to enforce a desired precurvature on the bellows as shown in Figure 3.4 (b). To ensure jig shape is maintained through the heating process the jigs were 3D printed using a co-polyester material (ColorFabb HT) with a higher glass-transition temperature greater than the bellows material (PLA). The jig-constrained bellows were placed in an oven (Quincy Lab Model 10 Oven) at 60°C for 20 minutes. After heating, the bellows were ambiently cooled to room temperature (approx. 24°C) while leaving the curved jig within the bellows for at least 20 minutes. After removal of the jig, the inner and outer precurved bellows are each connected to a drive mechanism, shown in Figure 3.4 (c), which allows coupling to a manual actuation system which axially rotates and translates their bases.

3.4 Bellows Modeling

3.4.1 Bellows Parameter Characterization

In order to develop accurate kinematic models and predict concentric-tube manipulator performance, it is necessary to calibrate the effective flexural and torsional

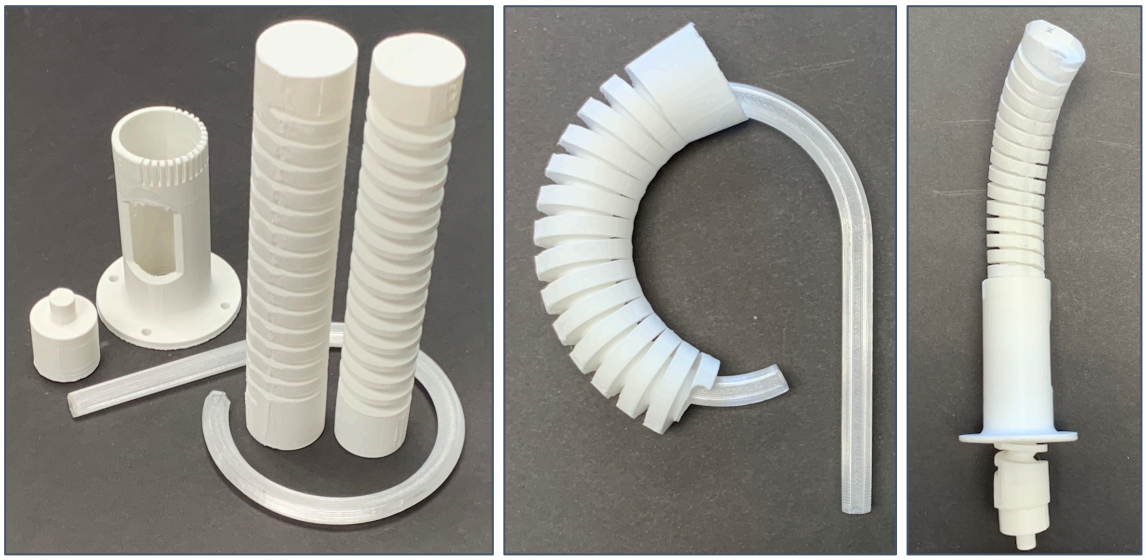


Figure 3.4: Components used to fabricate a pair of helical bellows (a). The curvature jig is inserted through the inner lumen of the bellows and enforces the new shape onto the bellows in the precurving process (b). Once precurved, inner and outer bellows attachments can be used to mount bellows onto actuation systems (c).

Table 3.2: Bellows dimensions of 3D printed prototype used in kinematic and bending experiments

Parameter	**Value**
Inner radius, r_i	7.5 mm
Outer radius, r_o	15 mm
Wall thickness, t	0.3 mm
Clearance, c	1.2 mm
Convolution pitch, h	9 mm
Convolution gap, a	2.5 mm
Inner convolution angle, φ	135°
Tangent angle at cut, μ	45°

rigidities of a bellows design. In this section, model parameters are calibrated for the prototype bellows by fitting the rigidity parameters to deflection data from small-deflection loading scenarios. Calibration data from (1) FEA simulations of the bellows, and (2) experimental tests on the physical prototypes are compared. These parameters are then used in a constant-curvature kinematic model.

The FEA simulations were produced using Abaqus/Standard (Simulia, Dassault Systems). Each bellows design was modeled using quadrilateral shell elements (element type S4R) with a thickness of 0.3 mm. Young's modulus for 3D printed PLA can vary between 1.8 to 3.3 GPa based on a variety of material factors and testing standards [118]. A Young's modulus of 3.15 GPa was used for all FEA simulations which is reported in the data sheet of a commonly used PLA (Ultimaker). Typical simulation run time was around 10 seconds. The experimental setup used a stereoscopic camera and markers attached to the bellows prototypes to measure tip deflections and rotations from bending and torsion experiments as show in Figure 3.5 (a).

To determine the effective flexural rigidity, a range of tip loads are applied at the distal bellows end and with the deflection measured at each load. The max tip load was 5 grams in order to remain in the small deflection range. The effective flexural rigidity EI is then fitted to the small deflection data using the Euler-Bernoulli tip deflection formula:

$$w = \frac{PL^3}{3EI} \tag{3.1}$$

where w is the tip deflection, P is the applied tip load, and L is the length of the beam. The deflection data and the linear fit are plotted in Figure 3.5 (b) and (c). In the FEA tests, tip masses of 1, 2, 3, and 4 grams were applied to the distal end while the experimental trials include an additional 5 gram load as well as the mass of the tip marker. These tests were performed with loads applied in the direction of Sides 1 and 2 for both the revolute and helical designs to account for the direction-dependent properties that are caused from 3D printing. After linearly fitting the

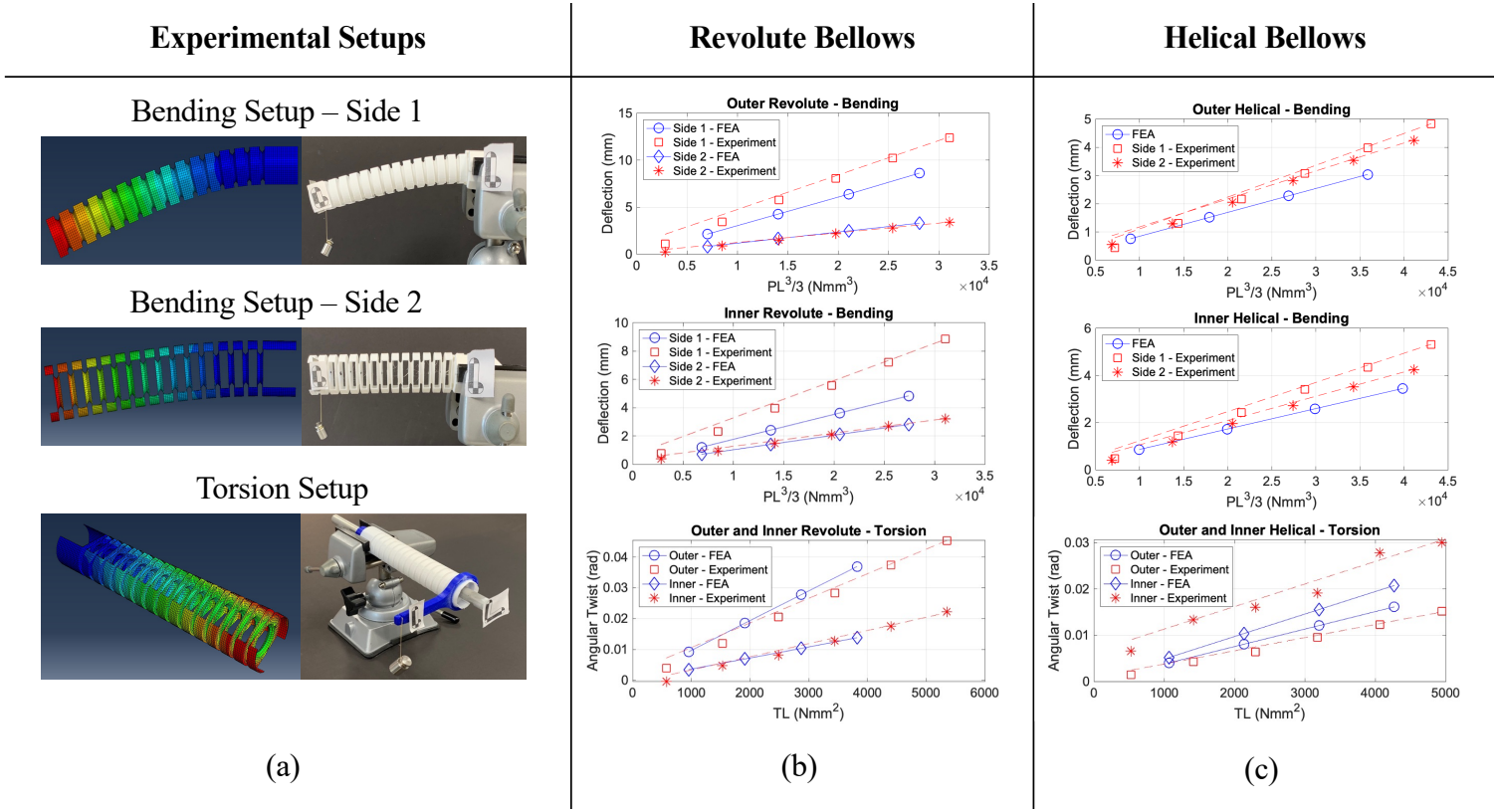


Figure 3.5: Flexural and torsional rigidity calibration of helical and revolute bellows designs. The experimental and FEA setups are shown in (a) with the flexural and torsional calibration results for the inner and outer bellows for the revolute (b) and helical (c) designs.

deflection data versus $PL^3/3$ (as outlined in ASTM D790-17, the standard test methods for determining flexural Properties of plastics), the slope of this fitted line then corresponds to $1/EI$, the inverse of the estimated flexural rigidity. The linear fit R-squared values for all flexural rigidity trials were at least 0.99 or greater.

The effective torsional rigidity GJ was estimated in a similar process by measuring the angular twist of the bellows ϕ from an applied torsional load T to a bellows of length L. The twist angle can be calculated as follows:

$$\phi = \frac{TL}{GJ} \tag{3.2}$$

The angular twist ϕ versus TL is plotted in Figure 3.5 (b) and (c) and a linear fit of the FEA and experimental angular twist data was performed. The slope of these fitted lines then correspond to $1/GJ$, the inverse of the effective torsional rigidity. Masses of 10, 20, 30, 40, and 50 grams were placed at the end of the arm which is 75 mm in length from the centerline of the bellows to the location of the loading mass. An aluminum tube was inserted through the center of each bellows prototype to mitigate any bending that could occur in the measurements. The FEA trials use a similar loading condition where moments of 0.0074, 0.0147, 0.0221, 0.0294 Nm were applied. The R-squared values for all torsional rigidity trials were greater than 0.97. The results of parameter characterization are compiled in Table 3.3. In general, FEA predicted slightly stiffer flexural rigidity values and slightly less stiff torsional rigidity values than those that were experimentally determined. Experimentally determined EI values for side 1 of each design were expected to be lower since 3D printed parts typically have a lower flexural rigidity in the direction of print orientation, due to layer effects [118]. Considering the uncertainties in 3D printed wall thickness, the range of uncertainty in Young's modulus, and the complexity of bellows geometry, FEA predicted reasonable bending and torsional rigidity values. It should be noted that even though there is some error in the FEA predicted parameters, this accuracy is

Table 3.3: FEA and experimental characterization of revolute and helical bellows prototypes.

			EI (Nm^2)		**GJ** (Nm^2)		**EI/GJ**	
Bellow Type		**Side**	**FEA**	**Experiment**	**FEA**	**Experiment**	**FEA**	**Experiment**
Revolute	Outer	*Side 1*	0.0032	0.0025	0.104	0.115	0.031	0.022
		Side 2	0.0085	0.0090			0.082	0.078
	Inner	*Side 1*	0.0057	0.0035	0.235	0.215	0.024	0.016
		Side 2	0.0097	0.0097			0.041	0.045
Helical	Outer	*Side 1*	0.0118	0.0081	0.300	0.322	0.039	0.025
		Side 2	0.0118	0.0093			0.039	0.029
	Inner	*Side 1*	0.0101	0.0074	0.168	0.172	0.060	0.043
		Side 2	0.0101	0.0089			0.060	0.052

sufficient for using FEA as an initial design tool, while more accurate experimentally calibrated parameters can be used for kinematic prediction and control.

The EI/GJ ratios from the physical experiments ranged from 0.016 to 0.078 which is an order of magnitude lower than previous methods for reducing this ratio based on laser cutting notches into metal tubes as listed in Table 3.1. Ratios this small can be considered effectively zero because they produce a concentric tube robot exhibiting virtually no torsional deformation or lag between the proximal and distal ends (i.e. actuator angles are transmitted down the length without loss, even to friction). Thus, kinematic models that assume infinite torsional rigidity can be reasonably used for CTRs using bellows.

3.4.2 Kinematic Modeling

A prior torsionally-rigid concentric-tube kinematic modeling framework [88] was modified to account for concentric structures that can exhibit direction-dependent flexural rigidity (such as 3D printed bellows as demonstrated in the previous section). Let $\mathbf{m}_i = [m_x \ m_y]^\top \in \mathbb{R}^2$ be the vector of the internal bending moment (about the x and y cross-sectional axes) carried by the i^{th} bellows expressed in a material reference frame attached to the i^{th} bellows. Let θ_i be the angle relating the material frame of the i^{th} bellows to a common robot "backbone" reference frame (defined as a "Bishop frame" that is fixed at the robot base and slides along the backbone without torsional rotation [119],[74]). Assuming zero torsional deformation along the length of the bellows, θ_i is constant and equal to the axial rotation of the i^{th} bellows at its base. Then, a moment balance on a segment of n concentric bellows expressed in the common backbone frame yields

$$\begin{aligned} \sum_{i=1}^{n} \mathbf{R}(\theta_i)\mathbf{m}_i = \mathbf{0}, \quad \text{where} \\ \mathbf{R}(\theta_i) = \begin{bmatrix} \cos(\theta_i) & -\sin(\theta_i) \\ \sin(\theta_i) & \cos(\theta_i) \end{bmatrix} \end{aligned} \tag{3.3}$$

A linearly elastic constitutive law relates the internal bending moment to the change in curvature of each bellows as

$$\begin{aligned}\mathbf{m}_i &= \begin{bmatrix} EI_{xx,i} & 0 \\ 0 & EI_{yy,i} \end{bmatrix} \left(\begin{bmatrix} u_{x,i} \\ u_{y,i} \end{bmatrix} - \begin{bmatrix} u^*_{x,i} \\ u^*_{y,i} \end{bmatrix} \right) \\ &= \mathbf{K}_i(\mathbf{u}_i - \mathbf{u}^*_i)\end{aligned} \tag{3.4}$$

where $\mathbf{K}_i$ is the bending stiffness matrix, $\mathbf{u}_i$ is the curvature vector containing the precurvature components about the bellows' own x and y cross-sectional axes, and $\mathbf{u}^*_\mathbf{i}$ is the initial precurvature vector of each bellows. Note that the flexural rigidities within $\mathbf{K}_i$ are allowed to be different in the x and y direction. The equilibrium curvature components in the robot backbone frame are then expressed as

$$\mathbf{u} = [u_x, u_y]^\top = \mathbf{R}(\theta_i)\mathbf{u}_i \quad \forall i \tag{3.5}$$

since the bellows must share a common curvature when expressed in the same reference frame. By substituting this into (3.4), the result can be manipulated to obtain the equilibrium curvature vector:

$$\mathbf{u} = \left(\sum_{i=1}^{n} \mathbf{R}(\theta_i)\mathbf{K}_i\mathbf{R}^\top(\theta_i) \right)^{-1} \sum_{i=1}^{n} \mathbf{R}(\theta_i)\mathbf{K}_i\mathbf{u}^*_i. \tag{3.6}$$

The constant-curvature transformation matrix $\mathbf{T}(s)$ of the robot backbone frame along the arc-length s of a segment of overlapped bellows tubes with respect to its

base is then computed as

$$\mathbf{T}(s) = e^{\hat{\xi}s} = \begin{bmatrix} \mathbf{R} & \mathbf{p} \\ \mathbf{0}^\top & 1 \end{bmatrix}, \text{ where } \hat{\xi} = \begin{bmatrix} 0 & 0 & u_y & 0 \\ 0 & 0 & -u_x & 0 \\ -u_y & u_x & 0 & 1 \\ 0 & 0 & 0 & 0 \end{bmatrix}$$
$$\mathbf{R}(s) = \begin{bmatrix} \frac{u_x^2+u_y^2C_\beta}{U^2} & \frac{u_xu_y(1-C_\beta)}{U^2} & \frac{u_yS_\beta}{U} \\ \frac{u_xu_y(1-C_\beta)}{U^2} & \frac{u_y^2+u_x^2C_\beta}{U^2} & \frac{-u_xS_\beta}{U} \\ \frac{-u_yS_\beta}{U} & \frac{u_xS_\beta}{U} & C_\beta \end{bmatrix} \tag{3.7}$$
$$\mathbf{p}(s) = \begin{bmatrix} \frac{u_y(1-C_\beta)}{U^2} & \frac{-u_x(1-C_\beta)}{U^2} & \frac{S_\beta}{U} \end{bmatrix}^\top$$

where $U = \sqrt{u_x^2 + u_y^2}$ (the magnitude of curvature), $\beta = sU$ (the total bending angle at s), and C_β and S_β are symbols that represent $\cos(\beta)$ and $\sin(\beta)$ respectively. Note that (3.7) is written in terms of the Cartesian components of the curvature vector. This is equivalent to the commonly used constant-curvature transformation reviewed in [120] (which is expressed in terms of the polar angle and magnitude of the curvature vector) but (3.7) has the advantage that it does not suffer from an artificial singularity in the straight configuration which is inherent to the polar representation.

If m segments exist in series, the transformation at the tip of the robot is then

$$\mathbf{T}_{tip}(s) = \prod_{j=1}^{m} \mathbf{T}_j(l_j) \tag{3.8}$$

where l_j is the arc-length of the j^{th} segment.

Note that in the case of a helical bellows pair, the overlapped section length changes as a function of actuation angles due to the helical pitch of the bellows, and there is an additional segment at the tip in which only one bellows is present (in which case (3.6) reduces to $\mathbf{u} = \mathbf{R}(\theta_i)\mathbf{u}_i^*$). In the case of a pair of helical bellows tubes, the length of this additional segment l_2 can be calculated as $l_2 = h|\theta_2 - \theta_1|$ where θ_2 and θ_1 are the outer and inner bellows base angles (defined such that $\theta_2 = \theta_1$ when the bellows are fully overlapped) and h is the helical pitch of the bellows design.

Depending on the handedness of the helix, and the direction of base rotation, the tip segment could consist of either the inner bellows or the outer bellows.

3.5 Validation Experiments

Validation experiments are conducted to confirm (1) the torsionally rigid assumption used in the kinematic model and (2) validate the kinematic model presented in subsection 3.3.2, as well as the accuracy of the parameters calibrated in subsection 3.3.1.

3.5.1 Validation of Torsional Rigidity Assumption

To validate the torsionally rigid model assumption (and the implication that friction does not affect the shape), the prototype is actuated over its entire workspace and the relative angle between the two bellows at the segment tip $\alpha_{tip} = \theta_{2,tip} - \theta_{1,tip}$ is measured and compared with the value of the relative angle of the two bellows bases $\alpha_{base} = \theta_{2,base} - \theta_{1,base}$. If the bellows pair exhibits torsional rigidity with no loss to friction, the tip angle should equal the base angle for all base rotations. The inner bellows rotates through 180° in both clockwise and counter clockwise directions in 10° increments. A graduated disk with a resolution of 1° was attached at the distal tip of the outer bellows, and a wire pointer attached to the inner bellows was used to indicate angle readings. Figure 3.6 (c) shows the experimental setup and results of this experiment. Figure 3.6 (a) shows the result for an unmodified, hollow tube CTR and Figure 3.6 (b) shows the result for a patterned tube. It should be noted that a direct comparison cannot be made between these results, as they come from CTRs that have different diameters, wall thicknesses, and precurvatures from the bellows prototype. However, this comparison shows how bellows can improve the effects of frictional hysteresis and torsional lag. The maximum difference between actuated and measured tip twist angle of the bellows pair was only 4°, which confirms the

assumptions of torsional rigidity and negligible frictional effects by exhibiting virtually zero torsional lag.

3.5.2 Validation of Kinematic Model

A manual actuation system was constructed that enables rotation and translation of two concentric bellows as shown in Figure 3.7. The setup uses two rotary stages which allow independent rotation of each bellows base with a micrometer for fine angular adjustments with a readable resolution of 0.083°. Because helical bellows require simultaneous rotation and translation with a specific pitch, a single dovetail linear stage was used to allow relative translation as the tubes are rotated.

To validate the accuracy of the full kinematic model of Section IV, the prototype bellows pair is actuated by equal angles in opposite directions (i.e. $\theta_1 = \alpha/2$, $\theta_2 = -\alpha/2$ for relative input angles ranging from $\alpha = 0°$ (precurvatures aligned) to $\alpha = 180°$ (precurvatures diametrically opposed) which actuates the bellows from maximum curvature, to almost completely straight as shown in Figure 3.8 (right). The radii of precurvature for both bellows tubes are 0.055 m in the direction of side 1.

A stereoscopic camera and a stylus pointer were used to measure points on the surface of the outer bellows as shown in Figure 3.8 (left). An adjustable desktop tripod with a camera mount attachment held the stylus pointer to provides reliable and steady measurements. The camera frame was rigidly registered to the robot base frame using a separate symmetric data set using MATLAB's 'pcregistericp()' from the Camera Vision Toolbox. The repeatability of the actuation and measurement procedure were evaluated by recording the distal tip position of the bellows coming from both $\alpha = 0°$ and from $\alpha = 180°$ configurations for the $\alpha = 40°, \alpha = 60°$ and $\alpha = 80°$ cases. 10 individual tip positions were taken at each configuration, with 5 from each direction. The largest standard deviation of tip position for each configuration was 0.7 mm.

The experimental surface shape data was then compared to predictions made by the torsionally-rigid kinematic model in Figure 3.9. Two different kinematic model predictions are shown: (1) the kinematic model using the flexural rigidities calibrated from FEA simulations, and (2) the kinematic model using the flexural rigidities calibrated experimentally (which are direction-dependent). The direction-dependent experimental calibration of flexural rigidity in subsection 3.3.1 improves shape prediction accuracy versus the FEA calibrated parameters. The shape validation results additionally verify the assumption of torsional rigidity and the implication that frictional forces, while present, do not significantly affect the shape because of the high stiffness of the torsional transmission.

The root mean square error (RMSE) for both models is tabulated in Table 3.4. These results demonstrate that concentric precurved bellows are feasible as continuum robot actuators. Whereas friction limits the kinematic accuracy and bending range of tendon/cable-driven continuum manipulators [121, 18], the concentric-bellows strategy is largely unaffected by frictional forces at large bending angles due to the high torsional stiffness of the transmission. Fluid-driven and material-based actuation may entail other trade-offs in terms of actuation bandwidth and safety (e.g. high pressures).

3.5.3 Payload Demonstration

To demonstrate payload capacity (and further confirm that friction does not hinder performance), Figure 3.10 shows a prototype lifting a 100g tip load, which is 4 times the mass of the bellows pair, while mostly retaining its desired shape across the bending range. Payload capacity can be tailored to the application by selecting the wall thickness and other dimensions of the convolution geometry. In general, increasing the wall thickness increases the effective EI while minimally affecting EI/GJ, thus increasing payload capacity while maintaining robot performance and

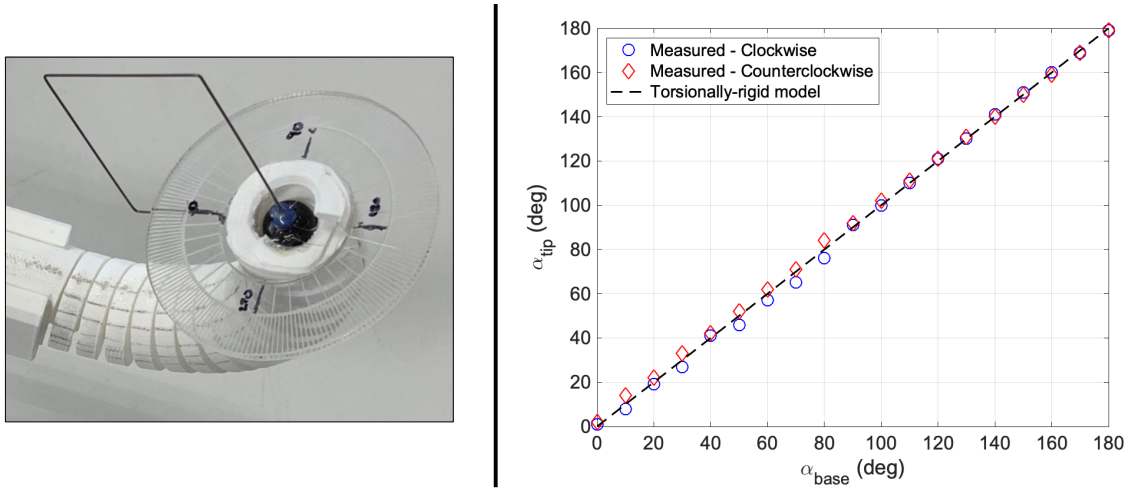


Figure 3.6: The plot shows the angle between the inner and outer bellows at the tip over a range of relative base actuation angles. The experimental setup is shown in on the left. Torsional rigidity would imply the base and tip angles to be equal (dashed line). Thus the data (right) confirms the torsionally rigid assumption of our model.

Table 3.4: Kinematic modeling error of concentric precurved bellows prototype

Configuration	with FEA Param. RMSE (mm)	with Experimental Param. RMSE (mm)
$\alpha = 0°$	1.28	1.28
$\alpha = 80°$	2.30	1.12
$\alpha = 120°$	3.89	1.99
$\alpha = 160°$	4.28	2.72
$\alpha = 180°$	4.27	2.78

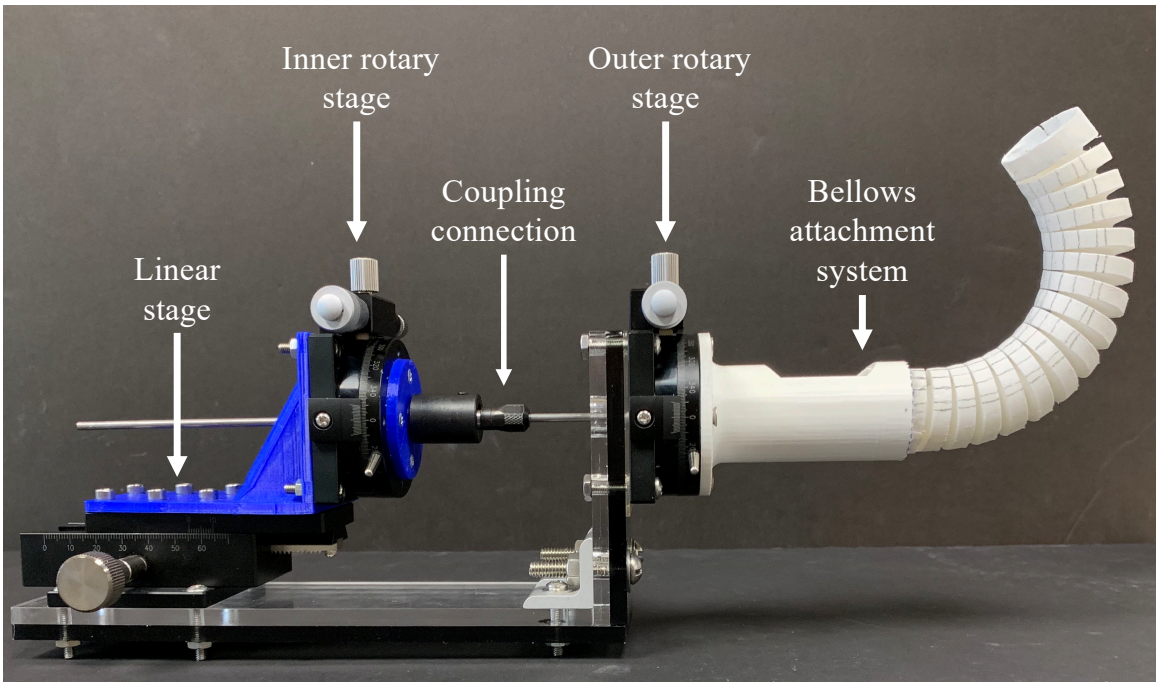


Figure 3.7: Manual actuation setup used in model validation experiments. The system provides rotation for both the inner and outer bellows and allows translation of inner bellows.

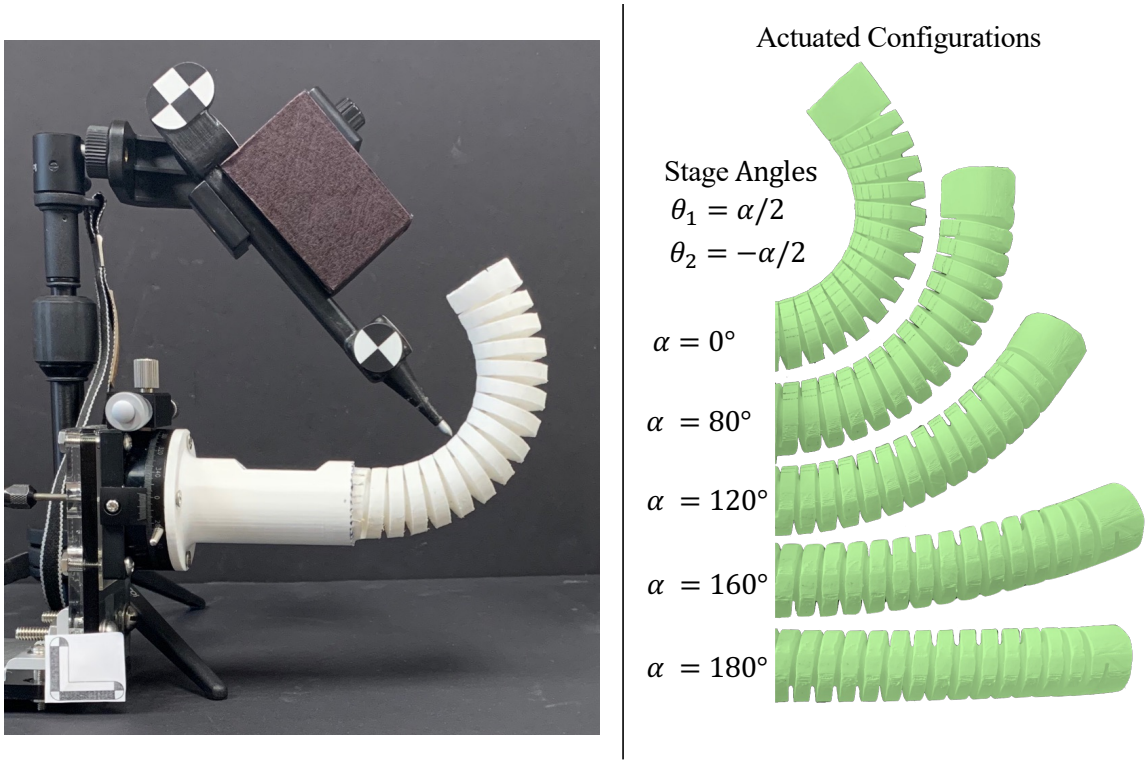


Figure 3.8: Experimental setup for measuring points along the curvature of thebellows pair (left). The outer curvature of the bellows pair were measured infive configurations in which the angles of the inner and outer bellows wereequal in magnitude but opposite in direction (right).

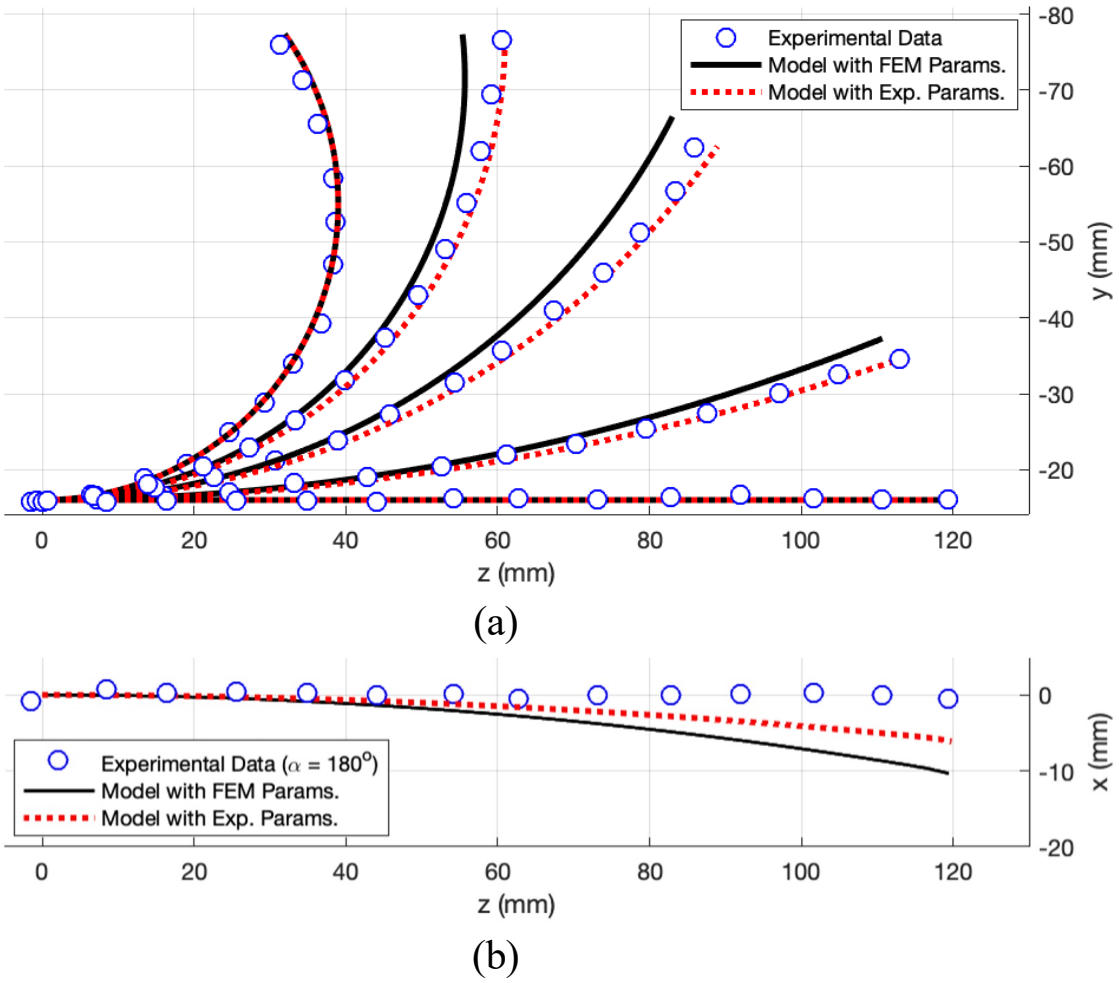


Figure 3.9: Experimental validation of torsionally-rigid kinematic model. The manual actuation setup is shown in (a) and the actuated configurations that are compared with the model are shown in (b). Experimental measurements of helical bellows at the actuated configurations are compared with the kinematic model using (i) FEA determined mechanical properties and (ii) experimentally determined mechanical properties.

overall diameter. For example, doubling the wall thickness of the outer helical bellows to 0.6 mm increases EI by a factor of 5 while only increasing EI/GJ by 25% to 0.05.

Applications of concentric-bellows actuation include manipulation tasks at scales appropriate for human cooperation. As a demonstration, a soft gripper was fabricated using revolute bellows as fingers that can grasp and lift a baseball (150g, 75mm diameter) as shown in Figure 3.10. It is also feasible to use concentric bellows actuation in surgical tools that require a high amount of angulation. For example, Figure 3.11 demonstrates a 5 mm diameter bellows precisely fabricated by nickel electroforming which is capable of at least a $\pm 135^\circ$ degree bending range in a short compact size. This new actuation strategy exhibits good performance over large bending angles due to an EI/GJ ratio much lower than what prior strategies have exhibited, eliminating the issue of unstable snapping and allowing the use of constant-curvature kinematic models.

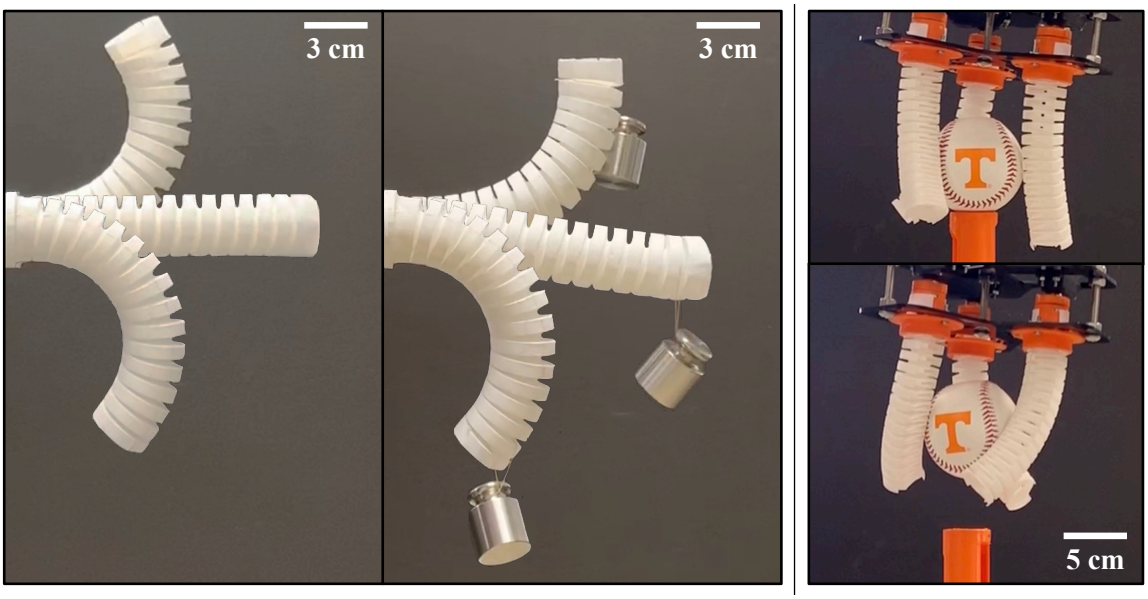


Figure 3.10: Payload capacity of prototype helical bellows pair with and without 100 g tip load (left) and a soft gripper demonstration (right).

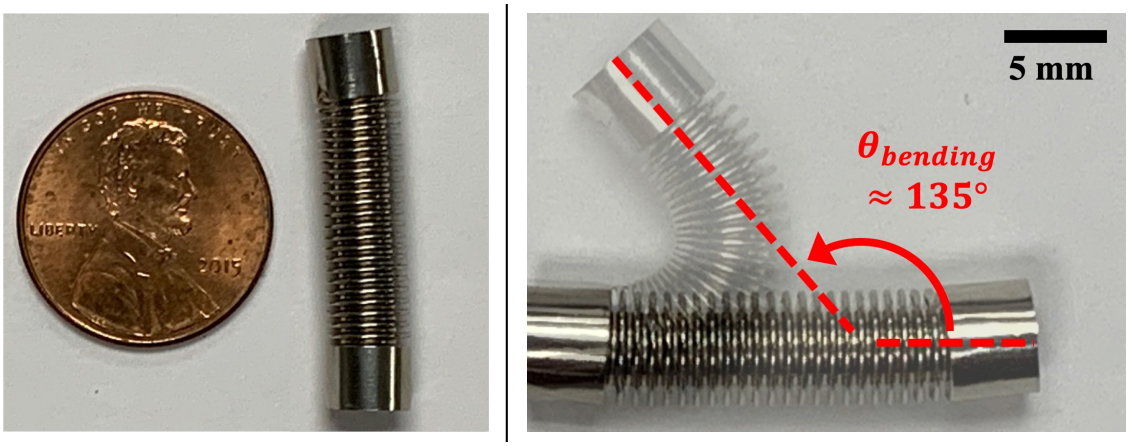


Figure 3.11: Bellows can fabricated at scale suitable for minimally-invasive surgical applications (left) and retain large bending angles at this scale (right).

Chapter 4

Model-Based Design of Concentric Push-Pull Robots for High Strength

4.1 Disclosure of Published Material

The work presented in this chapter is being submitted to IEEE Transactions in Robotics. The dissertation author will serve as the first author on this publication and D. C. Rucker, the chair of this dissertation's committee, will be second author and provided guidance and support throughout the paper writing process.

4.2 Overview

In this chapter, we derive our forward statics model for CPPRs and compare our model predictions with experimental results on several prototypes. Each tube is modeled as a classical Kirchhoff rod with an offset stiffness center and constraints of concentricity are derived and embedded in the model. A series of polynomial basis functions then approximates the curvatures of the common centerline and the

unconstrained degree of freedom of each tube. The coefficients of this polynomial series are then found via energy minimization (accounting for external loads) and used to construct the tube shapes and robot pose. Section 4.3 details the derivation of our energy-based kinematics model, beginning with the derivation of the kinematics of a single tube constrained to a centerline and ending with the implementation of the full kinematic model. Section 4.4 details an example design of a laser cut pattern that offsets the stiffness center of the tubes and demonstrates our parameter characterization process for estimating the mechanical properties of the tubes, which are inputs to the model. Section 4.5 covers our experimental validation of the model, in which we compare model kinematics and loaded deflection predictions with experimental prototypes. We investigate three pertinent CPPR design cases: (1) a two-tube, constant-curvature CPPR where the stiffness centers of each tube run parallel with the centerline, (2) a two-tube, 'converging' CPPR in which the stiffness centers taper toward the center of the tube down the length, and (3) a three-tube CPPR with parallel stiffness centers. Section 4.6 concludes with a discussion on our validation results and on potential future work.

4.3 Modeling

In this section, we derive our mechanics-based kinematic model for CPPRs. First we outline the overall model framework, mathematical conventions, and the assumptions used in the model. Then, we detail the modified Kirchhoff kinematic equations that can accommodate the kinematics of patterned tubes used for CPPRs. We show how the concentricity constraints between the tubes are embedded into the model, revealing the independent unconstrained variables that can be parameterized. We then detail an energy minimization procedure that accounts for external loading and actuation, and summarize the full model implementation.

4.3.1 Conventions and Modeling Assumptions

Each tube is kinematically modeled as a Kirchhoff rod in which the tube can only deform through bending and torsion. The Kirchhoff kinematic equations are a set of differential equations that describe how the tube position and orientation evolves down the length of the tube. We parameterize the curvature components of each tube, and these components are determined by applying the principal of minimal potential energy, which includes external loading.

For our model, the following assumptions are made:

1. Only conservative loads are applied. This includes point forces at the end effector and distributed forces along the length, expressed in the global frame.

2. The stiffness center offsets are continuous for each tube in the CPPR system.

3. We assume friction is negligible in our model. To mitigate the effects of friction, each tube is sanded after being laser machined.

4. Under the Kirchhoff tube assumption, axial and shear deformations are neglected.

5. Tubes are nested in perfect concentricity.

4.3.2 Kinematics of Tubes with Offset Stiffness Centers

We define the stiffness center of a tube as the location of the neutral axis in a cross section of the tube when the tube cross section carries a pure bending load. We attach a reference frame containing position $\mathbf{p}_i \in \mathbb{R}^3$ and orientation $\mathbf{R}_i \in \mathrm{SO}(3)$ along the stiffness center of each tube, where the z-axis of $\mathbf{R}_i$ is parallel to the tube center axis, and the x-axis passes through the tube center. Subscript i denotes the tube number, with tube 1 the outermost tube. The location of the tube center relative to the stiffness center is expressed in body-frame coordinates by a vector $\mathbf{r}_i \in \mathbb{R}^3$ in the

Table 4.1: Kinematic Nomenclature

$\dot{(\ )}$	Derivative with respect to s_1
$(')$	Derivative with respect to s
$\widehat{(\ )}$	Mapping that converts $\mathbb{R}^3$ to $\mathfrak{so}(3)$
$\vee$	Inverse of the $\widehat{(\ )}$ operation, $(\widehat{\boldsymbol{u}})^{\vee} = \boldsymbol{u}$
s	Arc length along common centerline
s_i	Arc length along stiffness center of the i^{th} tube
n	Number of tubes in CPPR
N	Highest polynomial order in parameterization
$\mathbf{p}_i$	Global position of stiffness center of the i^{th} tube
$\mathbf{R}_i$	Orientation of tube material cross-section of i^{th} tube
$\mathbf{r}_i$	Stiffness center in cross-section in body-frame
x_i	Local x-coordinate of stiffness center location
$\mathbf{u}_i$	Angular rate of change of $\boldsymbol{R}_i$ with respect to s_i
$\mathbf{p}$	Centerline position in global coordinates
$\mathbf{R}$	Orientation of Bishop frame attached to centerline
$\mathbf{t}$	Tangent vector of centerline position $\boldsymbol{p}$
$\mathbf{u}$	Angular rate of change of $\boldsymbol{R}$
k	Index of polynomial for parameterized curvatures
a_k	Coefficients for x-component of parameterized $\boldsymbol{u}$
b_k	Coefficients for y-component of parameterized $\boldsymbol{u}$
$c_{(k,i)}$	Coefficients of i^{th} tube parameterized curvature
$\mathbf{a}$	Vector of polynomial coefficients of a_k
$\mathbf{b}$	Vector of polynomial coefficients of b_k
$\mathbf{c_i}$	Vector of polynomial coefficients of $c_{(k,i)}$
$\mathbf{x}$	Coefficients vector of parameterized curvatures
L	Length of outermost tube (tube 1)
q_i	Actuated linear displacement of i^{th} tube
$\mathbf{y}$	Vector of state variables
E_e	Elastic energy of Kirchhoff tube
E_F	Energy from applied distal tip force
$\mathbf{F}$	Distal tip load in global coordinates
E_f	Energy from distributed force
$\mathbf{f}$	Distributed force applied to tube 1
E	Total potential energy of CPPR
α_i	Initial angular offset of i^{th} tube at base in CPPR
β_i	Distal angular offset of i^{th} tube at tip in CPPR
$\mathbf{g}$	Nonlinear constraint function
$(EI)_{x,i}$	Flexural rigidity of i^{th} tube about tube x-axis
$(EI)_{y,i}$	Flexural rigidity of i^{th} tube about tube y-axis
$(GJ)_i$	Torsional rigidity of i^{th} tube
$\mathbf{K}_i$	Stiffness matrix of i^{th} tube

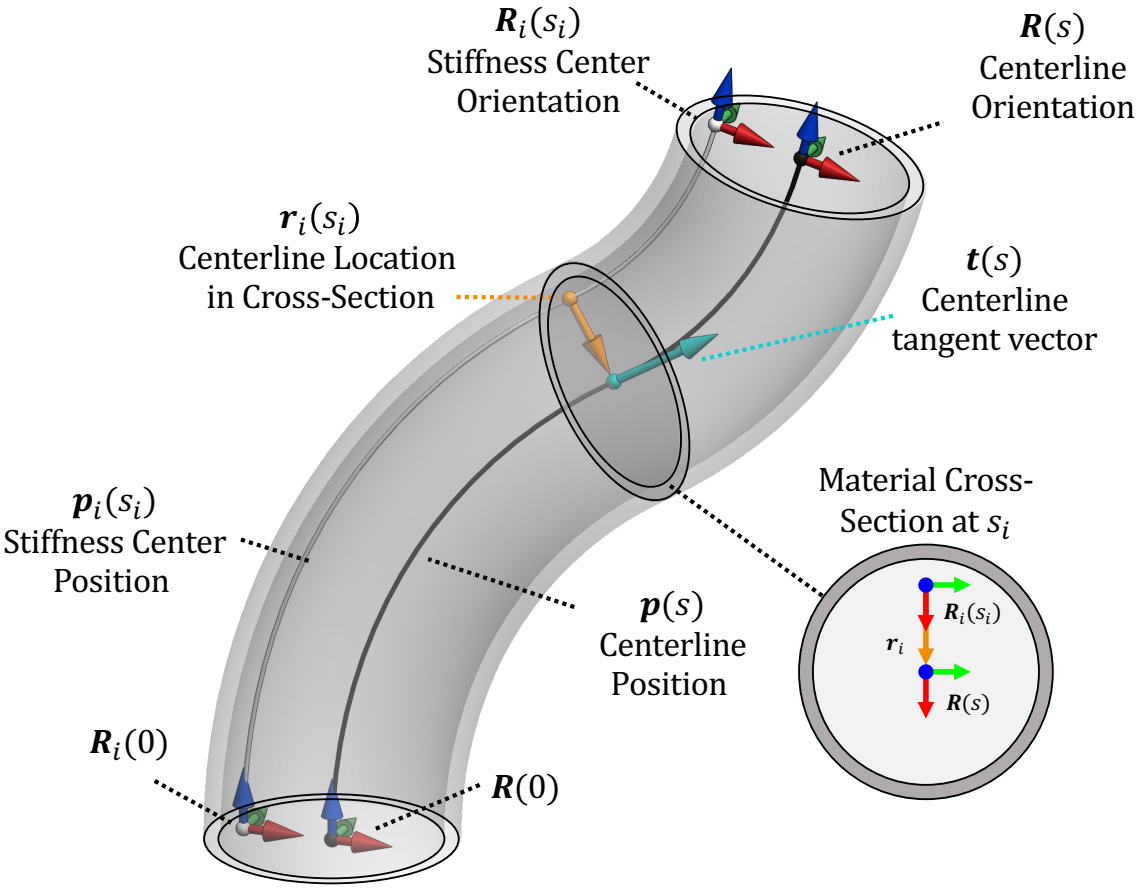


Figure 4.1: Illustration of a single tube with offset stiffness center with pertinent kinematic parameters labeled.

cross section of the tube. Figure 4.1 illustrates these definitions and relationships. The stiffness center location can vary down the length of the tube, as shown in Figure 4.2, where we can see examples of constant and varying $\mathbf{r}_i$.

The differential equations defining the evolution of the tube stiffness center frame (a function of the arc length along the undeformed tube s_i) are

$$\begin{aligned} \frac{d\mathbf{p}_i(s_i)}{ds_i} &= \mathbf{R}_i(s_i)\left(\mathbf{e}_3 - \frac{d\mathbf{r}_i}{ds_i}\right) \\ \frac{d\mathbf{R}_i(s_i)}{ds_i} &= \mathbf{R}_i(s_i)\widehat{\mathbf{u}}_i(s_i) \end{aligned} \tag{4.1}$$

where of $\mathbf{p}_i(s_i) \in \mathbb{R}^3$ is the global position of the stiffness center, $\mathbf{R}_i(s_i) \in \mathrm{SO}(3)$ is the orientation of the tube cross section, $\mathbf{e}_3 = [0\ 0\ 1]^\top$, $\mathbf{u}_i \in \mathbb{R}^3$ is the angular rate of change of $\mathbf{R}_i$ with respect to s_i, and the $\widehat{\ }$operator maps $\mathbb{R}^3$ to $\mathfrak{so}(3)$, the Lie Algebra of SO(3) [122] (also note that $()^\vee$ denotes the inverse mapping of $\widehat{\ }$, i.e., $(\widehat{\mathbf{u}})^\vee = \mathbf{u}$). In addition, $\mathbf{r}_i(s_i) \in \mathbb{R}^3$ defines the tube's center with respect to the frame attached at the stiffness center at s_i:

$$\begin{aligned} \mathbf{r}_i &= [x_i(s_i)\ \ 0\ \ 0]^\top \\ \frac{d\mathbf{r}_i}{ds_i} &= \left[\frac{dx_i(s_i)}{ds_i}\ \ 0\ \ 0\right]^\top \end{aligned} \tag{4.2}$$

where x_i is the displacement from the i^{th} tube's stiffness center origin to the centerline origin in the local frame coordinates. In this model, x_i can vary along s_i, the undeformed length of the tube. Note that defining $\mathbf{r}_i$ with zero y component does not limit the generality of this model, because $\mathbf{r}_i$ is expressed in coordinates of $\mathbf{R}_i$. Stiffness centers that form helical paths, or even more general paths can be described simply by attaching the stiffness center reference frame such that its x axis passes through the tube center.

4.3.3 Model Structure Overview

Our goal in the following subsections is to determine the kinematic constraints imposed by the enforcement of concentricity on multiple tubes with offset stiffness centers. While tubular concentricity constraints are well-understood for precurved concentric-tube robots (e.g. as detailed in[70],[71]), the concentricity constraints become more complex when the tubes have stiffness centers that are not located at the common tube center. Our high-level modeling approach will be to parameterize a framed curve along the common tube centerline (i.e. with a set of basis functions that determines centerline curvature), and then use the constraints of concentricity to determine certain components of curvature for the individual tubes. If there are remaining components of the individual tube curvatures that are not fully determined by the concentric constraints, we will additionally parameterize them with a set of basis functions. Thus, we aim to arrive at a set of free parameters (basis-function coefficients) that fully determines the multi-tube configuration with the constraints of concentricity embedded. After determining the free variables to be parameterized and embedding the constraints, we will use the principle of minimum potential energy to determine the basis function coefficients, thus predicting the mechanical response of the collection of tubes to actuation and external loading, which come into the energy minimization framework as global constraints and work-energy terms respectively.

4.3.4 Embedding the Constraints of Concentricity

When two or more tubes are concentrically nested within one another and fixed at their distal ends, the tubes will share a common centerline position in global coordinates $\mathbf{p}(s) \in \mathbb{R}^3$, parameterized as a function of arc length s along the curve. For modeling convenience we attach a reference orientation $\mathbf{R} \in \mathrm{SO}(3)$ along this centerline curve. The centerline frame is fixed at the robot base and slides along the centerline without torsion, forming what is known as a "Bishop Frame" [119],[74].

The equations governing the centerline Bishop frame are then:

$$\begin{aligned} \mathbf{p}'(s) &= \mathbf{t}(s) = \mathbf{R}(s)\mathbf{e}_3 \\ \mathbf{R}'(s) &= \mathbf{R}(s)\widehat{\mathbf{u}}(s) \end{aligned} \tag{4.3}$$

where s is the arc length along the centerline curve, $\mathbf{t}(s)$ denotes the tangent vector of the centerline, and $(')$ denotes a derivative with respect to s. It should be noted that $\mathbf{u} = [u_x \; u_y \; 0]^\top$ since the frame is a Bishop frame and has no torsion by definition. The centerline curvature functions $u_x(s)$ and $u_y(s)$ will eventually be parameterized by a set of basis function coefficients. We next seek to constrain the individual tubes to follow this common reference centerline. In the tube material cross section located at s_i, the position of the stiffness center $\mathbf{p}_i$ and the centerline position $\mathbf{p}$ are related by

$$\mathbf{p} = \mathbf{p}_i(s_i) + \mathbf{R}_i(s_i)\mathbf{r}_i(s_i) \tag{4.4}$$

To determine how this concentric constraint determines the individual tube curvatures, we first take the derivative of (4.4) with respect to s_i (i.e. perform index reduction):

$$\begin{aligned} \frac{d\mathbf{p}}{ds_i} &= \mathbf{R}_i \left(\mathbf{e}_3 - \frac{d\mathbf{r}_i}{ds_i} \right) + \mathbf{R}_i \widehat{\mathbf{u}}_i \mathbf{r}_i + \mathbf{R}_i \frac{d\mathbf{r}_i}{ds_i} \\ &= \mathbf{R}_i \left(\mathbf{e}_3 + \widehat{\mathbf{u}}_i \mathbf{r}_i \right) \end{aligned} \tag{4.5}$$

The differential relationship between the centerline arc length s and the individual tube reference parameter s_i is by definition

$$\frac{ds}{ds_i} = \left\| \frac{d\mathbf{p}}{ds_i} \right\| \tag{4.6}$$

Because the rotation of a vector does not affect its magnitude, the norm of $\frac{d\mathbf{p}}{ds_i}$ is equivalent to

$$\frac{ds}{ds_i} = \| \mathbf{e}_3 + \widehat{\mathbf{u}}_i \mathbf{r}_i \| \tag{4.7}$$

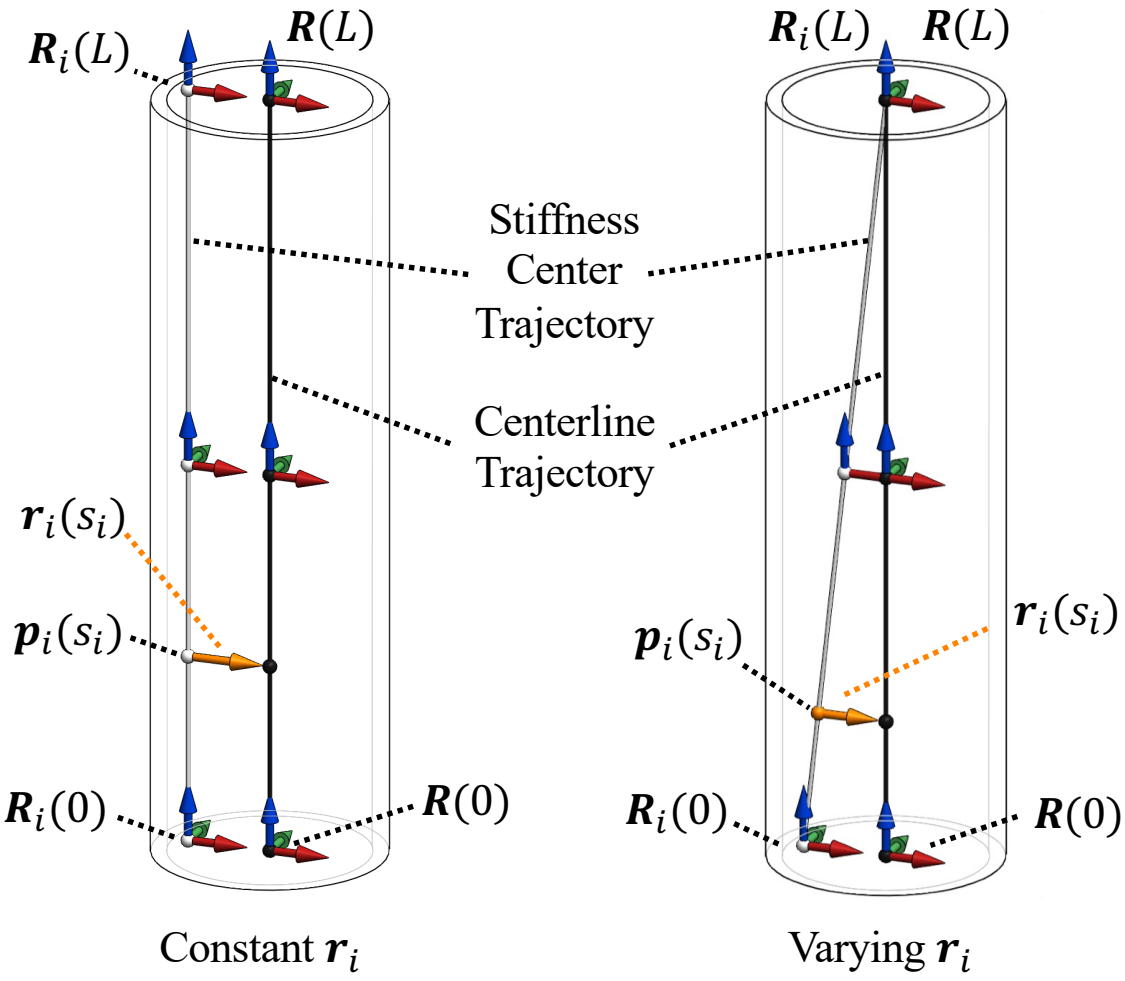


Figure 4.2: Examples of constant and varying stiffness center locations in relation to the tube profile.

Now knowing the differential relation in equation (4.7), we can use the definition of $\mathbf{t}$ in (4.3) to write the constraint as:

$$\begin{aligned}\mathbf{t} &= \frac{d\mathbf{p}}{ds_i}\frac{ds_i}{ds} = \mathbf{R}_i(\mathbf{e}_3 + \widehat{\mathbf{u}}_i\mathbf{r}_i)\frac{ds_i}{ds} \\ &= \mathbf{R}_i\frac{(\mathbf{e}_3 + \widehat{\mathbf{u}}_i\mathbf{r}_i)}{\|(\mathbf{e}_3 + \widehat{\mathbf{u}}_i\mathbf{r}_i)\|}\end{aligned} \tag{4.8}$$

Upon further inspection of the $\widehat{\mathbf{u}}_i\mathbf{r}_i$ term in equation (4.7) and (4.8), we find:

$$\widehat{\mathbf{u}}_i\mathbf{r}_i = \begin{bmatrix} 0 & -u_{z,i} & u_{y,i} \\ u_{z,i} & 0 & -u_{x,i} \\ -u_{y,i} & u_{x,i} & 0 \end{bmatrix}\begin{bmatrix} x_i \\ 0 \\ 0 \end{bmatrix} = \begin{bmatrix} 0 \\ u_{z,i}x_i \\ -u_{y,i}x_i \end{bmatrix}$$

where we see that $u_{x,i}$ does not affect the concentricity constraint equation at all. Therefore, we are free to parameterize the function $u_{x,i}(s_i)$ as a configuration variable along with the centerline curvature functions $u_x(s)$ and $u_y(s)$. The remaining curvature components $u_{y,i}(s_i)$ and $u_{z,i}(s_i)$ should then be determined by the concentricity constraint (4.4).

At first glance, it might seem that given $\mathbf{t}$ and $\mathbf{R}_i$, $u_{y,i}$ and $u_{z,i}$ could be straightforwardly determined from (4.8). However, taking the dot product of (4.8) with $\mathbf{R}_i\mathbf{r}_i$ we find:

$$\mathbf{t}^\top\mathbf{R}_i\mathbf{r}_i = \frac{(\mathbf{e}_3 + \widehat{\mathbf{u}}_i\mathbf{r}_i)}{\|\mathbf{e}_3 + \widehat{\mathbf{u}}_i\mathbf{r}_i\|}^\top\mathbf{r}_i = 0 \tag{4.9}$$

Interpreted geometrically, this result says that the x axis of $\mathbf{R}_i$ is orthogonal to the centerline tangent $\mathbf{t}$. This result presents a difficulty because neither $u_{y,i}$ nor $u_{z,i}$ appear in this component of the constraint. Considering this, combined with the fact that (4.8) is normalized, we find that (4.8) by itself cannot be used to directly determine both $u_{y,i}$ and $u_{z,i}$. Further, (4.9) reveals a constraint on $\mathbf{R}_i$ itself which must be true for all s_i. Both these challenges are resolved by performing an additional index reduction by taking a derivative. This provides the additional information needed to

solve for both $u_{y,i}$ and $u_{z,i}$, while also satisfying (4.9) (i.e. it's derivative will be satisfied everywhere, and $\mathbf{R}_i$ can be chosen to satisfy (4.9) at $s_i = 0$ as a boundary condition). Thus, differentiating (4.9) with respect to s_i,

$$\frac{ds}{ds_i}(\mathbf{t}')^\top \mathbf{R}_i \mathbf{r}_i + \mathbf{t}^\top \mathbf{R}_i \widehat{\mathbf{u}}_i \mathbf{r}_i + \mathbf{t}^\top \mathbf{R}_i \frac{d\mathbf{r}_i}{ds_i} = 0 \tag{4.10}$$

where $\mathbf{t}' = \mathbf{R}\hat{\mathbf{u}}\mathbf{e}_3$. Furthermore, we can use the original constraint equation (4.8) and the fact that $\mathbf{t}$ is a unit vector to write

$$\begin{aligned} \mathbf{t}^\top \mathbf{t} &= 1 \\ \mathbf{t}^\top \mathbf{R}_i \left(\mathbf{e}_3 + \widehat{\mathbf{u}}_i \mathbf{r}_i\right) &= \frac{ds}{ds_i} \\ \mathbf{t}^\top \mathbf{R}_i \mathbf{e}_3 + \mathbf{t}^\top \mathbf{R}_i \widehat{\mathbf{u}}_i \mathbf{r}_i &= \frac{ds}{ds_i} \end{aligned} \tag{4.11}$$

Substituting (4.10) into (4.11), we can then eliminate $\mathbf{u}_i$ from equation (4.11):

$$\mathbf{t}^\top \mathbf{R}_i \mathbf{e}_3 - \frac{ds}{ds_i}(\mathbf{R}\hat{\mathbf{u}}\mathbf{e}_3)^\top \mathbf{R}_i \mathbf{r}_i - \mathbf{t}^\top \mathbf{R}_i \frac{d\mathbf{r}_i}{ds_i} = \frac{ds}{ds_i}$$

which enables us to express $\frac{ds}{ds_i}$ in terms of the stiffness center and centerline kinematic variables:

$$\frac{ds}{ds_i} = \frac{\mathbf{t}^\top \mathbf{R}_i \left(\mathbf{e}_3 - \frac{d\mathbf{r}_i}{ds_i}\right)}{1 - \mathbf{e}_3^\top \hat{\mathbf{u}} \mathbf{R}^\top \mathbf{R}_i \mathbf{r}_i} \tag{4.12}$$

Substituting this result into (4.8), we find that we can now determine the remaining curvature components $u_{y,i}$ and $u_{z,i}$ of the stiffness center in terms of the centerline curvature $\mathbf{u}$, the known stiffness center $\mathbf{r}_i$ and other integrated quantities such as $\mathbf{R}$, $\mathbf{R}_i$, and $\mathbf{t}$.

$$\begin{aligned} u_{i,y} &= \frac{1}{x_i}\left(1 - \frac{\mathbf{e}_3^\top \mathbf{R}_i^\top \mathbf{t}\mathbf{t}^\top \mathbf{R}_i \left(\mathbf{e}_3 - \frac{d\mathbf{r}_i}{ds_i}\right)}{1 - \mathbf{e}_3^\top \hat{\mathbf{u}} \mathbf{R}^\top \mathbf{R}_i \mathbf{r}_i}\right) \\ u_{i,z} &= \frac{\mathbf{e}_2^\top \mathbf{R}_i^\top \mathbf{t}\mathbf{t}^\top \mathbf{R}_i \left(\mathbf{e}_3 - \frac{d\mathbf{r}_i}{ds_i}\right)}{x_i \left(1 - \mathbf{e}_3^\top \hat{\mathbf{u}} \mathbf{R}^\top \mathbf{R}_i \mathbf{r}_i\right)} \end{aligned} \tag{4.13}$$

As discussed previously $u_{x,i}$ is not constrained by the concentricity relationship.

4.3.5 Parameterization of Free Variables

Now that we have determined the free variables and embedded the constraints of concentricity, we now outline our parameterization of these free variables and how they are implemented in our energy minimization framework. The parameterization provides an approximation of the two components of the centerline curvature $\mathbf{u}$ and the free curvature component $u_{x,i}$ of each tube frame. We parameterize these functions as polynomials of order N in the variable s_1. For the centerline curvature $\mathbf{u} = [u_x \; u_y \; 0]^\top$, we have

$$u_x = \sum_{k=0}^{N} a_k s_1^k \qquad u_y = \sum_{k=0}^{N} b_k s_1^k \tag{4.14}$$

where a_k and b_k are the polynomial coefficients for the parameterized u_x and u_y respectively. Similarly for $u_{x,i}$, we have

$$u_{x,i} = \sum_{k=0}^{N} c_{(k,i)} s_1^k \tag{4.15}$$

where $c_{(k,i)}$ are the polynomial coefficients for the i^{th} tube. Thus, starting with a set of polynomial coefficients for a_k and b_k for the centerline and $c_{(k,i)}$ for each tube, we can construct the entire robot configuration by integrating the stiffness center kinematic equations in (4.1) (using (4.13) to enforce the concentricity) and the centerline kinematic equations (4.3). A detailed solution procedure including boundary conditions is discussed in the following subsections.

4.3.6 Principal of Minimal Potential Energy

To determine the robot configuration, we employ the principle of minimum potential energy. The potential energy sources we take into account include the potential energy

from elastic bending and twisting of the tubes and the energy from conservative external loads. Specifically, these include (1) total elastic potential energy, (2) the work of distal tip forces, and (3) the work of distributed forces applied to the outer most tube. The elastic potential energy E_e from bending and torsion of the i^{th} tube is

$$\frac{dE_e}{ds_i} = \frac{1}{2}(\mathbf{u}_i^\top(s_i) - \mathbf{u}_i^{*\top})\mathbf{K}_i(s_i)(\mathbf{u}_i(s_i) - \mathbf{u}_i^*) \tag{4.16}$$

where $\mathbf{u}_i^* = \left(\mathbf{R}_i^{*\top} d\mathbf{R}_i^*/ds_i\right)^\vee$ is the curvature associated with the stiffness center frame when the tube is straight (and $\mathbf{R}_i^*$ is the orientation when the tube is straight), and $\mathbf{K}_i$ is the stiffness matrix that contains the flexural rigidity values $(EI)_{x,i}(s_i)$ and $(EI)_{y,i}(s_i)$ about the x and y axes and the torsional rigidity $(GJ)_i(s_i)$ of each tube:

$$\mathbf{K}_i(s_i) = \begin{bmatrix} (EI)_{x,i}(s_i) & 0 & 0 \\ 0 & (EI)_{y,i}(s_i) & 0 \\ 0 & 0 & (GJ)_i(s_i) \end{bmatrix} \tag{4.17}$$

In Section 4.5, we will outline our process of estimating the components of (4.17) for laser cut tubes.

The elastic energy derivative in (4.16) for each tube is written in with respect to its respective arc parameter s_i. For convenience of implementation, we wish to integrate all differential equations with respect to a common integration variable, which we choose as s_1 (where tube 1 is the outermost tube). To facilitate this, we express each tube's energy derivative with respect to s_1 by multiplying (4.16) by

$$\frac{ds_i}{ds_1} = \frac{ds_i}{ds}\frac{ds}{ds_1} \tag{4.18}$$

where Equation 4.12 defines both $\frac{ds}{ds_1}$ and $\frac{ds_i}{ds}$. Thus, we write the derivative of total elastic energy with respect to s_1 as

$$\dot{E}_e = \sum_{i=1}^{n} \frac{dE_e(s_i)}{ds_i}\frac{ds_i}{ds_1} \tag{4.19}$$

Next we consider the work done by conservative external forces at the distal tip and along the length of the tubes. For both types of loading, we assume they are applied to the outermost tube in the collection (i.e. tube 1). The energy associated with the distributed loading can be written as

$$\dot{E}_f = -\mathbf{f}^\top(s_1)\mathbf{p}_1(s_1) \tag{4.20}$$

where $\mathbf{f}(s_1) \in \mathbb{R}^3$ is the force per unit s_1. Similarly, the energy associated with the work done by an external force $\mathbf{F} \in \mathbb{R}^3$ applied to the distal end of tube 1 can be written as:

$$E_F = -\mathbf{F}^\top \mathbf{p}_1(L) \tag{4.21}$$

where $\mathbf{F} = [F_x \ F_y \ F_z]^\top$ is expressed in global coordinates. Thus, the total potential energy E of the CPPR system is

$$E = E_F + \int_0^L \left(\dot{E}_e + \dot{E}_f\right) ds_1 \tag{4.22}$$

and (4.22) will serve as the objective function in the minimization problem that defines the robot kinetostatic model.

4.3.7 Model Boundary Conditions

Model boundary and initial conditions are used to express the physical constraints of CPPRs imposed by actuator displacements and tube tip the attachments.

Proximal Boundary Conditions

As shown in Figure 4.3, the variable s_1 is taken to be zero at the proximal end of the laser cut potion of tube 1, and L is the length from $s_1 = 0$ to the tip where all tubes are attached. When all tubes are straight and attached at their tips, s_i is also defined as zero when s_1 is zero, even though tube i may contain additional laser cut

length in the proximal direction. The displacement of the base of tube i away from this reference state is denoted q_i.

The initial arc lengths along the stiffness center of the i^{th} tube and the centerline are then

$$\begin{aligned} s_i(0) &= q_i - q_1, \quad i = 2, ..., n \\ s(0) &= -q_1 \end{aligned} \tag{4.23}$$

considering both s_i and s to be functions of s_1. The arc length along the centerline s is attached at the base of the slotted section of tube 1. As shown in Figure 4.3, a positive actuation displacement q_i is in the global -z-direction.

The initial position and orientation of each tube at its proximal base are implemented into the model as initial conditions to the kinematic equations for (4.1) and (4.3) as

$$\begin{aligned} \mathbf{p}_i(s_i(0)) &= -\mathbf{R}_z(\alpha_i)\mathbf{r}_i(s_i(0)) - [0\ 0\ q_1]^\top \\ \mathbf{R}_i(s_i(0)) &= \mathbf{R}_z(\alpha_i)^\top \mathbf{I}_{3\times 3} \end{aligned} \tag{4.24}$$

for $i = 1, ..., n$ where $\mathbf{I}_{3\times 3}$ is a 3×3 identity matrix and $\mathbf{R}_z(\alpha_i) \in \mathrm{SO}(3)$ is a rotation matrix about the z-axis by an angle θ

$$\mathbf{R}_z(\alpha_i) = \begin{bmatrix} \cos(\alpha_i) & -\sin(\alpha_i) & 0 \\ \sin(\alpha_i) & \cos(\alpha_i) & 0 \\ 0 & 0 & 1 \end{bmatrix} \tag{4.25}$$

For the centerline, the initial position and orientation is aligned with the global reference frame:

$$\begin{aligned} \mathbf{p}(0) &= [0\ 0\ -q_1]^\top \\ \mathbf{R}(0) &= \mathbf{I}_{3\times 3} \end{aligned} \tag{4.26}$$

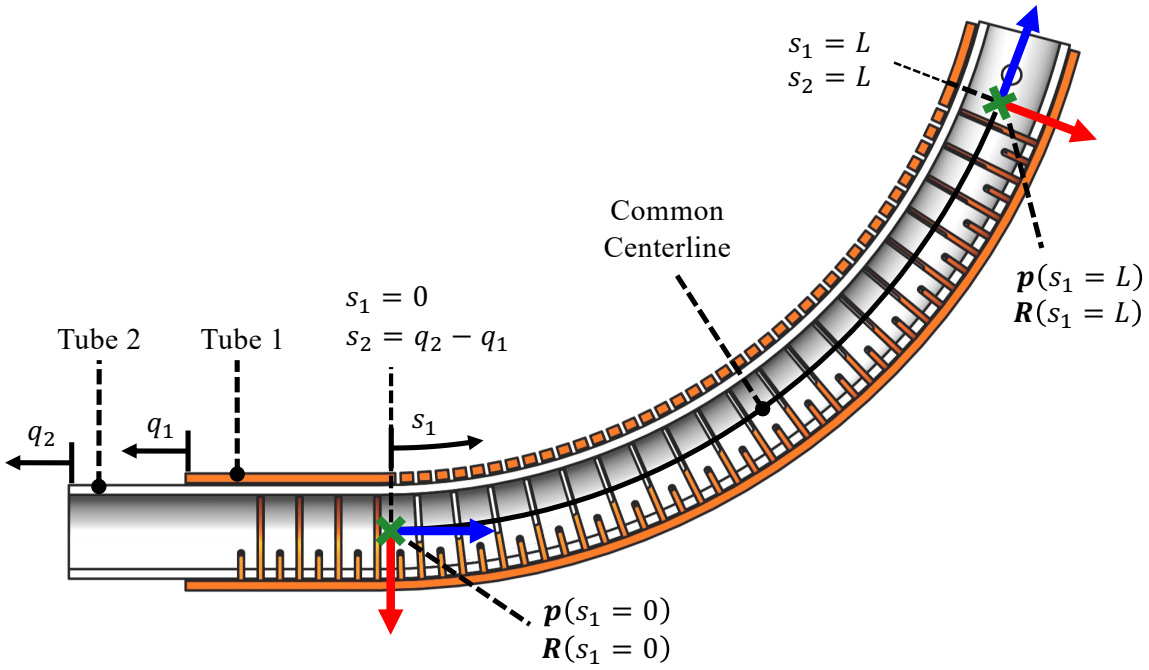


Figure 4.3: Actuation and arc length variables for a two tube CPPR. The base of the slotted section of Tube 1, the outermost tube, is considered $s_1 = 0$. The distal arc length $s_1 = L$ is set to where the slotted section of Tube 1 terminates.

Distal Orientation Boundary Constraint

Because the distal ends of the tubes are fixed together in CPPRs, this creates a distal orientation constraint for each tube. These distal constraints are implemented as boundary conditions on the kinematic equations as follows:

$$[\log(\mathbf{R}_z(\beta_i)^\top \mathbf{R}_i(L)]^\vee = 0, \quad i = 1, ..., n \tag{4.27}$$

where $\mathbf{R}_z(\beta_i)$ is the prescribed distal orientation offset for the i^{th} tube. In Section 4.3.8, we will show how (4.27) is implemented in our energy minimization.

Because the tips of all tubes are attached at the tip, and because of our definition of the s_i zero position, s_i must be to L at the tip $s_1 = L$, thus we have an additional distal constraint enforcing the fact that the tube tips never translate in and out of each other:

$$s_i(L) = L, \quad i = 2, ..., n \tag{4.28}$$

4.3.8 Summary of Solution Procedure

We now summarize the solution procedure to our kinetostatics problem using all of the previously derived model equations. First, the kinematic derivatives of the stiffness centers and the centerline need to be expressed with respect to s_1 to facilitate simultaneous integration of all variables. Expressing the centerline differential equations in (4.3) with respect to s_1 can be achieved by multiplying equation (4.12) to the set of equations:

$$\begin{aligned} \dot{\mathbf{p}} &= \frac{d\mathbf{p}}{ds}\frac{ds}{ds_1} = \mathbf{R}\mathbf{e}_3\frac{ds}{ds_1} \\ \dot{\mathbf{R}} &= \frac{d\mathbf{R}}{ds}\frac{ds}{ds_1} = \mathbf{R}\hat{\mathbf{u}}\frac{ds}{ds_1} \end{aligned} \tag{4.29}$$

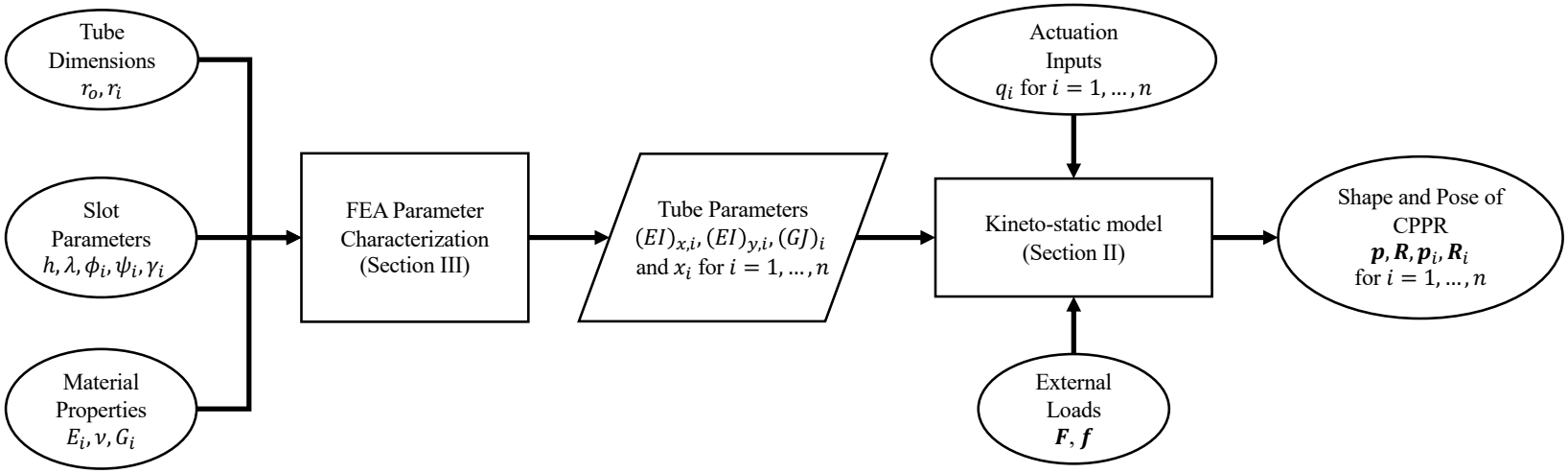


Figure 4.4: High-level flowchart the overall kinematics solutions. The dimensions, slot pattern, and material of the tubes are inputs to the FEA-based Parameter Characterization from Section 4.4 which outputs the bulk parameters of the slotted pattern. The tube parameters are used in the kineto-static model derived in Section 4.3. Actuation and external loads are inputs into the kineto-static model and the resultant shape and pose of the CPPR are the model outputs.

Expressing the kinematic differential equations of the stiffness centers with respect to s_1 is achieved by multiplying equation (4.18):

$$\begin{aligned}\dot{\mathbf{p}}_i &= \mathbf{R}_i(s_i)\left(\mathbf{e}_3 - \frac{d\mathbf{r}_i}{ds_i}\right)\frac{ds_i}{ds_1} \quad i = 1, ..., n \\ \dot{\mathbf{R}}_i &= \mathbf{R}_i(s_i)\widehat{\mathbf{u}}_i(s_i)\frac{ds_i}{ds_1} \quad i = 1, ..., n\end{aligned} \tag{4.30}$$

We define a state vector $\mathbf{y} = \{\mathbf{p}, \mathbf{R}, \mathbf{p}_1, \mathbf{R}_1, ..., \mathbf{p}_i, \mathbf{R}_i, s_i\}$ for $i = 1, ..., n$ which contains the kinematic state variables of the CPPR system and has corresponding derivatives with respect to s_1, which are $\dot{\mathbf{y}} = \{\dot{\mathbf{p}}, \dot{\mathbf{R}}, \dot{\mathbf{p}}_1, \dot{\mathbf{R}}_1, ..., \dot{\mathbf{p}}_i, \dot{\mathbf{R}}_i, \dot{s}_i\}$ (see equations (4.18), (4.29), and (4.30)) which are integrated over s_1. The polynomial coefficients for the free variables in (4.14) and (4.15) and the curvatures associated with the stiffness center frames of the tubes when straight (used in equation (4.16)) are concatenated into a single vector $\mathbf{x}$ as

$$\mathbf{x} = [\mathbf{a}, \mathbf{b}, \mathbf{c}_1, ..., \mathbf{c}_n]^\top \tag{4.31}$$

where $\mathbf{a} = [a_0, a_1, ..., a_k]$, $\mathbf{b} = [b_0, b_1, ..., b_k]$, and $\mathbf{c}_i = [c_{(0,i)}, c_{(1,i)}, ..., c_{(k,i)}]$ for $i = 1, ..., n$. Using the principal of minimum potential energy, the curvatures of the centerline and the tube stiffness centers along s_1 can be found by finding $\mathbf{x}$ that minimizes E, the total potential energy in the CPPR system. Thus, we have a minimization problem subject to nonlinear constraints:

$$\begin{aligned}&\min_{\mathbf{x}} \; E = E_F(\mathbf{y}_L) + \int_0^L \dot{E}_e(\mathbf{x}, \mathbf{y}, s_1) ds_1 \\ &\text{subject to } \mathbf{g}(\mathbf{y}_L)\end{aligned} \tag{4.32}$$

where $\mathbf{y}_L = \mathbf{y}(L)$ is the final state vector at L which is a function of $\mathbf{x}$, and $\mathbf{g}(\mathbf{y}_L)$ is the constraint function that contains the actuation boundary constraints (4.28) and the distal orientation boundary condition of (4.23), which implicitly is a function of $\mathbf{x}$.

The flowchart in Figure 4.4 provides a high-level walkthrough of the model. The following steps are taken to evaluate the objective function and the constraint violation residuals during a general iteration of the numerical optimization algorithm given tube actuator displacements q_i and external tip force $\mathbf{F}$:

1. Initial conditions $\mathbf{y}_0$ are provided based on initial stiffness center locations of each tube and their alignment at the base. The actuation displacements q_i are implemented into the initial conditions in (4.24) and (4.18).

2. An initial guess for the parameterized curvature $\mathbf{x}$ is provided to begin the optimization.

3. The state derivative $\dot{\mathbf{y}}$ that contains the kinematic differential equations of (4.18), (4.29), and (4.30), (which are calculated using equations (4.1)-(4.3), (4.13), (4.12), and (4.18)) are integrated for $s_1 \in [0\ L]$ to determine $\mathbf{y}$.

4. The total energy E is calculated by 4.22 where elastic energy E_e and distributed load energy E_f are computed by integrating (4.19) and (4.20) over the range $s_1 \in [0\ L]$, and tip load energy E_F is calculated by (4.21).

5. The residuals of the actuation and orientation constraints of (4.28) and (4.27) respectively are evaluated.

6. The optimization algorithm evaluates Jacobians and Hessians and chooses a new guess for $\mathbf{x}$ returning the process to step 2 until the termination criteria are met.

In our implementation, we used MATLAB's fmincon(), a packaged numerical solver for general constrained nonlinear optimization problems, using the interior-point method. All differential equations in the model are integrated with a fourth-order, adaptive stepsize, Runge-Kutta integration routine.

4.4 Tube Pattern Design and Parameter Characterization

In this section we discuss the design of the laser cut tubes with offset stiffness centers and characterization of their elastic parameters. For our parameter characterization, we use static finite element analysis (FEA) simulations to calculate the rigidity parameters used in the stiffness matrix $\mathbf{K}_i$ of equation (4.17) and the stiffness center locations x_i of the patterned tubes.

4.4.1 Tube Pattern Designs

We use a pattern of narrow slots cut into the tube walls with a fiber laser to shift the stiffness center away from the center of the tube cross-section and alter the flexural and torsional rigidity of the tube. The slot pattern contains interleaved slots such that a winding path of solid material remains, similar to so-called "serpentine" beams in MEMs literature [123]. The slotted pattern can vary along the length in order to change the mechanical properties. Three slot patterns, one designed for two-tube CPPRs with constant $\mathbf{r}_i$ (Figure 4.5), one designed for two-tube CPPRs with varying $\mathbf{r}_i$ (Figure 4.6) and another designed for 3D three-tube CPPRs with constant $\mathbf{r}_i$ (Figure 4.7) were used for our validation experiments. In Figures 4.5 (a) and 4.7 (a), the dark regions in the cross-section views are solid material. For the two tube CPPRs, we use a linear pattern of overlapping slots, forming a single serpentine pattern along the length of the tube as shown in Figure 4.5. The slot dimensions include the slot overlap angle α_i, backbone angle ϕ_i, slot pitch h_i, kerf λ and the length of tube that contains the slotted pattern L_i

For tube pattern used in our three tube robot, we used additional overlapping sections in the unit cell pattern that generate serpentine sections on three sides of the tubes. As each tube is required to bend in more than one plane in a three-tube CPPR, having large stiffness asymmetries can make actuation difficult, thus a tube

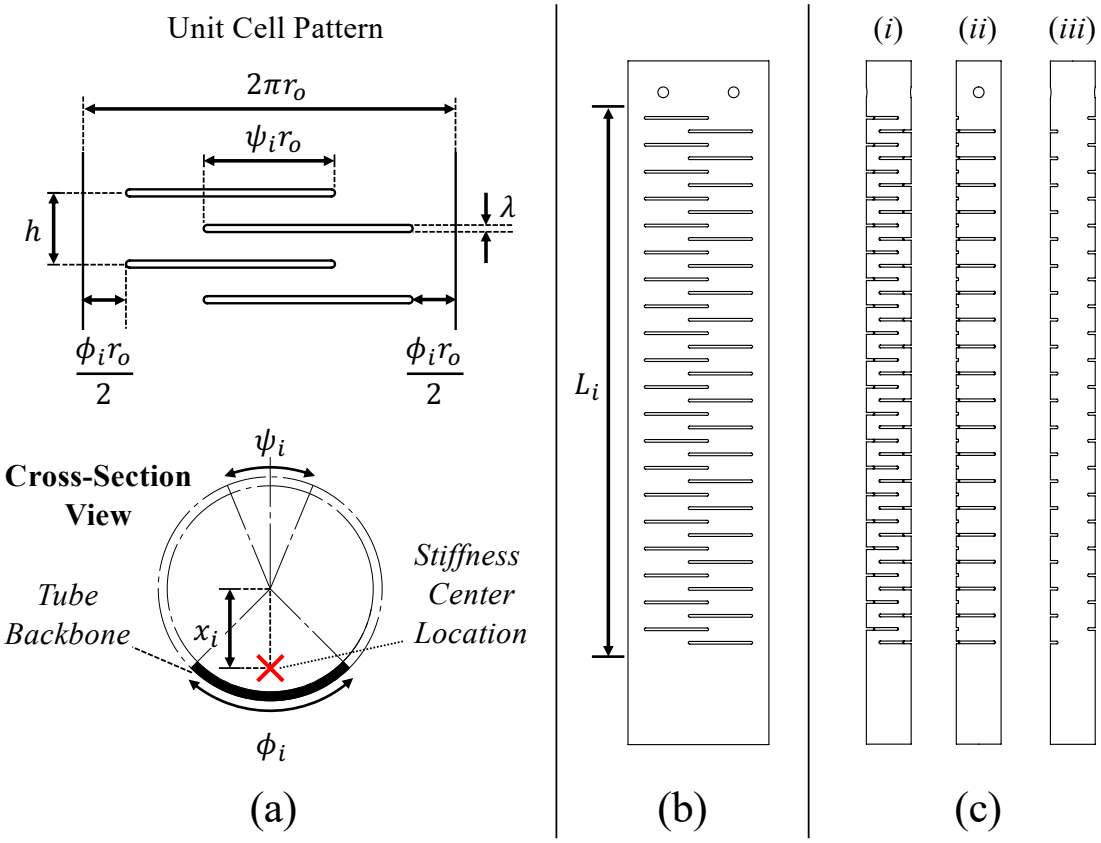


Figure 4.5: Slotted-tube pattern used to generate tube with offset stiffness centers. Slot parameters for a unit cell are shown in (a) with the 'unfolded' pattern design that is wrapped onto a nitinol tube (b). The resultant patterned tube is show from top (*i*), side (*ii*), and bottom (*iii*) views (c).

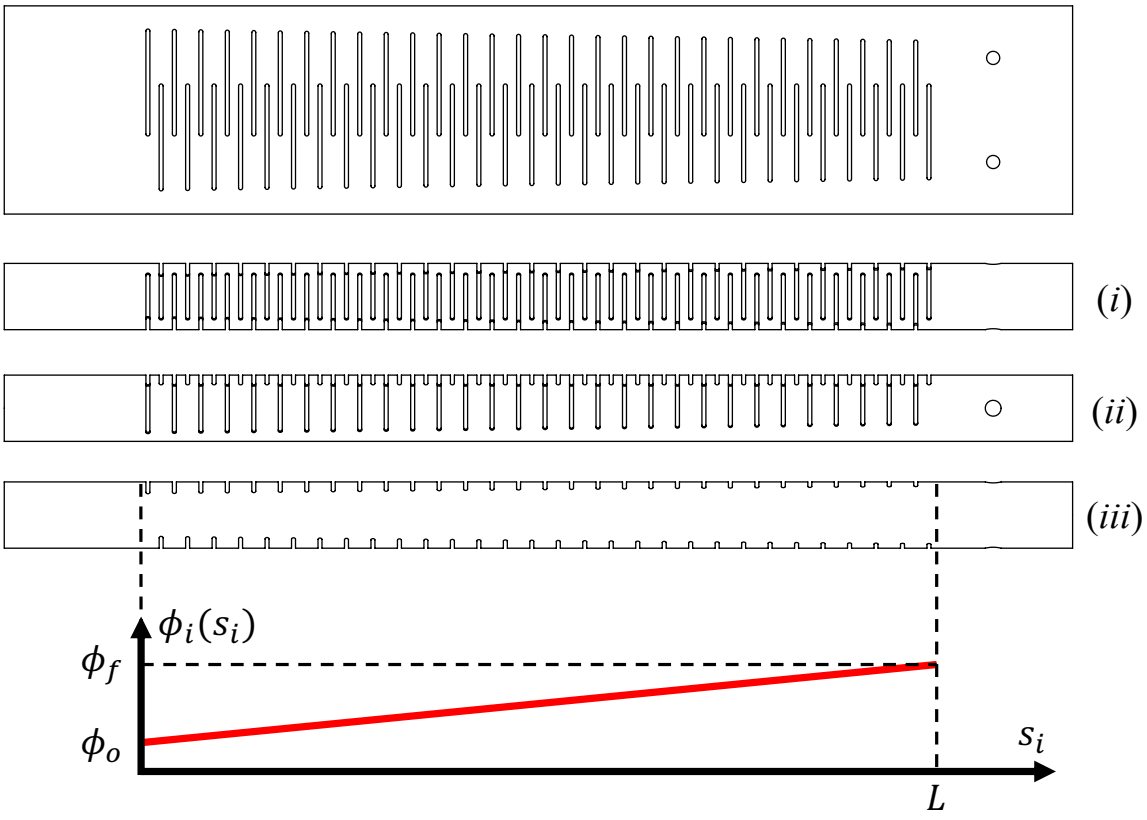


Figure 4.6: Converging tube design used for the Case 2 CPPR in which the backbone angle ϕ_i of each tube linearly tapers down the length of each tube as a function of s_i.

pattern that can achieve near symmetric flexural rigidity values for each tube (i.e. $(EI)_{x,i} \cong (EI)_{y,i}$) alleviates this issue. For all tube designs, a pulsed fiber laser was used to machine the slot patterns onto the tubes. The tubes in each prototypes were glued together to their tips using a cyanoacrylate glue.

4.4.2 Young's modulus calibration

In order to provide accurate FEA results for parameter characterization, we calibrated Young's modulus for each tube. The Young's modulus is found by fitting small deflection force-displacement data from a three-point flexural setup, as shown in Figure 4.8 and using the Euler-Bernoulli beam equation for a simply supported beam with a midpoint load applied:

$$\delta = \left(\frac{1}{E_i}\right)\frac{F_E L_E^3}{48I} \tag{4.33}$$

where E_i is the Young's modulus of the i^{th} tube, F_E is the applied midpoint force, L_E is the length of the simply supported beam , I is the second moment of area of the tube, and δ is the midpoint displacement of the beam. For our validation experiments, we use three different tube sizes, which are tabulated in Table 4.2. The length L_E used for all tube cases was 90mm. Each tube is simply supported with rollers at each end. A linear actuator (Thorlabs MTS50-Z8), controlled by a DC servo motor controller (Thorlabs KDC101), is used to apply a displacement δ at the midpoint along the beam. The midpoint force F_E at each displacement is recorded with a force gauge (ATI Mini40) at each applied displacement. A displacement range from 0 to 2mm in 0.1mm increments was used for the modulus calibration. A linear fit is performed on the dictated midpoint displacements as the dependent variable and $F_E L_e^3/48I$ as the independent variable. The slope of the linear fit corresponds to $(1/E_i)$. The calibrated Young's moduli for each tube is tabulated in Table 4.2, which are within the expected Young's modulus range for nitinol. The coefficient of determination for each fit of (4.33) was 0.99, ensuring displacements to the tubes were

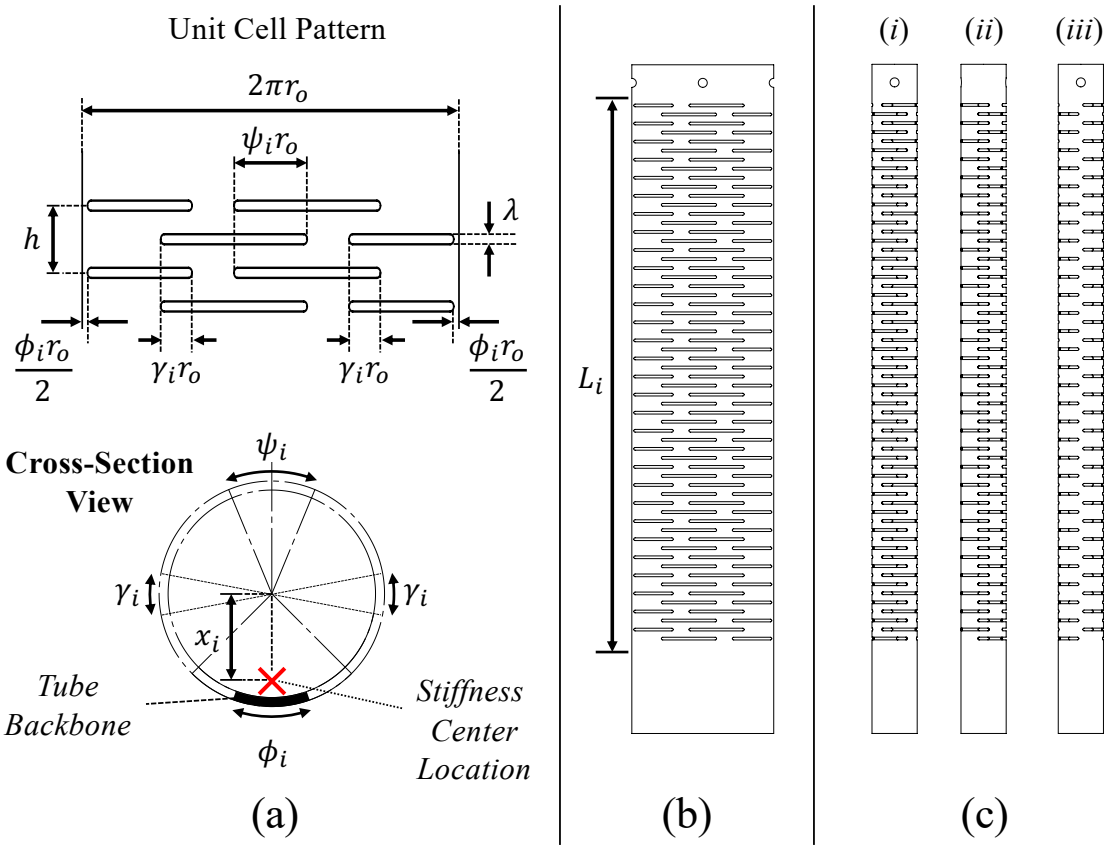


Figure 4.7: Slotted-tube pattern used for three-tube CPPR experiments. Slot parameters for a unit cell are shown in (a) with the 'unfolded' pattern design that is wrapped onto a nitinol tube (b). The patterned tube is shown from a top (i), side (ii), and bottom (ii) views in (c). Note that the additional overlaps from γ_i create additional slots on the side of the tube, thus enabling improved design of both flexural rigidity values of the tube.

Table 4.2: Nitinol Tube Dimensions and Calibrated Mechanical Properties

	r_o (mm)	r_i (mm)	E_i (GPa)	ν	G_i (GPa)
Tube 1	1.25	1.18	56.27	0.33	21.15
Tube 2	1.095	1.016	73.43	0.33	27.61
Tube 3	0.900	0.811	68.48	0.33	25.74

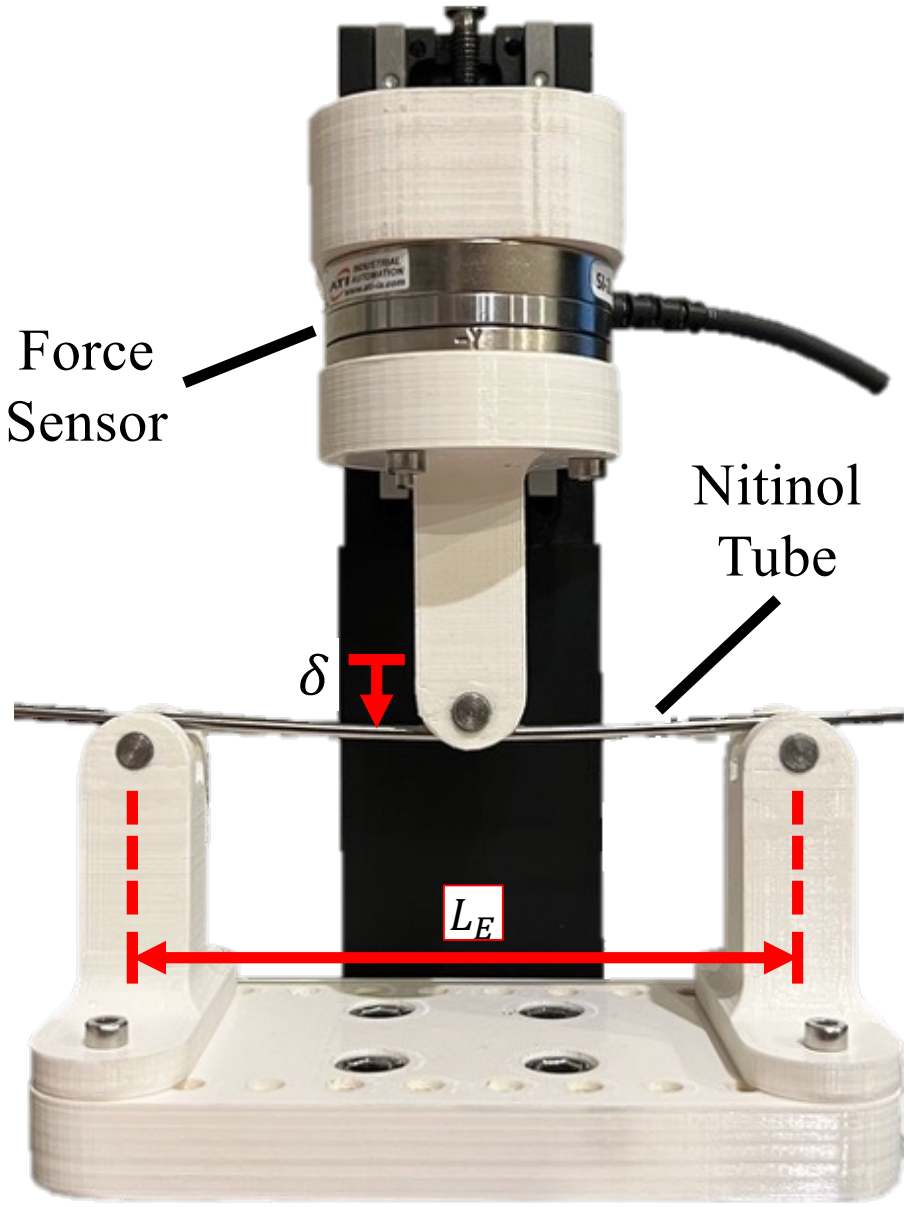


Figure 4.8: Three point flexural test setup used to calibarate the Young's modulus E of each nitinol tube. The moduli values are then used in our FEA simulations to determine the flexural and torsional properties of our patterned tubes.

within the linear elastic region of deflection. The experimentally determined Young's moduli are then implemented into the FEA material model for each tube.

4.4.3 Parameter Characterization

This subsection details our procedure for calculating the flexural and torsional rigidity values used in (4.17) and the stiffness center offset $\mathbf{r_i}$ for each patterned tube using FEA. Solidworks Simulation Premium was used as our FEA package, using a linear elastic material model and shell elements. The proximal base of the tube is rigidly fixed in translation and rotation while tip moments are applied at the tip, as shown in Figure 4.9.

To calculate the effective flexural rigidity values $(EI)_{x,i}$ and $(EI)_{y,i}$ in FEA, we apply apply moments at the distal tip of the patterned tube of length L_{FEA} and record the resultant bend angle:

$$\begin{aligned} (EI)_{x,i} &= \frac{M_x L_{FEA}}{\theta_x} \\ (EI)_{y,i} &= \frac{M_y L_{FEA}}{\theta_y} \end{aligned} \tag{4.34}$$

where L_{FEA} is the length of the patterned tube used in the FEA simulation, M_x and M_y are applied tip moments about the global x- and y-axes respectively, and θ_x and θ_y are the resultant bend angles about the x- and y-axes respectively. Moments at the tip are created by applying two point forces at the tip, each with equal magnitude but opposite directions, separated by a distance of outer diameter of the tube, (i.e. $M_x = 2F_x r_o$ and $M_y = 2F_y r_o$). The value of each point force was 0.01N and the bend angle is calculated using a small angle approximation from the maximum and minimum z-displacements from the applied moment, $\theta_x = (Z_{max} - Z_{min})/(2r_o)$.

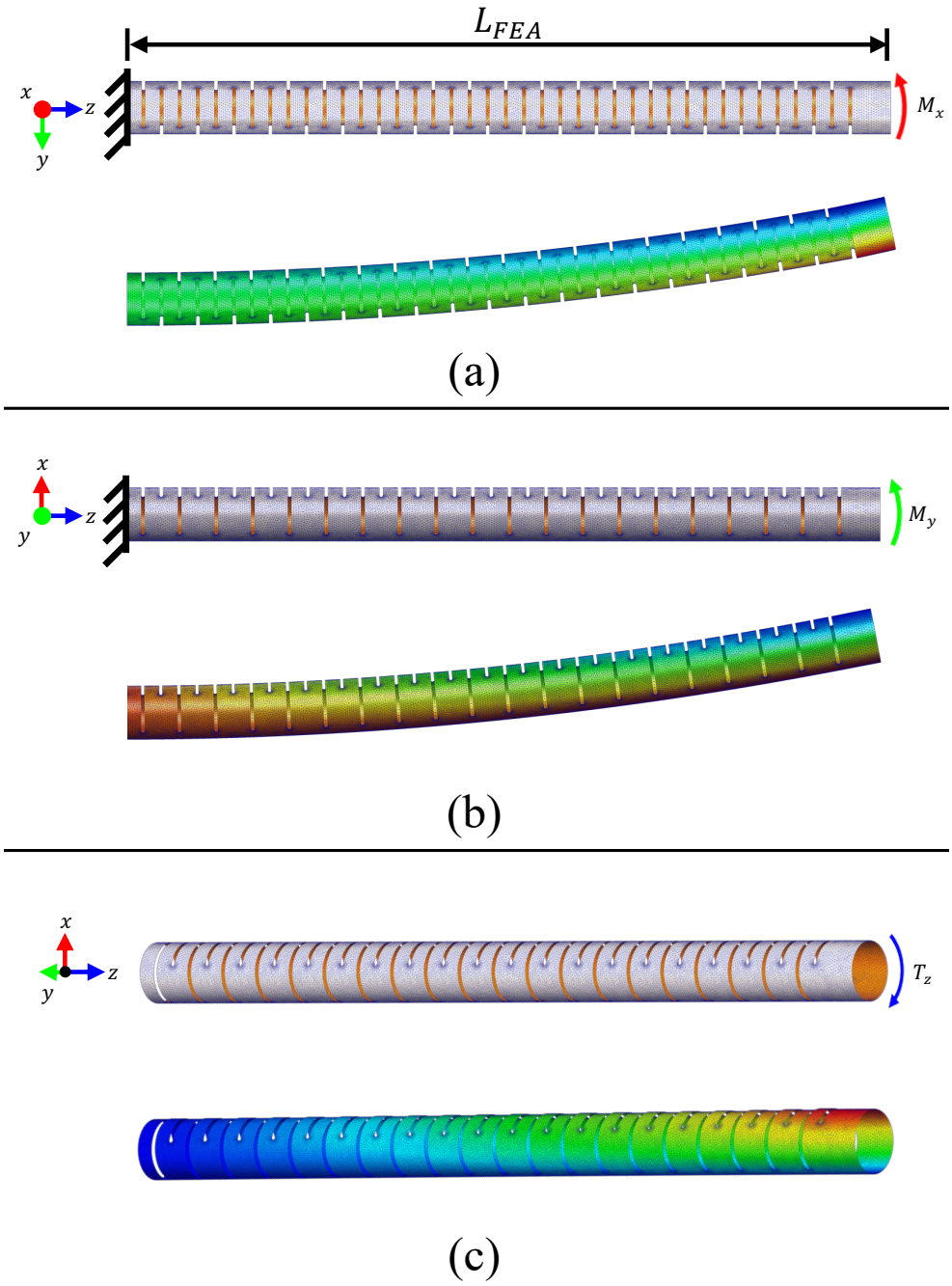


Figure 4.9: FEA Setups for calculating the flexural rigidity about x $(EI)_{x,i}$ (a), flexural rigidity about y $(EI)_{y,i}$ (b), and torsional rigidity $(GJ)_i$) (c).

To estimate the effective torsional rigidity $(GJ)_i$, we apply a torque M_z about the global z-axis at the tip of the patterned tube and record the resultant rotation θ_z:

$$(GJ)_i = \frac{M_z L_{FEA}}{\theta_z} \tag{4.35}$$

To generate the torque T_z, we apply four distal forces at the tip to generate a torque about the tube z-axis. Each point force has a magnitude of 0.01N and the proximal base is fixed in translation an rotation. The rotation angle θ_z is similarly calculated using the resulting displacements.

To calculate the stiffness center location x_i, we use the maximum and minimum z-displacements, Z_{max} and Z_{min} respectively, from the $(EI)_{y,i}$ test:

$$x_i = r_o - \frac{2r_o}{1 + |\frac{Z_{max}}{Z_{min}}|} \tag{4.36}$$

4.5 Experimental Validation

To validate our model, we compare our model predictions with laser cut nitinol CPPRs for three design cases. Case 1 uses a pair of patterned tubes with constant stiffness center locations along the length of the tube, Case 2 uses a pair of patterned tubes with varying stiffness center and mechanical properties down the length of the tube, and Case 3 uses three tubes with constant stiffness center locations as shown in Figure 4.7. The tube alignment for each design case is shown in Figure 4.10. For the two tube designs, the backbones are aligned 180^o apart from each other about the center of tube pair. For the three tube design, the stiffness centers are 120^o apart in the cross-section. We actuate each CPPR design across its workspace and compare model predictions with the tip positions from the physical robots. For cases 1 and 2, we also analyze the deflection under a tip load across the workspace.

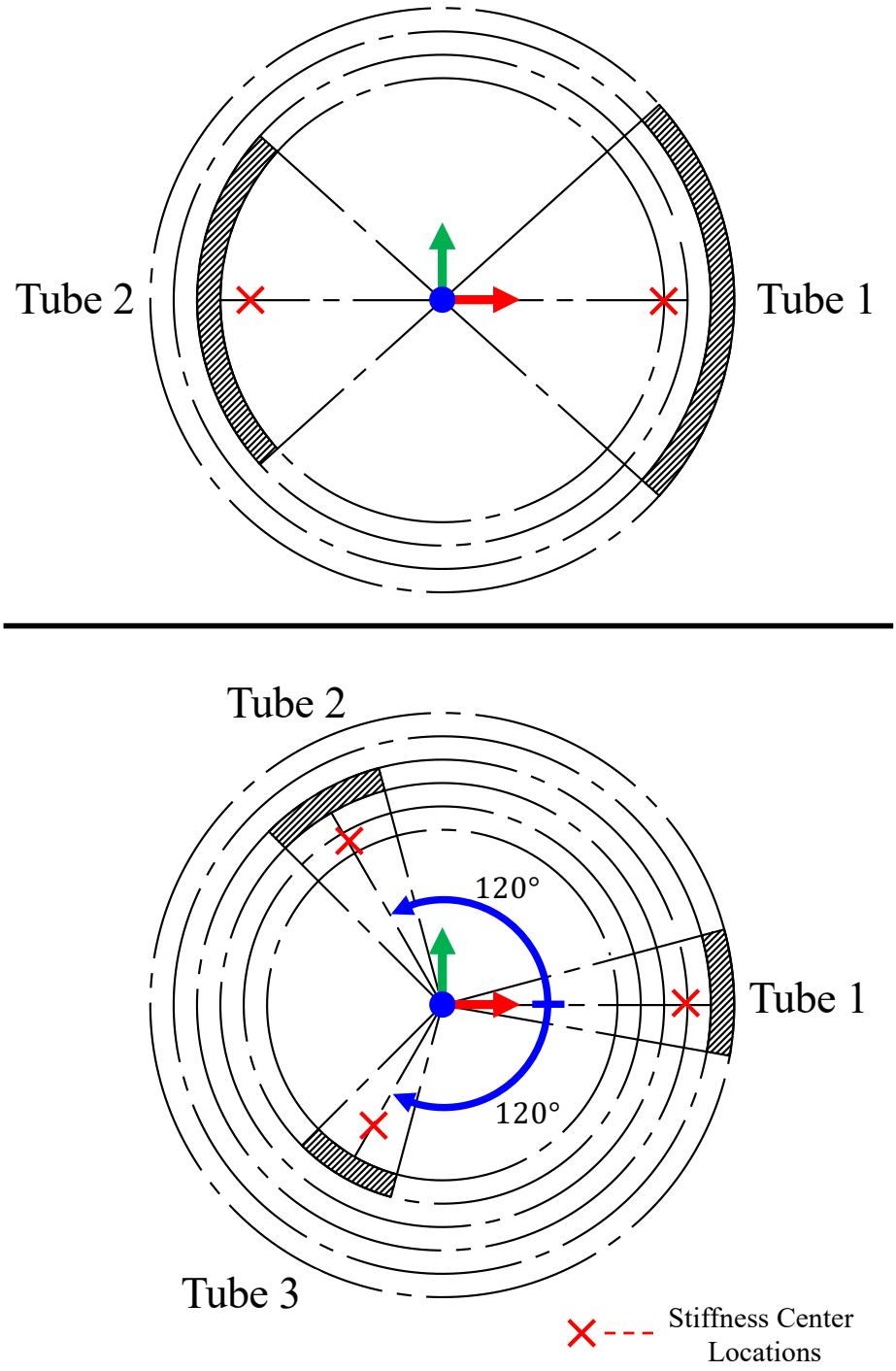


Figure 4.10: Tube alignments for the two-tube CPPRs (top) and three tube CPPRs (bottom). The principal axes at the center for both alignments indicate the origin of the centerline in relation to the stiffness center locations of each tube.

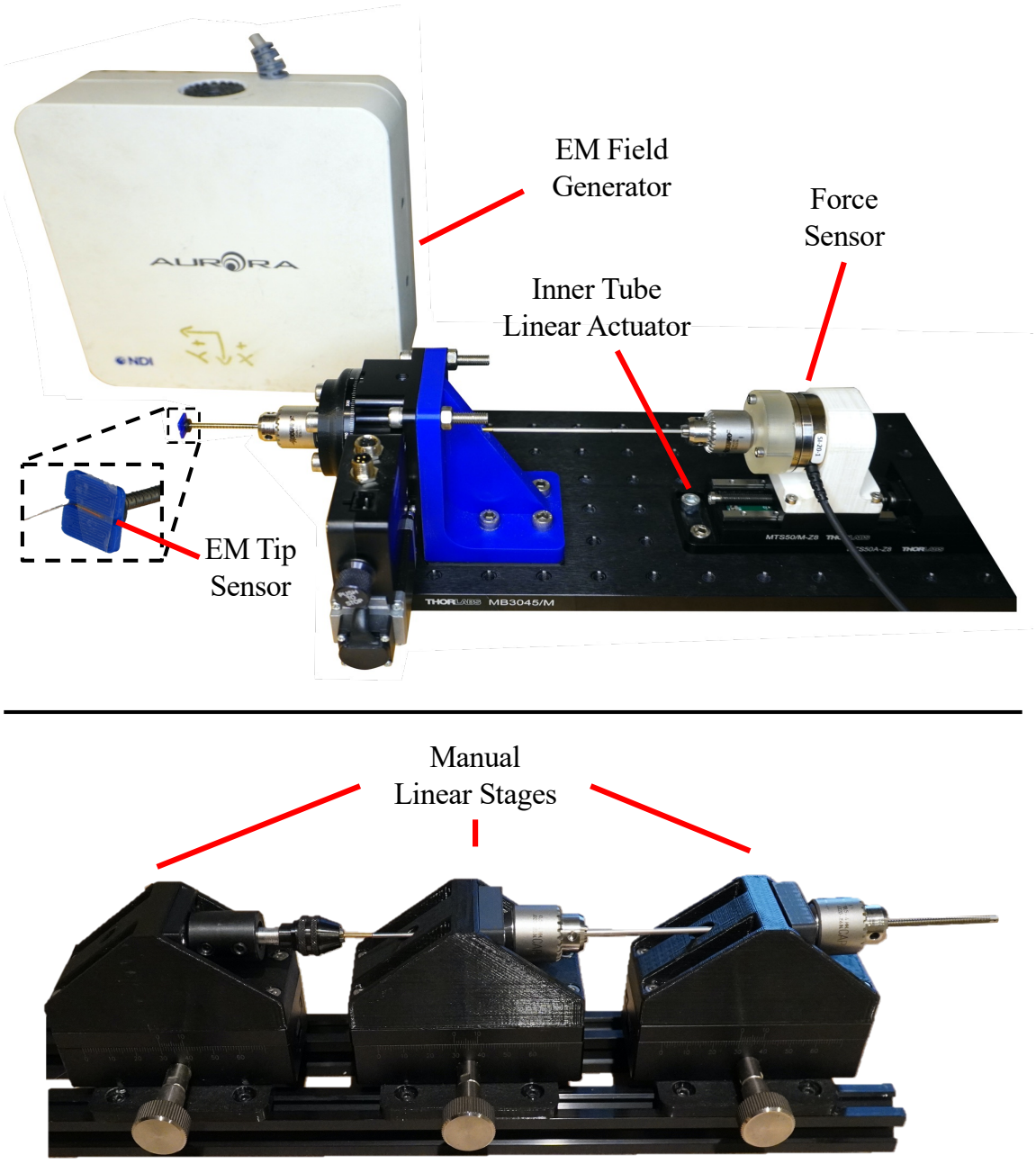


Figure 4.11: Actuation setups for 2-tube CPPRs (top) and 3-tube CPPRs (bottom).

4.5.1 Experimental Setups

We developed two actuation setups for our model validation experiments, a motorized setup for 2-tube CPPRs and manual setup for the 3-tube CPPR. The our 2-tube CPPR uses a motorized linear stage (Thorlabs MTS50-Z8) to actuate the inner tube while the outer tube remains fixed. Through-hole drill chucks (Accupro 55162614) are used to grip the inner and outer tubes to the actuation setup. The distal tip positions of the CPPR prototypes are tracked using an electromagnetic tracker system (NDI Aurora).

For our 3-tube CPPR experiments, we use manual linear stages (Optics Focus MDX-4090-60) to translate tubes 2 and 3 while keeping tube 1 fixed. The drill chucks and electromagnetic tracker system from the 2-tube actuation setup are also used in the 3-tube setup.For each of our experiments, we perform a rigid point-set registration of corresponding experimental and model actuation poses for each case.

4.5.2 Case 1: Two-Tube, Constant Stiffness Center Location

Tube 1 serves as the outer tube and Tube 2 is the inner tube from Table 4.2. The slot parameters of the design are shown in Table 4.3 and the resultant mechanical properties of both tubes are listed in Table 4.4. An additional 3mm is added to the tip of the tube pair to accommodate the EM sensor attachment. We assess the model accuracy by actuating the robot across its workspace and recording the tip pose at each actuation pose. We compare model predictions with experimental results in free space and with a distal tip loads applied in the plane of bending and out of the plane of bending. For the free workspace, we actuate the robot across a $\pm$3mm displacement range of the inner tube, actuating the inner tube in 0.25mm increments and recording the distal tip position at each pose. Figure 4.12 shows the range of motion at $\pm$3mm actuation limits and in the straight, unactuated case. We performed a rigid registration of the experimental data to the model data. The largest

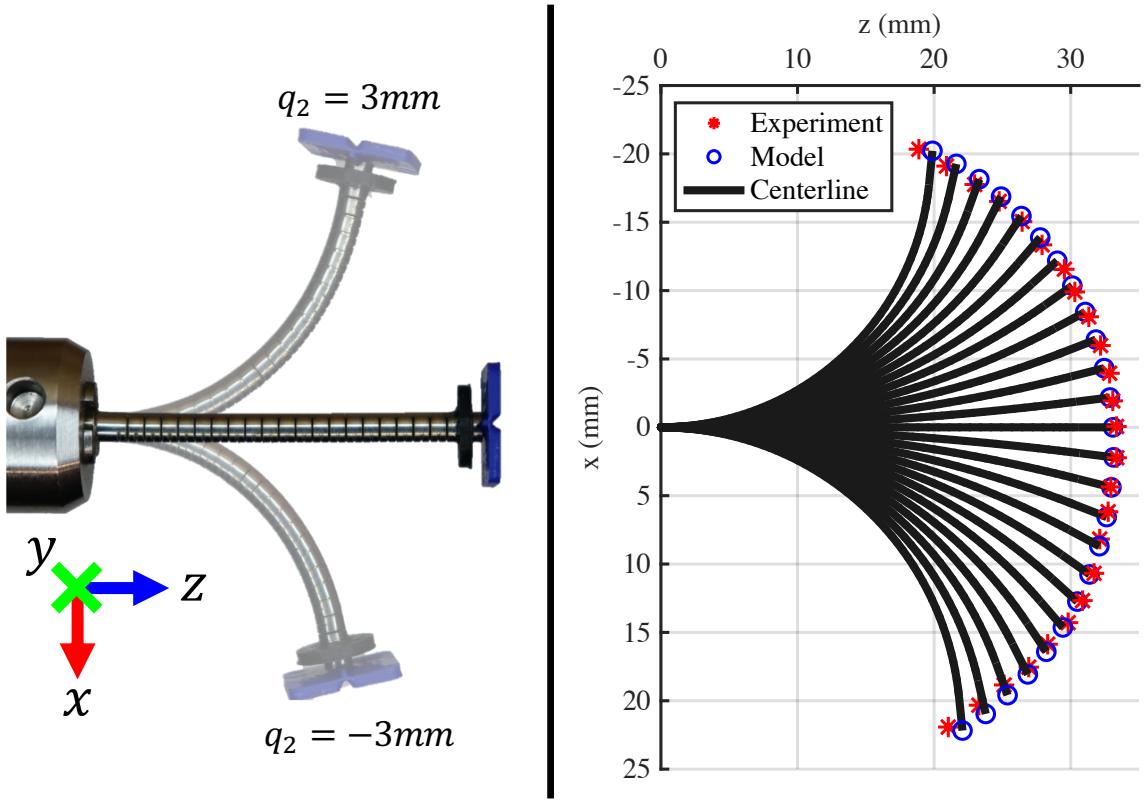


Figure 4.12: Case 1 CPPR (constant $\mathbf{r}_i$) workspace while unloaded while actuated to $\pm 3mm$ (left). Tip position of the CPPR are recorded at each pose and compared with model predictions (right).

pose error in the unloaded case occurred at $q = -3mm$, where the error was 1.12mm, approximately 3.6% of the overall active length of the robot.

For our tip load, we use attach a 50g weight (0.49N) and record the tip position at each pose. The in-plane loading cases use an inner tube displacement range of $\pm 1.25mm$ in 0.25mm increments. The in-plane loading data set is shown in Figure 4.13. The maximum error occurred at the maximum pulling displacement of tube 2, $q_2 = 1.25mm$, which had a tip error of 0.9mm, approximately 3% of the robot length. The out-of-plane tip loading cases use an inner tube displacement range of $\pm 1mm$, recorded poses in 0.25mm increments. The out-of-plane loading data set is shown in Figure 4.14. The tip position error statistics for the loaded and unloaded cases are recorded in Table 4.5. As we can see from comparing the results of the in-plane and out-of-plane loading results, the stiffness of the CPPR is much greater in the out-of-plane bending direction. In the straight, cantilevered cases for each loading case ($q_2 = 0$), the transverse deflection while loaded in-plane was 3.72mm and the transverse deflection while loaded out-of-plane was 1.36mm.

4.5.3 Case 2: Two Tube, Varying Stiffness Center Location

In this design case, we analyze the accuracy of the kinetostatic model over a wide range of actuation values, with and without tip loads, on a CPPR with tubes having varying stiffness center locations and mechanical properties along the length of the tube. The tube pattern begins with a stiffness center offset from the center at the base and linearly converges toward the centerline at the distal tip. The rationale behind this design choice stems from the results of [67] and [116] in which a tendon-actuated continuum robot uses converging tendon routing to improve its resistance to tip loads. To create a patterned tube with a varying stiffness center, we use the slotted serpentine pattern shown in Figure 4.6 and vary the backbone angle ϕ_i down the length of each tube. The remaining slot parameters are kept constant down the length of the tube as tabulated in Table 4.6.

Table 4.3: Slot parameters used for Case 1 CPPR

	ϕ_i (deg)	ψ_i (deg)	λ (mm)	h (mm)	L_i (mm)
Tube 1	90	120	0.15	1.5	30
Tube 2	90	90	0.15	1.5	37.5

Table 4.4: Mechanical Properties of Case 1 Sheaths

	$(EI)_{x,i}$ (Ncm^2)	$(EI)_{y,i}$ (Ncm^2)	$(GJ)_i$ (Ncm^2)	$x_i(s_i)$ (mm)	α_i (deg)	β_i (deg)
Tube 1	17.83	1.25	1.08	-1.09	0	0
Tube 2	20.70	1.85	1.71	0.94	0	0

Table 4.5: Tip Position Error Statistics of Case 1

Loading Case	Max. Error (mm)	Min. Error (mm)	Mean Error (mm)	Std. Dev. (mm)
Unloaded	1.12	0.07	0.54	0.24
Loaded In-Plane	0.90	0.14	0.47	0.29
Loaded Out-of-Plane	2.81	0.36	1.24	0.7

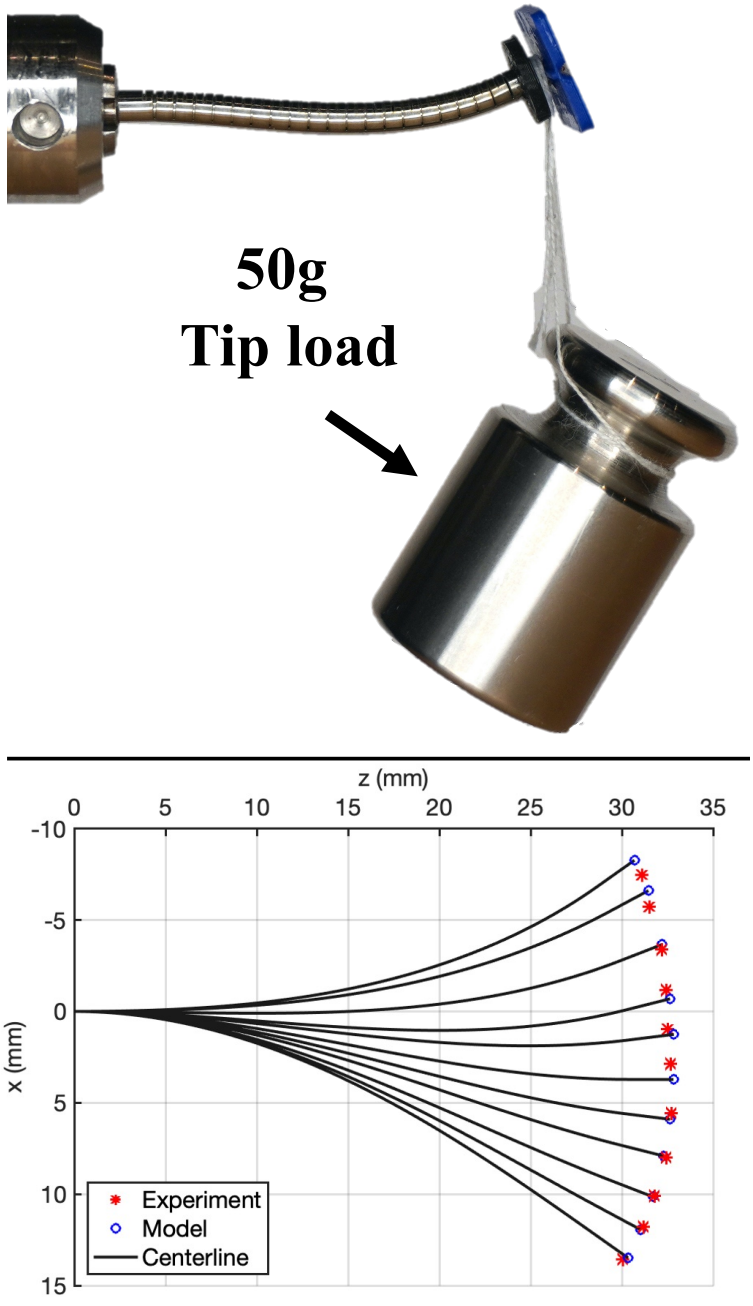


Figure 4.13: Case 1 CPPR with 50 gram load applied in the plane of bending while the inner tube is actuated at 1.25mm (top). Actuated configurations from -1.25mm to 1.25mm in 0.25mm increments (bottom).

We use the following linear function to taper the backbone angle down the length of the tubes:

$$\phi_i(s_i) = \left(\frac{\phi_f - \phi_o}{L_i}\right) s_i + \phi_o \tag{4.37}$$

where ϕ_o is the backbone angle at $s_i = 0$, ϕ_f is the backbone angle at $s_i = L_i$. Tubes 1 and 2 use $\phi_o = 80^o$ and $\phi_f = 120^o$ in this design case. In addition, the rigidity parameter values will also be affected by the changing backbone design and will need to be functions of s_i as well. To characterize $(EI)_{x,i}$, $(EI)_{y,i}$, $(GJ)_i$, and x_i over the range of backbone overlap angles, we perform a parameter sweep of the constant slotted tube design in Figure 4.5 using a constant ϕ_i using the calibration process used in Section 4.4 for Tubes 1 and 2. In these parameter sweeps, ϕ_i is the only varied parameter while the remaining slot parameters remained unchanged, as listed in Table 4.6. The parameter sweep results are plotted in Figure 4.15 for the flexural and torsional rigidity values and stiffness center locations. A polynomial regression of the parameter sweep data is performed to generate polynomial functions of the rigidity parameters and the stiffness center locations as functions of the backbone angle of the tube. For the rigidity parameters, we use a quadratic polynomial and use a linear fit for the stiffness center locations.

The coefficient of determination of all fits was greater the 0.98, confirming our polynomial order for each case is a good fit for the data. The quadratic fits for the rigidity parameters are implemented into the stiffness matrix $\mathbf{K}_i$ for each tube in equation (4.17) and the stiffness center linear fits are implemented into $\mathbf{r}_i$ for each tube in equation (4.2) for the energy minimization in (4.32).

For the free and in-plane loaded pose data sets of the Case 2 CPPR, we actuated tube 2 $\pm$1.25mm in 0.25mm increments. Like the Case 1 CPPR, we use a 50g weight at the tip. The free workspace result is shown in Figure 4.16 and the loaded workspace in Figure 4.17. The tip error statistics of the free and loaded data sets are tabulated in Table 4.7. In free space, the largest error occurred at $q_2 = -1.25mm$ and while loaded, the largest error occurred at $q_2 = 1.25mm$; the second largest error for the loaded

workspace was $q_2 = 1.25mm$. In future applications and designs, the mechanical properties could vary down the length either as a means for increasing the strength of the overall structure or for making the tip more flexible to enable tip-first bending.

4.5.4 Case 3: Three Tube, Constant Stiffness Center Location

For our patterned tubes, we use the three serpentine pattern shown in Figure 4.7 with the design parameters tabulated in Table 4.9 and mechanical properties for each tube are listed in Table 4.8. The stiffness center locations of each tube are 120^o apart from one another about the global z-axis which is inspired by the actuation setups of many tendon-driven [124] and pressure-driven [125] continuum robot designs.

Tube 1 remains fixed for all workspace poses. When either tube 2 or 3 is actuated and the two other tubes remain fixed, the robot bends in the direction of the stiffness center location of the actuated tube. When tubes 2 and 3 are actuated at the same magnitude and direction, the robot undergoes bending in the direction of tube 1. These actuation poses are shown in Figure 4.18. For our model validation, we actuate tubes 2 and 3 over a $\pm 1mm$ range in 0.5mm increments. The result comparing the three tube prototype with the model prediction is shown in Figure 4.19. The tip error statistics are tabulated in Table 4.10. The largest tip error occurred for the $q_2 = 0$mm, $q_3 = 1$mm configuration and the second largest tip error occurred for the $q_2 = 1$mm, $q_3 = 0$mm configuration (which was a 1.21mm error).

4.5.5 Error Sources

As in the case for CTRs, friction can play a role in model accuracy. As the clearance between the tubes gets smaller and the length of the tubes is larger, it's more likely to see the effects of friction. In addition to friction, other sources of model error can

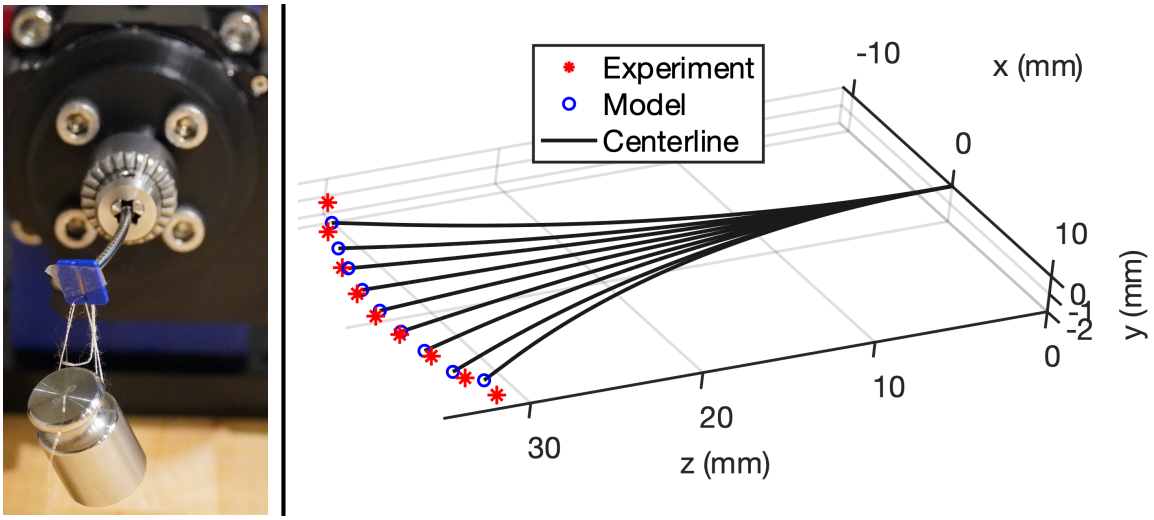


Figure 4.14: Case 1 CPPR with 50 gram load applied out of the plane of bending while the inner tube is actuated at 1.00mm (left). Actuated configurations are from -1mm to 1mm in 0.25mm increments (right).

Table 4.6: Constant slot parameters used for Case 2 CPPR

	ψ_i (deg)	λ (mm)	h (mm)	L_i (mm)
Tube 1	90	0.15	1.0	30
Tube 2	90	0.15	1.0	35

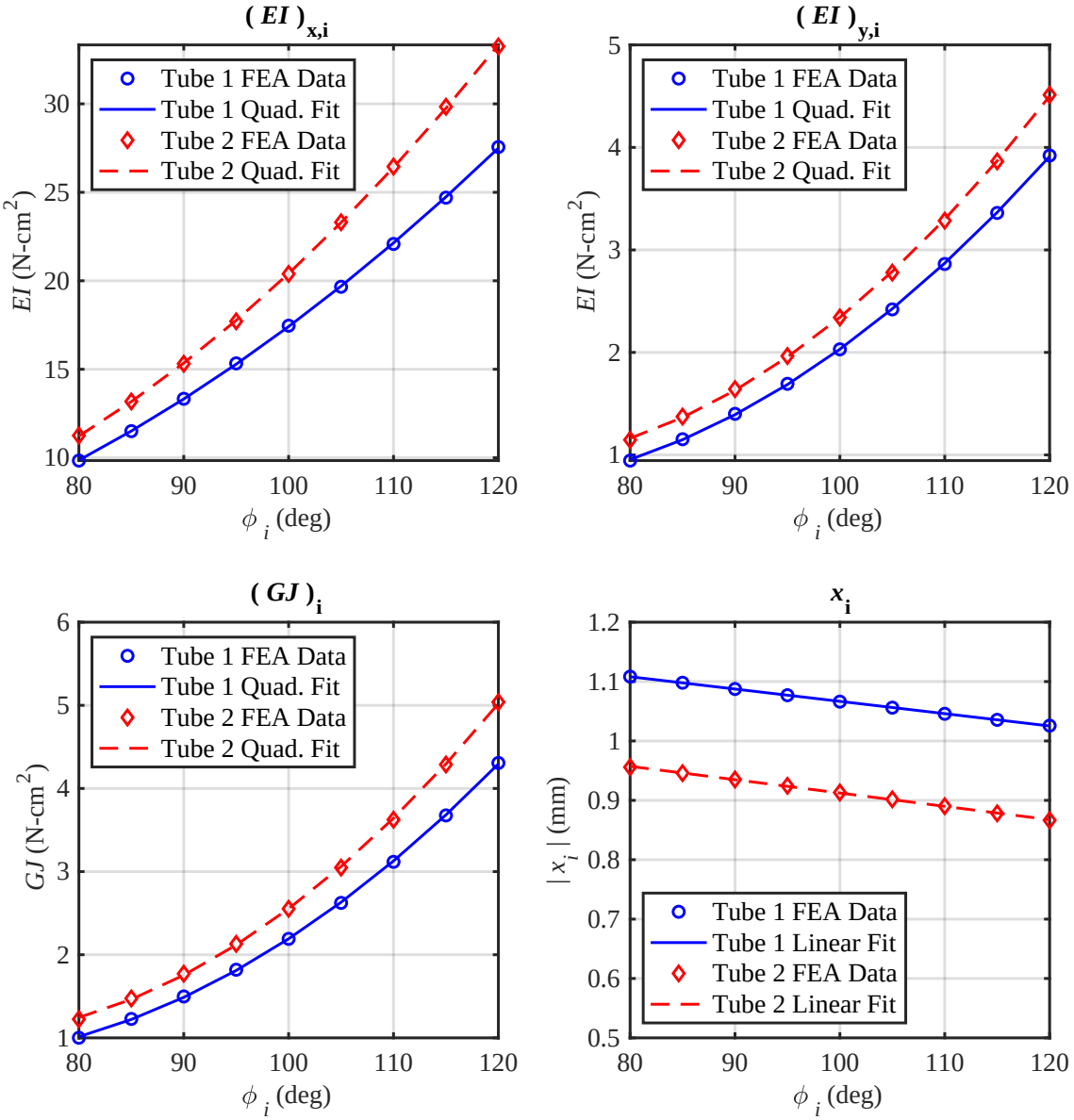


Figure 4.15: Parameter sweep of flexural, rigidity, torsional rigidity, and stiffness center location of tubes 1 and 2 for Case 2 CPPR.

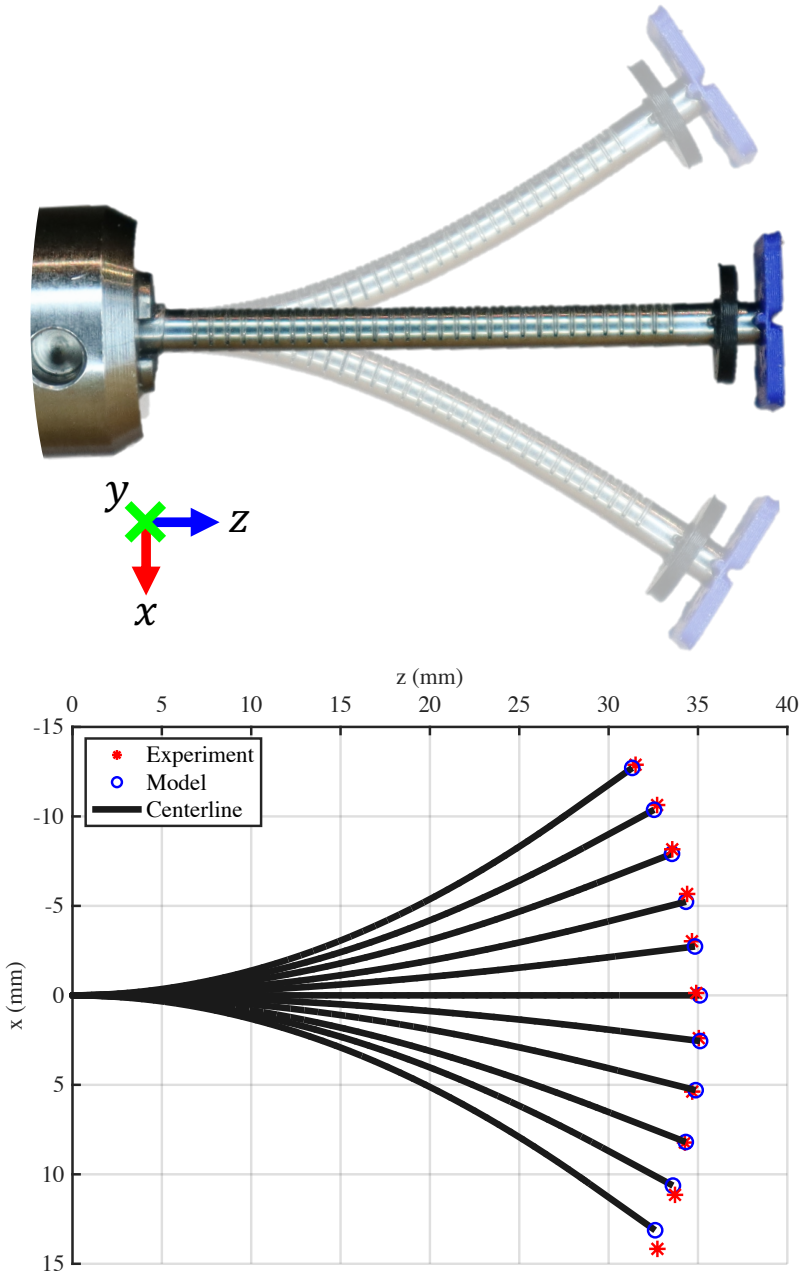


Figure 4.16: Case 2 CPPR prototype actuated to ±1.25mm (top) and the resultant workspace of the experimental prototype and comparison with our model predictions (bottom).

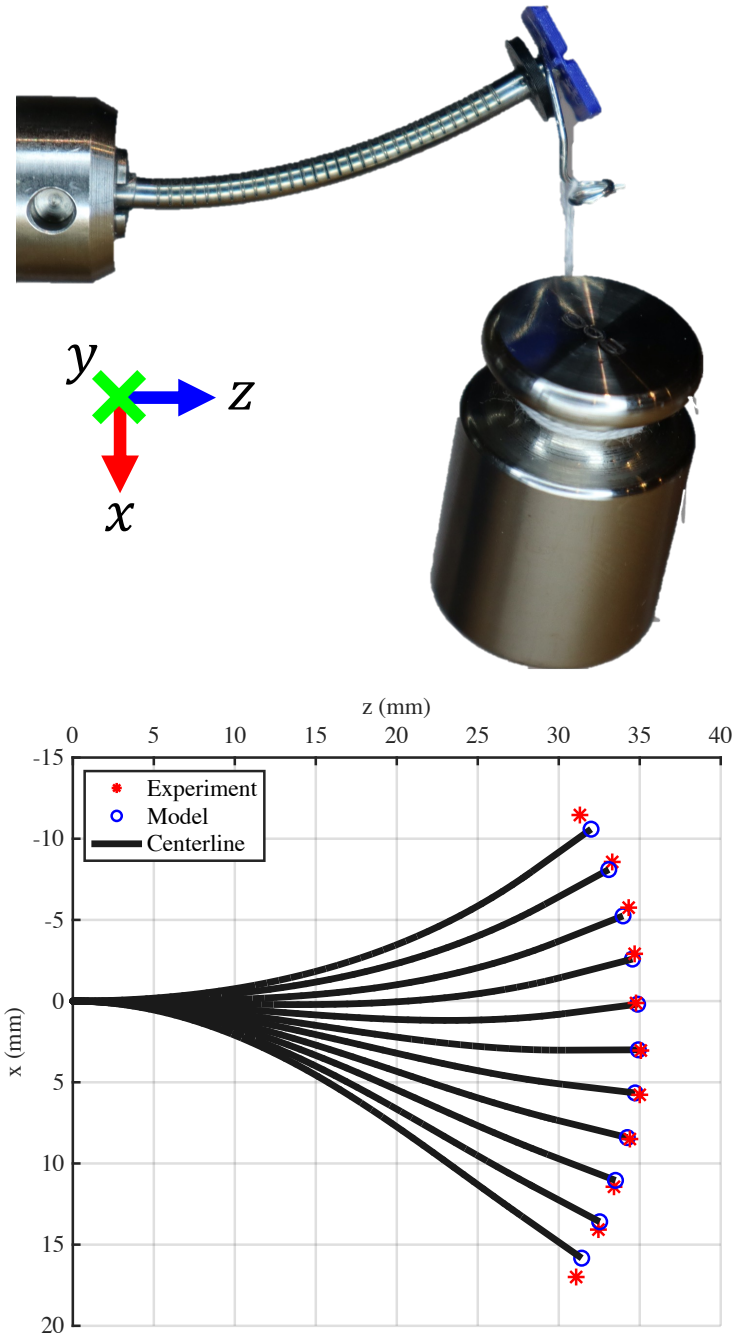


Figure 4.17: Case 2 CPPR prototype shown with 50g tip laod (top) and the resultant workspace with the tip load applied (bottom).

Table 4.7: Tip Position Error Statistics of Case 2

Loading Case	Max. Error (mm)	Min. Error (mm)	Mean Error (mm)	Std. Dev. (mm)
Unloaded	1.05	0.06	0.35	0.26
Loaded	1.21	0.13	0.51	0.36

Table 4.8: Slot parameters used for Case 3 CPPR

	ϕ_i (deg)	ψ_i (deg)	γ_i (deg)	λ (mm)	h (mm)	L_i (mm)
Tube 1	10	70	30	0.15	1.0	30
Tube 2	10	70	40	0.15	1.0	34
Tube 3	10	70	40	0.15	1.0	34

Table 4.9: Tube Parameters of Case 3 Sheaths

	$(EI)_{x,i}$ (Ncm^2)	$(EI)_{y,i}$ (Ncm^2)	$(GJ)_i$ (Ncm^2)	$x_i(s_i)$ (mm)	α_i (deg)	β_i (deg)
Tube 1	1.96	1.78	2.73	-1.12	0	0
Tube 2	1.81	1.78	2.78	-0.983	120	120
Tube 3	1.83	1.89	2.91	-0.764	240	240

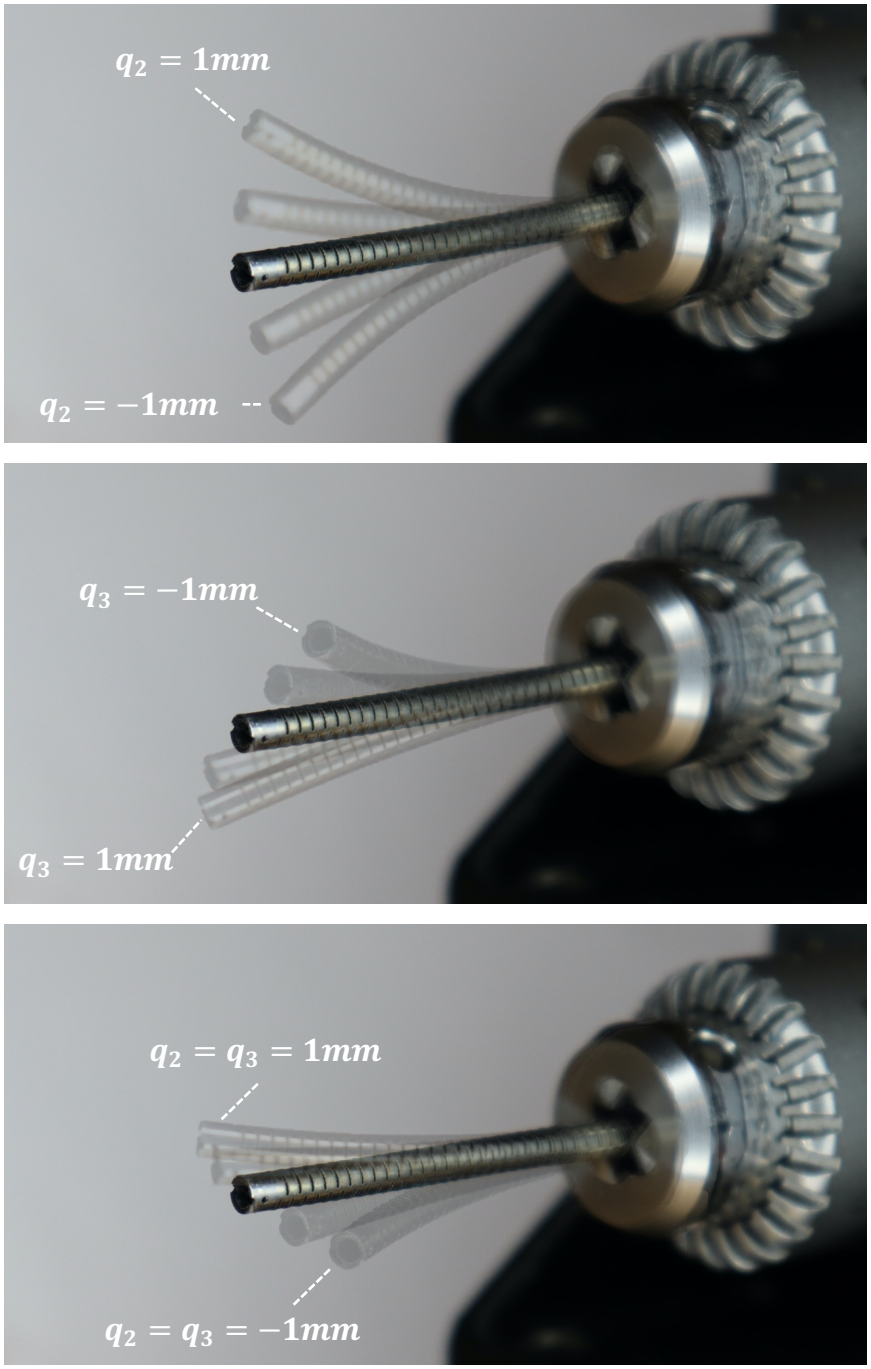


Figure 4.18: Three tube robot actuation poses showing displacements of just tube 2 (left), just tube 3 (middle) and both tubes in equal direction and displacement (right).

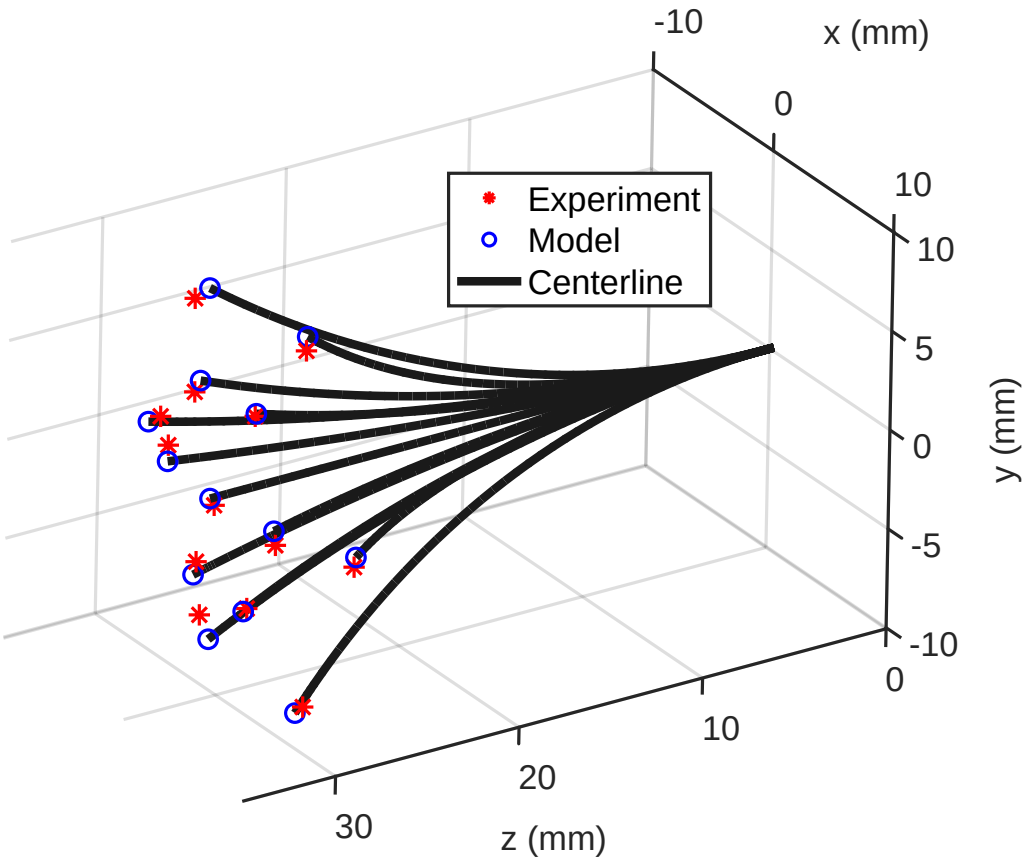


Figure 4.19: Workspace of three tube CPPR showing model predictions compared with experimental results.

Table 4.10: Tip Position Error Statistics of Case 3

	Max. Error (mm)	Min. Error (mm)	Mean Error (mm)	Std. Dev. (mm)
Unloaded	1.98	0.22	0.83	0.44

occur error in the parameter characterization process, the CPPR fabrication process, and in unmodeled physical effects such as shear and axial deformations.

Errors in the actual span length L_E used to calibrate the Young's modulus plays an important role, as the span length term in equation (4.33) is cubed. Tube misalignment , which can occur from the gluing process. If the clearance between the tubes is too large, the inner tube(s) may be glued to the walls of the outer tube during the glueing process, nullifying the concentricity constraint.

Thermal effects from laser machining have also been found to play a role in altering the microstructure and mechanical properties of Nitinol [126], thus the actual Young's modulus of the laser patterned tubes may be slightly altered from the uncut tube. In addition, the Kirchhoff tube assumption used in the model does not account for shear and axial deformations. The role of these effects should be further studied in future work as model accuracy would decrease for CPPRs with low axial stiffness and under large axial forces, either from actuation or from external loads. Some of these errors could be mitigated through simultaneous calibration of the rigidity and stiffness offsets of the tubes with the registration of the experimental pose data. Furthermore, these errors can be mitigated, depending on the operation of the CPPR. In robotic applications, errors can be mitigated from the operator in a tele-operated system or through a model-based controller in closed-loop control. However, based on the low errors in the current set of experiments, the influence of these error sources are negligible in the calibration and experimental setups.

4.6 Conclusion

In this paper, we developed a general kinematics model for CPPRs, expanding the capabilities for design and analysis of these tubular robot actuators. The kinematics-statics model was derived, starting with the kinematics of a single tube and culminating with the solution of the overall CPPR kinematics using the principal of minimal energy. An FEA-based parameter characterization was demonstrated to

estimate the mechanical properties of patterned tubes with offset stiffness centers. Two- and three-tube CPPR design cases were created to test the capabilities of the model. The model shows good agreement for all case designs and has similar levels of accuracy to the state of the art models for other types of continuum robots.

We envision that this model will be useful for the design of CPPRs toward future surgical applications, providing kinematic analysis that can account for manipulator interactions with the environment and allow the design optimization of generally patterned tubes for procedure-specific workspaces and force requirements. Furthermore, the model we developed here can be the basis for the development of intrinsic force sensing and control algorithms in future robotic implementations of CPPRs.

Chapter 5

Conclusions

Continuum robots are characterized by their dexterity, ability to traverse complex pathways, and compactness. These characteristics largely motivate continuum robotics research toward the development of surgical robots that can traverse tortuous pathways in the body and perform surgical tasks. Having continuum robots with these desired traits, while having sufficient payload capacity, are challenging to create, especially for long, slender robots. The work presented in this dissertation aims to address these challenges in improving strength and stability in continuum robots through the development of novel robot designs and derivation of new statics models that can analyze robot response to external loads. While many continuum robot design and modeling advancements have been made over the past 20 years, there are still a number of challenges in fabrication, modeling, and control that still need to be addressed in order to develop these robots for surgical applications. We hope the work presented in this dissertation will serve as a stepping stone for these future developments.

5.1 Tendon-Driven Continuum Robots

The contributions in Chapter 2 include the development of a novel high-strength continuum robot which uses a torsional stiff backbone and a hybrid parallel-converging

tendon routing that improves the resistance to tip loads. Based on the minimal oscillations in the payload carrying task in Chapter 2, the backbone and routing design choices could be used for future real-time control of TDCRs. In addition, novel actuation elements such as the tendon pathways and anti-buckling sub-assemblies could be used to improve the performance of future TDCR actuation designs.

In terms of future work for the TDCR contributions, there are additional design updates that can be applied to the backbone and tendon routing design as well as the addition of kinematic modeling. One addition to the backbone design can include adding a thin-walled backbone down the center of the rhombus pattern, which creates an axially stiff structure that can bend in a single plane. In addition, the derivation of a low-level mechanics model could be derived to predict the mechanical properties based on the geometry of the backbone, which could be computationally efficient for use in design optimization.

5.2 Concentric Tube Robots

The results in Chapter 3 showed how using bellows tubes virtually eliminates the instabilities and kinematic errors from friction found in CTRs, having the lowest flexural-torsional rigidity ratio for symmetric tube designs in the CTR literature to-date. In addition, CPBs also introduce the first soft robot actuation scheme based on concentric tube robots. Soft robotics have received great attention in the robotics research community over the past decade for their potential in safe human-robot collaboration, rehabilitation, and minimally invasive surgical applications. There are a number of benefits of the CPB actuation in regards to soft robot safety and utility. CPBs offer inherently safe actuation, as you cannot 'over-actuate' (e.g. putting too much pressure in a hydraulic-actuated soft robot could rupture the robot) and the inner lumen of the bellows provides space for tools, sensors, and cameras at the tip.

Future work in CPBs are primarily focused on fabrication techniques both for small and large scales and design for specific applications. The fabrication and

modeling work developed in Chapter 3 provides the groundwork for this future work. At small-scales, the high torsional rigidity of bellows tubes are ideal for long transmission sections used in long medical scopes such as colonoscopes where torsional lag continues to be a major issue in the field. At large-scales, traditional manufacturing techniques such as blow molding could be explored to create arbitrarily large CPBs for soft fingered grippers. Since friction was shown to have a minimal effect on kinematic accuracy, CPBs could be useful for real-time control of CTRs through the use of computationally-efficient constant-curvature kinematic models.

5.3 Concentric Push-Pull Robots

As a new sub-field within the continuum robotics research field, there are many exciting opportunities for CPPRs, primarily motivated for the development of surgical robots. The kineto-static model derived and validated in Chapter 4 is the first general model for CPPRs that can account for external loads, and CPPRs using multiple tubes, expanding the capabilities of this robot design. This model can be useful for the design of CPPRs, providing kinematic analysis and interactions with the environment, and can serve as a first step toward the intrinsic force sensing and control of these robots. This dissertation also demonstrates the first three tube CPPR, which has the potential of improving surgeon dexterity, simplifying actuation design, and expanding the degrees of freedom for CPPRs.

The overlapping slotted designs presented in Chapter 4 demonstrate effective payload capacity, for loads applied in-plane and out of the plane. Further design work in tube patterning could further the strength and range of motion capabilities of these devices. Mathematical models that can predict the low-level mechanical properties of the tube pattern (i.e. flexural rigidity, stiffness center offset, etc.) could be achieved through FEA-based parameter sweeps that estimates the mechanical properties or through the derivation of analytical equations of the mechanical properties based on the geometry of the cut pattern. This low-level model could then be used alongside

the derived statics model from Chapter 4 within a larger design optimization scheme to design CPPRs with optimal strength and range of motion.

Bibliography

[1] K. Zhang, C. Qiu, and J. S. Dai, "An Extensible Continuum Robot With Integrated Origami Parallel Modules," *Journal of Mechanisms and Robotics*, vol. 8, no. 3, p. 031010, 2016. xiii, 4

[2] J. Santoso, E. H. Skorina, M. Luo, R. Yan, and C. D. Onal, "Design and analysis of an origami continuum manipulation module with torsional strength," in *2017 IEEE/RSJ International Conference on Intelligent Robots and Systems (IROS)*. IEEE, 9 2017, pp. 2098–2104. xiii, 4

[3] T. Liu, Y. Wang, and K. Lee, "3D Printable Origami Twisted Tower: Design, Fabrication, and Robot Embodiment," *IEEE Robotics and Automation Letters*, vol. 3, no. 1, pp. 1–1, 2017. xiii, 4

[4] N. P. Castledine, J. H. Boyle, and J. Kim, "Design of a modular continuum robot segment for use in a general purpose manipulator," in *Proceedings - IEEE International Conference on Robotics and Automation*, vol. 2019-May. Institute of Electrical and Electronics Engineers Inc., 5 2019, pp. 4430–4435. xiii, 1, 3, 4

[5] A. Shiva, A. Stilli, Y. Noh, A. Faragasso, I. D. Falco, G. Gerboni, M. Cianchetti, A. Menciassi, K. Althoefer, and H. A. Wurdemann, "Tendon-Based Stiffening for a Pneumatically Actuated Soft Manipulator," *IEEE Robotics and Automation Letters*, vol. 1, no. 2, pp. 632–637, 7 2016. xiii, 3, 4

[6] Y. Kim, S. S. Cheng, and J. P. Desai, "Active Stiffness Tuning of a Spring-Based Continuum Robot for MRI-Guided Neurosurgery," *IEEE Transactions on Robotics*, vol. 34, no. 1, pp. 18–28, 2 2018. xiii, 3, 4

[7] H. Azimian, P. Francis, T. Looi, and J. Drake, "Structurally-redesigned concentric-tube manipulators with improved stability," in *2014 IEEE/RSJ International Conference on Intelligent Robots and Systems*. IEEE, 9 2014, pp. 2030–2035. xiii, 6, 8, 36, 37

[8] D.-Y. Lee, J. Kim, J.-S. Kim, C. Baek, G. Noh, D.-N. Kim, K. Kim, S. Kang, and K.-J. Cho, "Anisotropic Patterning to Reduce Instability of Concentric-Tube Robots," *IEEE Transactions on Robotics*, vol. 31, no. 6, pp. 1311–1323, 12 2015. xiii, 6, 8, 36, 37

[9] K. A. Xin Jue Luo, T. Looi, S. Sabetian, and J. Drake, "Designing Concentric Tube Manipulators for Stability Using Topology Optimization," in *2018 IEEE/RSJ International Conference on Intelligent Robots and Systems (IROS)*. IEEE, 10 2018, pp. 1764–1769. xiii, 6, 8, 36, 37

[10] C. Rucker, J. Childs, P. Molaei, and H. B. Gilbert, "Transverse Anisotropy Stabilizes Concentric Tube Robots," *IEEE Robotics and Automation Letters*, vol. 7, no. 2, pp. 2407–2414, 4 2022. xiii, 6, 8

[11] J. M. Hur, D. S. Seo, K. Kim, J. K. Lee, K. J. Lee, Y. Y. Kim, and D. N. Kim, "Harnessing distinct deformation modes of auxetic patterns for stiffness design of tubular structures," *Materials and Design*, vol. 198, p. 109376, 1 2021. xiii, 6, 10

[12] M. Rox, K. Riojas, M. Emerson, K. Oliver-Butler, C. Rucker, and R. J. W. Iii, "Luminal Robots Small Enough to Fit Through Endoscope Ports: Initial Tumor Resection Experiments in the Airways," in *Hamlyn Symposium on Medical Robotics*, 2018. xiii, 9, 10

[13] J. Burgner-Kahrs, D. C. Rucker, and H. Choset, "Continuum Robots for Medical Applications: A Survey," *IEEE Transactions on Robotics*, vol. 31, no. 6, pp. 1261–1280, 12 2015. 1, 10

[14] T. N. Payne and F. R. Dauterive, "A comparison of total laparoscopic hysterectomy to robotically assisted hysterectomy: surgical outcomes in a community practice." *Journal of minimally invasive gynecology*, vol. 15, no. 3, pp. 286–91, 5 2008. 1

[15] A. Gao, Y. Zou, M. Liang, Z. Wang, Z. Wang, and H. Liu, "A contact-aided asymmetric steerable catheter for atrial fibrillation ablation," *IEEE Robotics and Automation Letters*, vol. 2, no. 3, pp. 1525–1531, 7 2017. 1

[16] M. Salerno, K. Zhang, A. Menciassi, and J. S. Dai, "A Novel 4-DOF Origami Grasper With an SMA-Actuation System for Minimally Invasive Surgery," *IEEE Transactions on Robotics*, vol. 32, no. 3, pp. 484–498, 2016. 1

[17] Z. Shi, D. Liu, C. Ma, and D. Zhao, "Accurate controlled shape memory alloy actuator for minimally invasive surgery," in *2011 IEEE International Conference on Mechatronics and Automation, ICMA 2011*, 2011, pp. 817–822. 1

[18] T. Kato, I. Okumura, S. E. Song, A. J. Golby, and N. Hata, "Tendon-Driven Continuum Robot for Endoscopic Surgery: Preclinical Development and Validation of a Tension Propagation Model," *IEEE/ASME Transactions on Mechatronics*, vol. 20, no. 5, pp. 2252–2263, 10 2015. 1, 53

[19] T. Yamaguchi, Y. Ambe, H. Ando, M. Konyo, K. Tadakuma, S. Maruyama, and S. Tadokoro, "A Mechanical Approach to Suppress the Oscillation of a Long Continuum Robot Flying with Water Jets," *IEEE Robotics and Automation Letters*, vol. 4, no. 4, pp. 4346–4353, 10 2019. 1

[20] A. Bajo and N. Simaan, "Finding lost wrenches: Using continuum robots for contact detection and estimation of contact location," *Proceedings - IEEE International Conference on Robotics and Automation*, pp. 3666–3673, 2010. 1

[21] D. Nahar, P. M. Yanik, and I. D. Walker, "Robot tendrils: Long, thin continuum robots for inspection in space operations," *IEEE Aerospace Conference Proceedings*, 6 2017. 1

[22] X. Dong, D. Axinte, D. Palmer, S. Cobos, M. Raffles, A. Rabani, and J. Kell, "Development of a slender continuum robotic system for on-wing inspection/repair of gas turbine engines," *Robotics and Computer-Integrated Manufacturing*, vol. 44, pp. 218–229, 4 2017. 1

[23] X. Dong, M. Wang, A. Mohammad, W. Ba, M. Russo, A. Norton, J. Kell, and D. Axinte, "Continuum Robots Collaborate for Safe Manipulation of High-Temperature Flame to Enable Repairs in Challenging Environments," *IEEE/ASME Transactions on Mechatronics*, 2022. 1

[24] M. M. Tonapi, I. S. Godage, and I. D. Walker, "Next generation rope-like robot for in-space inspection," *IEEE Aerospace Conference Proceedings*, 2014. 1

[25] J. S. Mehling, M. A. Diftler, M. Chu, and M. Valvo, "A minimally invasive tendril robot for in-space inspection," *Proceedings of the First IEEE/RAS-EMBS International Conference on Biomedical Robotics and Biomechatronics, 2006, BioRob 2006*, vol. 2006, pp. 690–695, 2006. 1

[26] T. Zheng, D. T. Branson, E. Guglielmino, R. Kang, G. A. Medrano Cerda, M. Cianchetti, M. Follador, I. S. Godage, and D. G. Caldwell, "Model validation of an octopus inspired continuum robotic arm for use in underwater environments," *Journal of Mechanisms and Robotics*, vol. 5, no. 2, 3 2013. 1

[27] Z. Gong, B. Chen, J. Liu, X. Fang, Z. Liu, T. Wang, and L. Wen, "An opposite-bending-and-extension soft robotic manipulator for delicate grasping in shallow water," *Frontiers Robotics AI*, vol. 6, no. APR, p. 26, 2019. 1

[28] J. Hughes, U. Culha, F. Giardina, F. Guenther, A. Rosendo, and F. Iida, "Soft manipulators and grippers: A review," p. 1, 11 2016. 1

[29] J. Shintake, V. Cacucciolo, D. Floreano, and H. Shea, "Soft Robotic Grippers," *Advanced Materials*, vol. 30, no. 29, p. 1707035, 7 2018. 1

[30] Y. Li, Y. Chen, and Y. Li, "Pre-charged pneumatic soft gripper with closed-loop control," *IEEE Robotics and Automation Letters*, vol. 4, no. 2, pp. 1402–1408, 4 2019. 1

[31] A. Yeshmukhametov, K. Koganezawa, and Y. Yamamoto, "A novel discrete wire-driven continuum robot arm with passive sliding disc: Design, kinematics and passive tension control," *Robotics*, vol. 8, no. 3, p. 51, 7 2019. 1

[32] B. A. Jones and I. D. Walker, "Kinematics for multisection continuum robots," *IEEE Transactions on Robotics*, 2006. 1, 2

[33] B. A. Jones, R. L. Gray, and K. Turlapati, "Three dimensional statics for continuum robotics," in *2009 IEEE/RSJ International Conference on Intelligent Robots and Systems*. IEEE, 10 2009, pp. 2659–2664. 1, 11

[34] D. C. Rucker and R. J. Webster III, "Statics and Dynamics of Continuum Robots With General Tendon Routing and External Loading," *IEEE Transactions on Robotics*, vol. 27, no. 6, pp. 1033–1044, 12 2011. 1, 11

[35] R. E. Goldman, A. Bajo, and N. Simaan, "Compliant Motion Control for Multisegment Continuum Robots With Actuation Force Sensing," *IEEE Transactions on Robotics*, vol. 30, no. 4, pp. 890–902, 8 2014. 1

[36] R. Xu, A. Yurkewich, and R. V. Patel, "Curvature, Torsion, and Force Sensing in Continuum Robots Using Helically Wrapped FBG Sensors," *IEEE Robotics and Automation Letters*, vol. 1, no. 2, 2016. 1

[37] V. Aloi, K. T. Dang, E. J. Barth, and C. Rucker, "Estimating Forces Along Continuum Robots," *IEEE Robotics and Automation Letters*, vol. 7, no. 4, pp. 8877–8884, 10 2022. 1

[38] M. Mahvash and P. E. Dupont, "Stiffness control of surgical continuum manipulators," *IEEE Transactions on Robotics*, vol. 27, no. 2, pp. 334–345, 4 2011. 1

[39] D. Rus and M. T. Tolley, "Design, fabrication and control of soft robots," *Nature*, vol. 521, no. 7553, pp. 467–475, 5 2015. 1

[40] A. A. Alqumsan, S. Khoo, and M. Norton, "Robust control of continuum robots using Cosserat rod theory," *Mechanism and Machine Theory*, vol. 131, pp. 48–61, 1 2019. 1

[41] P. Rao, Q. Peyron, S. Lilge, and J. Burgner-Kahrs, "How to Model Tendon-Driven Continuum Robots and Benchmark Modelling Performance," *Frontiers in Robotics and AI*, vol. 7, p. 223, 2 2021. 1, 2

[42] P. Polygerinos, N. Correll, S. A. Morin, B. Mosadegh, C. D. Onal, K. Petersen, M. Cianchetti, M. T. Tolley, and R. F. Shepherd, "Soft Robotics: Review of Fluid-Driven Intrinsically Soft Devices; Manufacturing, Sensing, Control, and Applications in Human-Robot Interaction," 2017. 1

[43] A. D. Marchese, R. Tedrake, and D. Rus, "Dynamics and trajectory optimization for a soft spatial fluidic elastomer manipulator," in *Proceedings - IEEE International Conference on Robotics and Automation*, vol. 2015-June, no. June. Institute of Electrical and Electronics Engineers Inc., 6 2015, pp. 2528–2535. 1

[44] Y. Haibin, K. Cheng, L. Junfeng, and Y. Guilin, "Modeling of grasping force for a soft robotic gripper with variable stiffness," *Mechanism and Machine Theory*, vol. 128, pp. 254–274, 10 2018. 1

[45] H. Zhang, A. S. Kumar, J. Y. H. Fuh, and M. Y. Wang, "Investigation on Developing a Topology Optimized and 3D Printable Multimaterial Soft Gripper," in *IEEE International Conference on Control and Automation, ICCA*, vol. 2018-June. IEEE Computer Society, 8 2018, pp. 692–697. 1

[46] H. B. Gilbert, D. C. Rucker, and R. J. Webster III, "Concentric Tube Robots: The State of the Art and Future Directions." Springer, Cham, 2016, pp. 253–269. 1

[47] J. Wang, J. Ha, and P. E. Dupont, "Steering a multi-armed robotic sheath using eccentric precurved tubes," in *Proceedings - IEEE International Conference on Robotics and Automation*, vol. 2019-May. Institute of Electrical and Electronics Engineers Inc., 5 2019, pp. 9834–9840. 1, 11

[48] L. Wang, F. C. Pedrosa, and R. V. Patel, "Eccentric-Tube Robot (ETR) Modeling and Validation," in *Proceedings of the IEEE RAS and EMBS International Conference on Biomedical Robotics and Biomechatronics*, vol. 2020-November. IEEE Computer Society, 11 2020, pp. 866–871. 1, 11

[49] Y. J. Kim, S. Cheng, S. Kim, and K. Iagnemma, "A stiffness-adjustable hyperredundant manipulator using a variable neutral-line mechanism for minimally invasive surgery," *IEEE Transactions on Robotics*, vol. 30, no. 2, pp. 382–395, 2014. 3

[50] A. Fishman, M. S. Garrad, A. Hinitt, P. Zanini, T. Barker, and J. Rossiter, "A Compliant Telescopic Limb with Anisotropic Stiffness," *Frontiers in Robotics and AI*, vol. 3, no. FEB, p. 80, 2 2017. 3

[51] G. Dammer, S. Gablenz, A. Hildebrandt, and Z. Major, "Design and shape optimization of PolyJet bellows actuators," in *2018 IEEE International Conference on Soft Robotics (RoboSoft)*. IEEE, 4 2018, pp. 282–287. 3

[52] D. Drotman, S. Jadhav, M. Karimi, P. deZonia, and M. T. Tolley, "3D printed soft actuators for a legged robot capable of navigating unstructured terrain," in *2017 IEEE International Conference on Robotics and Automation (ICRA)*. IEEE, 5 2017, pp. 5532–5538. 3, 36

[53] T. Rehman, A. A. M. Faudzi, D. E. O. Dewi, and M. S. M. Ali, "Design, characterization, and manufacturing of circular bellows pneumatic soft actuator," *International Journal of Advanced Manufacturing Technology*, vol. 93, no. 9-12, pp. 4295–4304, 12 2017. 3

[54] J. A. Childs and C. Rucker, "Concentric precurved bellows: New bending actuators for soft robots," *IEEE Robotics and Automation Letters*, vol. 5, no. 2, pp. 1215–1222, 4 2020. 3, 35

[55] J. Santoso and C. D. Onal, "An Origami Continuum Robot Capable of Precise Motion Through Torsionally Stiff Body and Smooth Inverse Kinematics," *Soft Robotics*, p. soro.2020.0026, 7 2020. 3

[56] D. Rus and C. Sung, "Spotlight on origami robots," *Science Robotics*, pp. 2–4, 2018. 3

[57] N. Liu, M. E. Abdelaziz, M. Shen, and G. Z. Yang, "Design and Kinematics Characterization of a Laser-Profiled Continuum Manipulator for the Guidance of Bronchoscopic Instruments," *Proceedings - IEEE International Conference on Robotics and Automation*, pp. 25–31, 9 2018. 3

[58] C. D. Onal, M. T. Tolley, R. J. Wood, and D. Rus, "Origami-Inspired Printed Robots," *IEEE/ASME Transactions on Mechatronics*, vol. 20, no. 5, pp. 2214–2221, 10 2015. 3

[59] A. Reid, F. Lechenault, S. Rica, and M. Adda-Bedia, "Geometry and design of origami bellows with tunable response," *Physical Review E*, vol. 95, no. 1, p. 013002, 1 2017. 3

[60] S. M. Felton, D. Y. Lee, K. J. Cho, and R. J. Wood, "A passive, origami-inspired, continuously variable transmission," in *Proceedings - IEEE International Conference on Robotics and Automation*. Institute of Electrical and Electronics Engineers Inc., 9 2014, pp. 2913–2918. 3

[61] A. Jiang, G. Xynogalas, P. Dasgupta, K. Althoefer, and T. Nanayakkara, "Design of a variable stiffness flexible manipulator with composite granular jamming and membrane coupling," in *IEEE International Conference on Intelligent Robots and Systems*, 2012, pp. 2922–2927. 3

[62] Y. Jiang, D. Chen, C. Liu, and J. Li, "Chain-Like Granular Jamming: A Novel Stiffness-Programmable Mechanism for Soft Robotics," *Soft Robotics*, vol. 6, no. 1, pp. 118–132, 2 2019. 3

[63] H. Jeon, Q. N. Le, S. Jeong, S. Jang, H. Jung, H. Chang, H. J. Pandya, and Y. Kim, "Towards a Snake-Like Flexible Robot With Variable Stiffness Using an SMA Spring-Based Friction Change Mechanism," *IEEE Robotics and Automation Letters*, vol. 7, no. 3, pp. 6582–6589, 7 2022. 3

[64] J. C. Case, E. L. White, V. Sunspiral, and R. Kramer-Bottiglio, "Reducing Actuator Requirements in Continuum Robots Through Optimized Cable Routing," *Soft Robotics*, vol. 5, no. 1, pp. 109–118, 2 2018. 5

[65] J. Starke, E. Amanov, M. T. Chikhaoui, and J. Burgner-Kahrs, "On the merits of helical tendon routing in continuum robots," in *IEEE International Conference on Intelligent Robots and Systems*, vol. 2017-September. Institute of Electrical and Electronics Engineers Inc., 12 2017, pp. 6470–6476. 5

[66] Y. Kim, S. S. Cheng, M. Diakite, R. P. Gullapalli, J. M. Simard, and J. P. Desai, "Toward the development of a flexible mesoscale MRI-compatible neurosurgical continuum robot," *IEEE Transactions on Robotics*, vol. 33, no. 6, pp. 1386–1397, 12 2017. 5

[67] K. Oliver-Butler, J. Till, and C. Rucker, "Continuum Robot Stiffness under External Loads and Prescribed Tendon Displacements," *IEEE Transactions on Robotics*, vol. 35, no. 2, pp. 403–419, 4 2019. 5, 93

[68] R. Webster, A. Okamura, and N. Cowan, "Toward Active Cannulas: Miniature Snake-Like Surgical Robots," in *2006 IEEE/RSJ International Conference on Intelligent Robots and Systems*. IEEE, 10 2006, pp. 2857–2863. 5

[69] P. Sears and P. Dupont, "A steerable needle technology using curved concentric tubes," in *IEEE International Conference on Intelligent Robots and Systems*, 2006, pp. 2850–2856. 5

[70] P. Dupont, J. Lock, and E. Butler, "Torsional kinematic model for concentric tube robots," in *2009 IEEE International Conference on Robotics and Automation*. IEEE, 5 2009, pp. 3851–3858. 7, 11, 66

[71] D. C. Rucker, B. A. Jones, and R. J. Webster III, "A Geometrically Exact Model for Externally Loaded Concentric-Tube Continuum Robots," *IEEE Transactions on Robotics*, vol. 26, no. 5, pp. 769–780, 10 2010. 7, 11, 66

[72] J. Lock and P. E. Dupont, "Friction modeling in concentric tube robots," in *2011 IEEE International Conference on Robotics and Automation*. IEEE, 5 2011, pp. 1139–1146. 7

[73] S. W. Han, A. Sawatsky, H. de Brito Fontana, and W. Herzog, "Contribution of individual quadriceps muscles to knee joint mechanics," *Journal of Experimental Biology*, vol. 222, no. 6, 2019. 7

[74] P. Dupont, J. Lock, B. Itkowitz, and E. Butler, "Design and Control of Concentric-Tube Robots," *IEEE Transactions on Robotics*, vol. 26, no. 2, pp. 209–225, 4 2010. 7, 11, 35, 38, 48, 66

[75] H. Su, D. C. Cardona, W. Shang, A. Camilo, G. A. Cole, D. C. Rucker, R. J. Webster, and G. S. Fischer, "A MRI-guided concentric tube continuum robot with piezoelectric actuation: A feasibility study," in *Proceedings - IEEE International Conference on Robotics and Automation*. Institute of Electrical and Electronics Engineers Inc., 2012, pp. 1939–1945. 7

[76] R. Ponten, C. B. Black, A. J. Russ, and D. C. Rucker, "Analysis of a concentric-tube robot design and feasibility for endoscopic deployment," in *Medical Imaging 2017: Image-Guided Procedures, Robotic Interventions, and Modeling*, R. J. Webster and B. Fei, Eds., vol. 10135. SPIE, 3 2017, p. 1013514. 7

[77] M. U. Farooq, W. Y. Kim, and S. Y. Ko, "A cost-effective and miniaturized actuation system for two three-tube concentric tube robots with parallel actuation," in *International Conference on Control, Automation and Systems*, vol. 2017-October. IEEE Computer Society, 12 2017, pp. 1382–1386. 7

[78] J. Burgner, D. C. Rucker, H. B. Gilbert, P. J. Swaney, P. T. Russell, K. D. Weaver, and R. J. Webster, "A telerobotic system for transnasal surgery," *IEEE/ASME Transactions on Mechatronics*, vol. 19, no. 3, pp. 996–1006, 2014. 7

[79] C. Bergeles and P. E. Dupont, "Planning stable paths for concentric tube robots," in *2013 IEEE/RSJ International Conference on Intelligent Robots and Systems*. IEEE, 11 2013, pp. 3077–3082. 7

[80] C. Bergeles, A. H. Gosline, N. V. Vasilyev, P. J. Codd, P. J. Del Nido, and P. E. Dupont, "Concentric tube robot design and optimization based on task

and anatomical constraints," *IEEE Transactions on Robotics*, vol. 31, no. 1, pp. 67–84, 2 2015. 7

[81] C. Baykal, L. G. Torres, and R. Alterovitz, "Optimizing design parameters for sets of concentric tube robots using sampling-based motion planning," in *2015 IEEE/RSJ International Conference on Intelligent Robots and Systems (IROS)*. IEEE, 9 2015, pp. 4381–4387. 7

[82] K. Leibrandt, C. Bergeles, and G. Z. Yang, "On-line collision-free inverse kinematics with frictional active constraints for effective control of unstable concentric tube robots," *IEEE International Conference on Intelligent Robots and Systems*, vol. 2015-December, pp. 3797–3804, 12 2015. 7

[83] L. G. Torres, R. J. Webster, and R. Alterovitz, "Task-oriented design of concentric tube robots using mechanics-based models," in *IEEE International Conference on Intelligent Robots and Systems*, 2012, pp. 4449–4455. 7

[84] T. K. Morimoto and A. M. Okamura, "Design of 3-D Printed Concentric Tube Robots," *IEEE Transactions on Robotics*, vol. 32, no. 6, pp. 1419–1430, 12 2016. 7

[85] A. Vandini, C. Bergeles, F. Y. Lin, and G. Z. Yang, "Vision-based intraoperative shape sensing of concentric tube robots," in *IEEE International Conference on Intelligent Robots and Systems*, vol. 2015-December. Institute of Electrical and Electronics Engineers Inc., 12 2015, pp. 2603–2610. 7

[86] A. Vandini, C. Bergeles, B. Glocker, P. Giataganas, and G.-Z. Yang, "Unified Tracking and Shape Estimation for Concentric Tube Robots," *IEEE Transactions on Robotics*, vol. 33, no. 4, pp. 901–915, 8 2017. 7

[87] C. Shi, X. Luo, P. Qi, T. Li, S. Song, Z. Najdovski, T. Fukuda, and H. Ren, "Shape sensing techniques for continuum robots in minimally invasive surgery:

A survey," *IEEE Transactions on Biomedical Engineering*, vol. 64, no. 8, pp. 1665–1678, 8 2017. 7

[88] R. Webster, J. Romano, and N. Cowan, "Mechanics of Precurved-Tube Continuum Robots," *IEEE Transactions on Robotics*, vol. 25, no. 1, pp. 67–78, 2 2009. 7, 11, 35, 38, 48

[89] H. B. Gilbert, R. J. Hendrick, and R. J. Webster III, "Elastic Stability of Concentric Tube Robots: A Stability Measure and Design Test," *IEEE Transactions on Robotics*, vol. 32, no. 1, pp. 20–35, 2 2016. 7, 10

[90] J. Ha, F. C. Park, and P. E. Dupont, "Elastic Stability of Concentric Tube Robots Subject to External Loads," *IEEE Transactions on Biomedical Engineering*, vol. 63, no. 6, pp. 1116–1128, 6 2016. 7

[91] J. Till, V. Aloi, K. E. Riojas, P. L. Anderson, R. J. Webster, and C. Rucker, "A dynamic model for concentric tube robots," *IEEE Transactions on Robotics*, vol. 36, no. 6, pp. 1704–1718, 12 2020. 7

[92] S. M. Sadati, Z. Mitros, R. Henry, L. Zeng, L. D. Cruz, and C. Bergeles, "Real-Time Dynamics of Concentric Tube Robots with Reduced-Order Kinematics Based on Shape Interpolation," *IEEE Robotics and Automation Letters*, vol. 7, no. 2, pp. 5671–5678, 4 2022. 7

[93] J. Ha, F. C. Park, and P. E. Dupont, "Achieving elastic stability of concentric tube robots through optimization of tube precurvature," in *2014 IEEE/RSJ International Conference on Intelligent Robots and Systems*. IEEE, 9 2014, pp. 864–870. 7

[94] K. E. Riojas, R. J. Hendrick, and R. J. Webster, "Can Elastic Instability Be Beneficial in Concentric Tube Robots?" *IEEE Robotics and Automation Letters*, vol. 3, no. 3, pp. 1624–1630, 7 2018. 7

[95] R. J. Hendrick, H. B. Gilbert, and R. J. Webster, "Designing snap-free concentric tube robots: A local bifurcation approach," *Proceedings - IEEE International Conference on Robotics and Automation*, vol. 2015-June, no. June, pp. 2256–2263, 6 2015. 7

[96] C. Fellmann and J. Burgner-Kahrs, "Implications of trajectory generation strategies for tubular continuum robots," *IEEE International Conference on Intelligent Robots and Systems*, vol. 2015-December, pp. 202–208, 12 2015. 7

[97] K. Leibrandt, C. Bergeles, and G. Z. Yang, "Implicit active constraints for safe and effective guidance of unstable concentric tube robots," *IEEE International Conference on Intelligent Robots and Systems*, vol. 2016-November, pp. 1157–1163, 11 2016. 7

[98] J.-S. Kim, D.-Y. Lee, K. Kim, S. Kang, and K.-J. Cho, "Toward a solution to the snapping problem in a concentric-tube continuum robot: Grooved tubes with anisotropy," in *2014 IEEE International Conference on Robotics and Automation (ICRA)*. IEEE, 5 2014, pp. 5871–5876. 8, 36, 37

[99] K. Oliver-Butler, J. A. Childs, A. Daniel, and D. C. Rucker, "Concentric Push–Pull Robots: Planar Modeling and Design," *IEEE Transactions on Robotics*, pp. 1–15, 9 2021. 8, 10

[100] J. Kim, W. Y. Choi, S. Kang, C. Kim, and K. J. Cho, "Continuously Variable Stiffness Mechanism Using Nonuniform Patterns on Coaxial Tubes for Continuum Microsurgical Robot," *IEEE Transactions on Robotics*, vol. 35, no. 6, pp. 1475–1487, 12 2019. 8

[101] P. J. Swaney, P. A. York, H. B. Gilbert, J. Burgner-Kahrs, and R. J. Webster, "Design, fabrication, and testing of a needle-sized wrist for surgical instruments," *Journal of Medical Devices, Transactions of the ASME*, vol. 11, no. 1, pp. 0 145 011–145 019, 3 2017. 8

[102] P. A. York, P. J. Swaney, H. B. Gilbert, and R. J. Webster, "A wrist for needle-sized surgical robots," in *Proceedings - IEEE International Conference on Robotics and Automation*, vol. 2015-June, no. June. Institute of Electrical and Electronics Engineers Inc., 6 2015, pp. 1776–1781. 8

[103] K. W. Eastwood, H. Azimian, B. Carrillo, T. Looi, H. E. Naguib, and J. M. Drake, "Kinetostatic design of asymmetric notch joints for surgical robots," *IEEE International Conference on Intelligent Robots and Systems*, vol. 2016-November, pp. 2381–2387, 11 2016. 8

[104] K. Oliver-Butler, Z. H. Epps, and D. C. Rucker, "Concentric agonist-antagonist robots for minimally invasive surgeries," in *Medical Imaging 2017: Image-Guided Procedures, Robotic Interventions, and Modeling*, R. J. Webster and B. Fei, Eds., vol. 10135. SPIE, 3 2017, p. 1013511. 8

[105] K. Xu, M. Fu, and J. Zhao, "An experimental kinestatic comparison between continuum manipulators with structural variations," *Proceedings - IEEE International Conference on Robotics and Automation*, pp. 3258–3264, 9 2014. 10

[106] M. F. Simons, K. M. Digumarti, A. T. Conn, and J. Rossiter, "Tiled auxetic cylinders for soft robots," *RoboSoft 2019 - 2019 IEEE International Conference on Soft Robotics*, pp. 62–67, 5 2019. 10

[107] Q. Lu and B. He, "Kinematics and energy minimization approach for continuum robot," *Mechanisms and Machine Science*, vol. 36, pp. 817–827, 2016. 11

[108] F. Renda, M. Giorelli, M. Calisti, M. Cianchetti, and C. Laschi, "Dynamic Model of a Multibending Soft Robot Arm Driven by Cables," *IEEE Transactions on Robotics*, vol. 30, no. 5, pp. 1109–1122, 10 2014. 11

[109] D. C. Rucker, R. J. Webster, G. S. Chirikjian, and N. J. Cowan, "Equilibrium Conformations of Concentric-tube Continuum Robots," *The International Journal of Robotics Research*, vol. 29, no. 10, pp. 1263–1280, 4 2010. 11

[110] J. Till, V. Aloi, and C. Rucker, "Real-time dynamics of soft and continuum robots based on Cosserat rod models," *The International Journal of Robotics Research*, vol. 38, no. 6, pp. 723–746, 5 2019. 11

[111] C. B. Black, J. Till, and D. C. Rucker, "Parallel Continuum Robots: Modeling, Analysis, and Actuation-Based Force Sensing," *IEEE Transactions on Robotics*, vol. 34, no. 1, pp. 29–47, 2 2018. 11

[112] J. Till, C. E. Bryson, S. Chung, A. Orekhov, and D. C. Rucker, "Efficient computation of multiple coupled Cosserat rod models for real-time simulation and control of parallel continuum manipulators," in *Proceedings - IEEE International Conference on Robotics and Automation*, vol. 2015-June, no. June. Institute of Electrical and Electronics Engineers Inc., 6 2015, pp. 5067–5074. 11

[113] K. M. de Payrebrune and O. M. O'Reilly, "On the development of rod-based models for pneumatically actuated soft robot arms: A five-parameter constitutive relation," *International Journal of Solids and Structures*, vol. 120, pp. 226–235, 8 2017. 11

[114] D. Trivedi, D. Dienno, and C. D. Rahn, "Optimal, model-based design of soft robotic manipulators," *Journal of Mechanical Design, Transactions of the ASME*, vol. 130, no. 9, pp. 0 914 021–0 914 029, 9 2008. 11

[115] J. Till and D. C. Rucker, "Elastic stability of cosserat rods and parallel continuum robots," *IEEE Transactions on Robotics*, vol. 33, no. 3, pp. 718–733, 6 2017. 11

[116] J. A. Childs and C. Rucker, "Leveraging Geometry to Enable High-Strength Continuum Robots," *Frontiers in Robotics and AI*, vol. 8, no. 629871, 2 2021. 13, 93

[117] G. Dolzyk and S. Jung, "Tensile and Fatigue Analysis of 3D-Printed Polyethylene Terephthalate Glycol," *Journal of Failure Analysis and Prevention*, vol. 19, no. 2, pp. 511–518, 4 2019. 15, 17

[118] L. Virgin, "On the flexural stiffness of 3D printer thermoplastic," *International Journal of Mechanical Engineering Education*, vol. 45, no. 1, pp. 59–75, 1 2017. 44, 46

[119] R. L. Bishop, "There is More than One Way to Frame a Curve," *The American Mathematical Monthly*, vol. 82, no. 3, p. 246, 3 1975. 48, 66

[120] R. J. Webster and B. A. Jones, "Design and kinematic modeling of constant curvature continuum robots: A review," *International Journal of Robotics Research*, vol. 29, no. 13, pp. 1661–1683, 2010. 50

[121] G. Subramani and M. R. Zinn, "Tackling friction - An analytical modeling approach to understanding friction in single tendon driven continuum manipulators," in *Proceedings - IEEE International Conference on Robotics and Automation*, vol. 2015-June, no. June. Institute of Electrical and Electronics Engineers Inc., 6 2015, pp. 610–617. 53

[122] R. M. Murray, Z. Li, and S. Shankar Sastry, *A Mathematical Introduction to Robotic Manipulation*. CRC Press, 12 1994. 65

[123] G. Barillaro, A. Molfese, A. Nannini, and F. Pieri, "Analysis, simulation and relative performances of two kinds of serpentine springs," *Journal of Micromechanics and Microengineering*, vol. 15, no. 4, pp. 736–746, 4 2005. 80

[124] S. Neppalli, M. Csencsits, B. Jones, and I. Walker, "A Geometrical Approach to Inverse Kinematics for Continuum Manipulators," Tech. Rep., 2008. 97

[125] E. H. Skorina and C. D. Onal, "Soft Hybrid Wave Spring Actuators," *Advanced Intelligent Systems*, vol. 2, no. 1, p. 1900097, 1 2020. 97

[126] C. A. Biffi and A. Tuissi, "Nitinol laser cutting: microstructure and functional properties of femtosecond and continuous wave laser processing," *Smart Materials and Structures*, vol. 26, no. 3, p. 035006, 2 2017. 105

Vita

Jake A. Childs was born in Oak Ridge, TN and grew up in Kingston, TN. He completed his AS in Mechanical Engineering from Roane State Community College in 2015, and his BS and MS in Mechanical Engineering from the University of Tennessee, Knoxville in 2017 and 2020 respectively. As a graduate student, he was awarded the J. Wallace and Katie Dean Graduate Fellowship in 2018, served as president of the Graduate Association of MABE Engineers (GAME) from 2019 through 2021, and was awarded the MABE Outstanding Graduate Student Award in 2022. His research interests are in the design and modeling of continuum robots and their implementation in medical applications.